
Doctoral

Engineering

2021

Optical fiber sensors for in-situ detection of solid-liquid phase change for n-octadecane

Wei Han

Technological University Dublin, hanwei20041375@gmail.com

Follow this and additional works at: <https://arrow.tudublin.ie/engdoc>



Part of the [Electrical and Computer Engineering Commons](#)

Recommended Citation

Han, W. (2021). Optical fiber sensors for in-situ detection of solid-liquid phase change for n-octadecane. Technological University Dublin. DOI: 10.21427/WQQ6-1705

This Theses, Ph.D is brought to you for free and open access by the Engineering at ARROW@TU Dublin. It has been accepted for inclusion in Doctoral by an authorized administrator of ARROW@TU Dublin. For more information, please contact arrow.admin@tudublin.ie, aisling.coyne@tudublin.ie, vera.kilshaw@tudublin.ie.

Optical fiber sensors for in-situ detection of solid-liquid phase change for n-octadecane

A thesis

Submitted for the degree of Doctor of Philosophy

by

Wei Han



School of Electrical and Electronic Engineering
College of Engineering & Built in Environment
Technological University Dublin

**Supervisors: Prof. Yuliya Semenova, Dr. Qiang Wu,
Prof. Gerald Farrell and Dr. Marek Rebow**

Dublin, Ireland

April, 2021

To my parents with all my love

Abstract

In the past few decades solid-liquid phase change materials (PCMs) have gained an increasingly important role in thermal energy storage applications due to their ability to absorb or release large amounts of energy during melting or solidification. The precise phase change temperature varies with different conditions, such as external pressure, small variations in the PCM composition in the case of multi-component mixtures and/or material purity. In order to achieve better energy efficiency for the energy storage process, it is necessary to be able to accurately detect the solid-liquid phase changes in the bulk of a PCM.

Optical fiber sensors allow for direct detection of the phase changes in PCMs while also offering the advantages of a passive nature and small size.

The focus of the research presented in this thesis is on the development of a novel approach to detecting the solid-liquid phase changes in selected PCMs using optical fiber sensors. To achieve this goal, initially the correlation between the temperature, changes in the refractive index (RI) and internal pressure acting upon the optical fiber during the phase transitions was studied for the selected PCM, n-octadecane. Based on the results of these studies, several optical fiber sensing structures have been proposed and demonstrated for the detection of phase changes as follows:

An optical fiber Fresnel reflection sensor for detection of phase changes

An fiber Fresnel reflection sensor for detection of solid-liquid phase change in n-octadecane is proposed and experimentally demonstrated. The sensor probe consists of a single-mode fiber with a cleaved end immersed in the n-octadecane

sample under test. The detection relies on measuring the slope of the output power ratio change which is caused by the RI change during the phase transition. The results of this work suggest that such a simple optical fiber sensor can be used for detection of liquid-solid phase changes in other materials with similar thermo-optic properties to n-octadecane. This sensor realized in-situ detection for a solid liquid phase change, which is a significant advantage compared to the traditional phase change detection methods

A fiber heterostructure based optical fiber sensor for detection of phase changes.

A single-mode-no-core-single-mode fiber optical sensor for the detection of solid-liquid and liquid-solid phase changes in n-octadecane is proposed and demonstrated. The transmission-type sensor probe consists of a short section of no-core fiber sandwiched between two sections of a single-mode fiber. The detection relies on measuring the level of the output power ratio which is caused by the large step-like variations in the RI of n-octadecane's. Importantly, compared to the Fresnel reflection sensor, the proposed fiber heterostructure is resistant to bending and strain disturbances during the measurements. The results of this work suggest that the proposed sensor is potentially capable of detecting liquid-solid phase changes in other materials whose thermo-optic properties are similar to those of n-octadecane. Moreover, this sensor not only has the advantage of achieving in-situ phase change detection, but also has the ability of working in an environment subjected to mechanical disturbance, which makes it has great potential of industry applications.

Optical fiber Fabry-Perot sensor based on a singlemode-hollow core-singlemode fiber

An optical fiber Fabry-Perot sensor to monitor the solid-liquid and liquid-solid phase changes in n-octadecane is also proposed and investigated. The sensor probe is fabricated by splicing a short section of a hollow core fiber between two single-mode fibers. By analyzing the changes in the output spectrum of the probe, such as spectral shift of a selected interference dip, the phase change within a material sample in the vicinity of the fiber probe can be accurately detected. The proposed sensor can deal with PCM types whose RI values make it difficult for the other two sensor types to work, and also can be used for detection of the material's phase state at a particular point of its volume. This work has the potential to better understanding phase change mechanism and its application in energy engineering. Compared to the other sensors developed in the research presented in this thesis, this sensor has the advantage that the application is not limited by the RI of the PCMs.

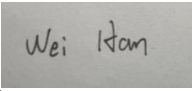
Declaration

I certify that this thesis which I now submit for examination for the award of MPhil, is entirely my own work and has not been taken from the work of others save and to the extent that such work has been cited and acknowledged within the text of my work.

This thesis was prepared according to the regulations for postgraduate study by research of the Technological University Dublin and has not been submitted in whole or in part for an award in any other Institute or University.

The work reported in this thesis conforms to the principles and requirements of Institute's guidelines for ethics in research.

The Institute has permission to keep, to lend or to copy this thesis in whole or in part, on condition that any such use of the material of the thesis be duly acknowledged.

Signature _____  _____ Date 06/04/2021 _____

Candidate

Acknowledgements

The work presented in this thesis would not have been possible without the tremendous support I received from the Photonics Research Centre of the Technological University Dublin, and the great number of enabling people I encountered here.

I would like to express my sincere gratitude to Dr. Marek Rebow for his continuing support of my research. His immense knowledge and experience in this field, and unwavering enthusiasm guided me through the most challenging time during my research. His passion for science and relentless desire to search for the unknown has always been my aspiration. I am fortunate to have him as my supervisor.

I would like to thank Prof. Yuliya Semenova. Prof. Semenova offered numerous insightful comments which helped shape this project. Her astute understanding of optical fiber sensor helped me navigate the complex topics I faced in research. She encouraged me to take innovative approaches to experimental design and held me to a high scientific standard in evaluating my own work.

I would also like to offer my deep appreciation of the selfless willingness of Prof. Gerald Farrell to help. Prof. Farrell spent countless hours reading and critiquing my articles. He taught me how to apply critical thinking in writing to communicate ideas and showed me how scientific writing could be both erudite and accessible.

I would also like thank Dr. Qiang Wu for challenging me when I am in need. He played a massive role in my development as a scientist and inspired me to be a better researcher and person. His rigorous and serious attitude towards science research is an example for me to follow.

Within the Photonic Research Centre, I am also grateful to Dr. Vishnu Kavungal, Dr. Arun Kumar Mallik, Dr. Fangfang Wei, Dr. Xiaokang Lian for all the help they provided. From the early days, if it wasn't for the help of great friends like them, those first 12 months of living in Ireland would have been extremely difficult.

Last but not the least, I would like to express my gratitude to my parents. I am fortunate to have enjoyed their unconditional support throughout the years. They nourished my passion for science, and encouraged me to pursue my dream. My parents made sacrifices to help me achieve my ambition as if it was their own. I would not have arrived at this stage today without them as the pillars of my strength.

Wei Han

August 2021

List of publications arising from research

Journal papers

1. Kumar, R., Han, W., Liu, D., Ng, W. P., Binns, R., Busawon, K., & Wu, Q. (2018). Optical fibre sensors for monitoring phase transitions in phase changing materials. *Smart Materials and Structures*, 27(10), 105021.
2. Han, W., Rebow, M., Liu, D., Farrell, G., Semenova, Y., & Wu, Q. (2018). Optical fiber Fresnel reflection sensor for direct detection of the solid–liquid phase change in n-octadecane. *Measurement Science and Technology*, 29(12), 125107.
3. Han, W., Rebow, M., Lian, X., Liu, D., Farrell, G., Wu, Q., Ma, Y., & Semenova, Y. (2019). SNS optical fiber sensor for direct detection of phase transitions in C18H38 n-alkane material. *Experimental Thermal and Fluid Science*, 109, 109854.
4. Han, W., Rebow, M., Lian, X., Liu, D., Farrell, G., Wu, Q., & Semenova, Y. (2021). Optical fiber Fabry-Perot sensor based on a singlemode-hollow core-singlemode fiber structure for direct detection of phase transition in n-octadecane. *Measurement*, 110002.
5. Liu, D., Han, W., Mallik, A. K., Yuan, J., Yu, C., Farrell, G., Semenova, Y., & Wu, Q. (2016). High sensitivity sol-gel silica coated optical fiber sensor for detection of ammonia in water. *Optics express*, 24(21), 24179-24187.
6. Liu, D., Kumar, R., Wei, F., Han, W., Mallik, A. K., Yuan, J., Yu, C., Kang, Z., Li, F., Liu, Z., Tam, H., Farrell, G., Semenova, Y. & Wu, Q. (2018). Highly sensitive twist sensor based on partially silver coated hollow core fiber structure. *Journal of Lightwave Technology*, 36(17), 3672-3677.
7. Liu, D., Wu, Q., Han, W., Wei, F., Ling, F., Kumar, R., Tian, K., Shen, C., Farrell, g., Semenova, Y., & Wang, P. (2019). Strain independent twist sensor based on uneven platinum coated hollow core fiber structure. *Optics express*, 27(14), 19726-19736.

8. Lian, X., Farrell, G., Wu, Q., Han, W., Shen, C., Ma, Y., & Semenova, Y. (2020). Anti-resonance, inhibited coupling and mode transition in depressed core fibers. *Optics express*, 28(11), 16526-16541.
9. Lian, X., Farrell, G., Wu, Q., Han, W., Shen, C., Ma, Y., & Semenova, Y. (2020). Spectral dependence of transmission losses in high-index polymer coated no-core fibers. *Journal of Lightwave Technology*, 38(22), 6352-6361.

Conference papers

1. Han, W., Liu, D., Lian, X., Mallik, A. K., Wei, F., Sun, L., Farrell, G., Semenova, Y., & Wu, Q. (2016, November). A spherical-structure based fiber sensor for simultaneous measurement of ammonia gas concentration and temperature. In *Advanced Sensor Systems and Applications VII* (Vol. 10025, p. 100251J). International Society for Optics and Photonics..
2. Liu, D, Han, W., Farrell, G., Semenova, Y., and Wu, Q., Tapered hetero-core silica fiber structure for relative humidity sensing. Photonics Ireland 2015, Cork, 2015. (poster presentation)
3. Wei, F., Mallik, A. K., Liu, D., Han, W., Lian, X., Farrell, G., Wu, Q., Peng, G., & Semenova, Y. (2017, April). Simultaneous measurement of both magnetic field strength and temperature with a microfiber coupler based fiber laser sensor. In *2017 25th Optical Fiber Sensors Conference (OFS)* (pp. 1-4). IEEE.
4. Kumar, R., Han, W., Liu, D., Ng, W. P., Binns, R., Busawon, K., Fu, Y., Ghassemlooy, Z., Underwood, C., Mahkmov, K., Yuan, J., Yu, C., Shu, H., Li, X., Guo, T., Farrell, G., Semenova, Y., & Wu, Q. (2018, August). Singlemode-multimode-singlemode fibre structure for phase transition monitoring in phase changing materials. In *Journal of Physics: Conference Series* (Vol. 1065, No. 25, p. 252024). IOP Publishing.

Contents

Abstract.....	I
Declaration.....	IV
Acknowledgements.....	V
List of publications arising from research.....	VII
Contents.....	IX
List of figures.....	XI
Acronyms	XIII
Chapter 1. Introduction	1
1.1 Research background.....	1
1.2 Classification and properties of phase change materials	4
1.2.1 Classification of PCMs	6
1.2.2 Properties of phase change materials	8
1.2.3 Applications of PCMs	15
1.3 The need for accurate detection of phase changes in PCMs.....	20
1.4 Aim and objectives of the thesis.....	23
1.5 Layout of the thesis.....	24
Chapter 2 Fundamentals of Optical Fiber Sensors for Phase Change Detection.....	26
2.1 Light propagation in an optical fiber	26
2.2 Optical fiber sensors and their applications	30
2.2.1 Fresnel-reflection based fiber sensor	31
2.2.2 Interferometric fiber sensors.....	32
Chapter 3 Overview of methods for the detection of phase changes in PCMs.....	38
3.1 Introduction	38
3.2 Common methods for the detection for phase changes in PCMs.....	39
3.3 Optical fiber sensors for phase change detection	43
3.3.1 Existing optical fiber sensing methods for phase change detection	43

3.3.2 Optical fiber sensing techniques for detecting the phenomena associated with phase change	46
3.4 Conclusion	48
Chapter 4 Optical Fiber Fresnel Reflection Sensor for Detection of Phase Changes.....	51
4.1 Introduction	51
4.2 Experimental setup and operating principle.....	52
4.3 Experimental results and discussion	58
4.4 Conclusion	66
Chapter 5 A Fiber Heterostructure based Optical Fiber Sensor for Detection of Phase Changes.....	68
5.1 Introduction	68
5.2 Experimental setup and operating principle of the sensor	69
5.3 Experimental results and discussion	75
5.3.1 Experimental preparation and setup	76
5.3.2 Experimental results	78
5.3.3 The use of signal processing to improve phase change detection	83
5.3.4 Experimental results for slow natural cooling	84
5.4 Conclusion	86
Chapter 6 Optical fiber Fabry-Perot sensor based on a singlemode-hollow core-singlemode fiber	88
6.1 Introduction	88
6.2 Experimental setup and operating principle.....	90
6.3 Experimental results and discussion	97
6.3.1 Experiment preparation and setup.....	97
6.3.2 Experimental results	99
6.4 Conclusion.....	108
Chapter 7 Conclusions and future work	110
7.1 Conclusions from the research	110
7.2 Future work.....	116
References	120

List of figures

Fig.1.1 Global energy consumption by sectors	2
Fig.1.2 Typical phase diagram.....	5
Fig.1.3 Classification of the PCMs.	8
Fig.1.4 Schematic comparison of stored energy by a PCM and a non-PCM.....	10
Fig.1.5 Typical supercooling curve	11
Fig.1.6 Typical enthalpy changes accompanying melting and solidification of a PCM exhibiting thermal hysteresis.....	13
Fig.2.1 Optical fiber in cylindrical coordinates.....	28
Fig.2.2 Schematic diagram of a Fresnel-reflection based fiber sensor. (a) a typical Fresnel fiber sensor head based on SMF. (b) a typical Fresnel fiber sensor system	31
Fig.2.3 Schematic diagram of optical fiber FPI.....	33
Fig.2.4 Schematic diagram of a typical fiber sensor based MZI.....	35
Fig.2.5 Typical in-line MZI fiber sensor based on a multimode-single mode-multimode structure	36
Fig.3.1 A typical DSC graph (DSC curve of n-octadecane).....	41
Fig.4.1 (a) Schematic diagram of the experimental setup. (b) 3D image of the sensing area.....	54
Fig.4.2 Simulated relationship between the reflected power ratio and the refractive index of the surrounding material of the probe.....	56
Fig.4.3 Reflected power ratio measured at different temperatures during the heating and cooling cycles of the n-octadecane sample: inflection point at ~28 °C in the heating experiment corresponds to the solid-liquid phase change and that at ~27.5 °C corresponds to the liquid-solid phase change on cooling.....	60
Fig.4.4 Photographs of the solid-liquid interface position at different temperatures: at 28°C both the thermocouple and fiber optic probe tips are clearly visible (the image corresponds to the inflection point in Fig. 4.3).....	63
Fig.4.5 Photographs of the solid-liquid interface position at different temperatures: at 27.5°C both the thermocouple and fiber optic probe tips are in contact with the solid surface (the image corresponds to the inflection point in Fig. 4.3).	64

Fig.5.1 (a) Schematic diagram of the experimental setup. (b) 3D image of the sensing area.....	71
Fig.5.2 Simulated output power distributions (left) and light intensity along the Z axis (right) when the sensor is immersed in: (a) solid, (b) liquid n-octadecane.	75
Fig.5.3 Experimental transmission spectrum of the sensor.....	76
Fig.5.4 Experimentally measured normalized output power during heating and cooling cycles.	78
Fig.5.5 Photographs of the sample at different temperatures during heating experiment.....	81
Fig.5.6 Photographs of the phase front at different temperatures during cooling.....	82
Fig.5.7 The result of the cooling naturally experiment.....	85
Fig.6.1 Schematic diagram of the sensor probe.	89
Fig.6.2 (a) Schematic diagram of the experimental setup. (b) 3D image of the sensing area	91
Fig.6.3 Experimental spectra of the fiber probes with different lengths of SMF-2.95	
Fig.6.4 Typical experimental reflected spectrum of the sensor probe.....	96
Fig.6.5 Temperature response of the sensor probe.	98
Fig.6.6 Heating experiments results: (a) dip wavelength shift during the heating cycle; Fig. 6.6 (b) dip wavelength shift after the sample melts into liquid...	101
Fig.6.7 Photographs of the solid-liquid interface position at different temperatures: at 28.5 °C both the thermocouple and fiber optic probe tips are clearly visible.....	102
Fig.6.8 The cooling experiment spectral results: (a) the dip wavelength shift during the cooling cycle (b) the dip wavelength shift before the sample solidifies.	104
Fig.6.9 Photographs of the solid-liquid interface position at different temperatures: at 28 °C both the thermocouple and fiber optic probe tips are clearly visible while they are immersed in the solid sample at 27.5 °C.....	106
Fig.6.10 The comparison of the heating and cooling experiment results.	107

Acronyms

DSC	Differential scanning calorimetry
FPI	Fabry-Perot interferometer
HCF	Hollow core fiber
MMF	Multimode fiber
NCF	No-core fiber
OSA	Optical spectrum analyzer
PCM	Phase change material
RI	Refraction index
SMF	Single-mode fiber
SNS	single-mode-no core-single-mode
SMS	singlemode-multimode-singlemode
SOC	State-of-charge
RIU	Refractive index unit
TES	Thermal energy storage

Chapter 1. Introduction

This Chapter introduces the research background, the concept of phase change materials (PCMs) and their role in the development of efficient thermal energy storage technologies in order to address the global demand for higher efficiency of energy use. The Chapter also provides a classification of PCMs, a brief description of their thermal and optical properties and an overview of their applications in thermal energy storage systems. The need for accurate detection of phase changes in PCMs is discussed, followed by a statement of the motivation and main objectives of the research undertaken. Finally an overview of the thesis layout is provided at the end of this Chapter.

1.1 Research background

According to the data provided by the BP plc [1], in 2019 the energy consumption by industry accounted for approximately half of all global energy consumption while feedstock fuels, residential and commercial buildings accounted for another 30% of the global energy consumption (Fig. 1.1). Given the urgent need for a reduction in the use of fossil fuels, it becomes increasingly important to maximize energy use efficiency in these two sectors. One way of achieving this goal in the residential sector is to transform the existing buildings into low energy consumption buildings. This solution requires a combination of renewable sources of energy and innovative energy storage technologies. Using thermal energy storage (TES) systems based on PCMs in buildings has become an increasingly important research topic in recent years.

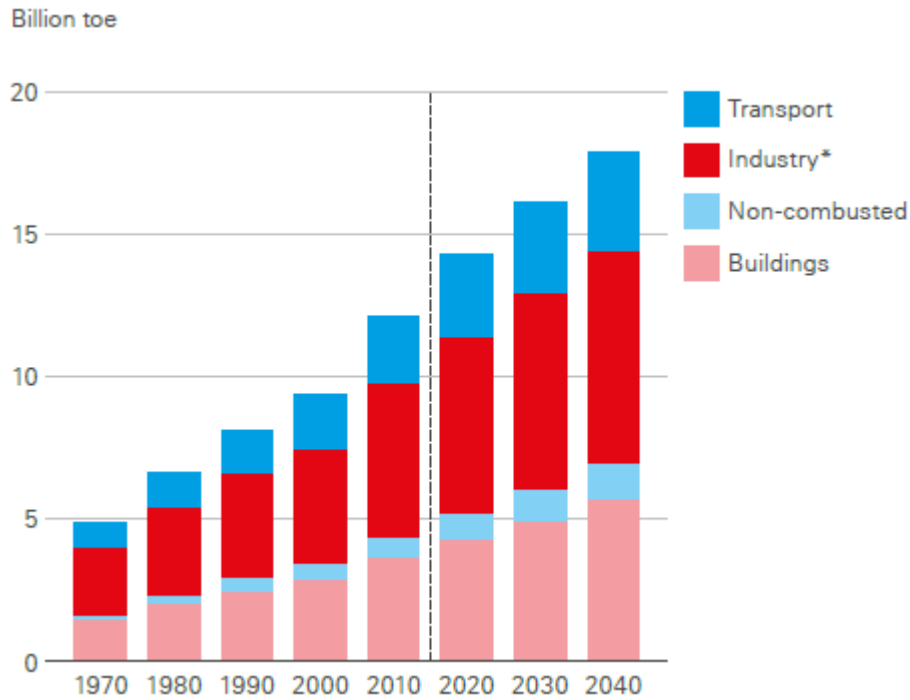


Fig.1.1 Global energy consumption by sectors [1].
 * Excludes non-combusted use of fuels.

The TES systems allow for the storage of energy during off-peak periods and the release of energy during the periods of high demand. A number of proposed designs involve wallboards as one of the best options for incorporating the PCMs into the buildings as a part of the TES systems [2]. For example, Zhang *et.al* proposed the concept of a brick wall filled with a PCM and investigated its thermal response, showing that the thermal storage capacity of such a wall is increased significantly, compared to the traditional solid brick wall [3]. Lai *et. al* proposed an aluminum honeycomb structure wallboard combined with a microencapsulated PCM [4]. This wallboard can shift the peak hours of electricity use in the summer and achieves lower module surface temperature compared to other wallboards. Another approach to increasing the energy efficiency of buildings involves incorporating PCMs in the building's heating system. Reza *et. al* developed an underfloor heating system combined with PCM wallboards. This underfloor

heating system has been installed in two test huts at the University of Auckland [5]. The test results indicate that the underfloor heating system reduces electricity consumption and cost by up to 35% and 44.4% respectively compared to a heat pump. Cheng *et. al* proposed an electronic underfloor heating system combined with a heat conduction-enhanced shape-stabilized PCM [6]. Analysis of its performance indicated a significantly improved energy efficiency compared to that of the conventional energy storage and air conditioning systems and allowed for a reduction in the thickness of thermal insulating materials.

To improve energy consumption efficiency in industry, it is very important to reduce or reuse the industrial waste heat. Industrial waste heat is the heat rejected from industrial processes in which the energy is used to produce high-value products [7]. Industrial waste heat is usually present in a thermal carrier, such as water, and can be considered as a potential energy source. If the industrial waste heat is captured and stored, it can be reused in other processes, or can be transformed into other types of energy, such as electricity [8]. In many cases, the yearly waste heat production is very large, which makes it a viable potential energy source. For example, the United State is estimated to produce the yearly waste heat of approximately 1501-1583 Petajoule (PJ), Canada is estimated to produce the yearly waste heat of approximately 2300 PJ. For Europe, it is nearly 1610-2708 PJ [9].

One way to improve the recovery of the industrial waste energy is utilizing PCMs for its storage [10]. For example, Akram *et. al* proposed a kiln which utilises PCM to improve the waste heat recovery [11]. The gap of the kiln shells is filled with the PCM (paraffin), to store the waste heat dissipated from the surface of the kiln. By doing that the waste heat recovery is increased by 3% to 8%. Huang *et. al*

investigated the thermal properties of a composite PCM (LiNO₃/KCl) in order to explore its long-term usage for the industrial waste heat storage [12]. By using the thermogravimetric analyzer and differential scanning calorimetry (DSC), they determined that the material remains stable in a relatively wide range of temperatures up to 315 °C. In addition, its thermal performance and phase change properties remain stable after several hundreds of melting/solidification cycles. Merlin *et. al* proposed a PCM-based industrial waste energy recovery system for the food processing industry [13], capable of storing up to 6 kWh, which is 15% of the total energy associated with the process.

From the above examples it can be seen that PCMs play an important role in the energy storage applications. The following sections introduce the basic properties and characteristics of PCMs.

1.2 Classification and properties of phase change materials

Phase change is a change of material from one physical state (solid, liquid or gas) to another, without any changes in its chemical content. Such changes often occur both in nature and numerous technological processes. Some materials with a high heat of fusion are capable of storing or releasing large amounts of energy when they undergo phase changes, such as melting or solidification at certain temperatures, and these materials are referred to as PCMs. Latent heat storage or release can be achieved when the PCMs undergo phase changes. For example, a typical PCM, n-octadecane, can absorb, store and release 244 kJ of energy per kilogram while undergoing a phase change.

A typical phase diagram for a PCM is shown in Fig. 1.2. As it can be seen from the figure, phase changes can occur as a result of changes in the pressure upon the material and/or its temperature. The black lines in the diagram indicate the phase boundaries. As the temperature and pressure change, the phase changes occur along these boundaries. The triple point is the point on the phase diagram where the boundaries intersect.

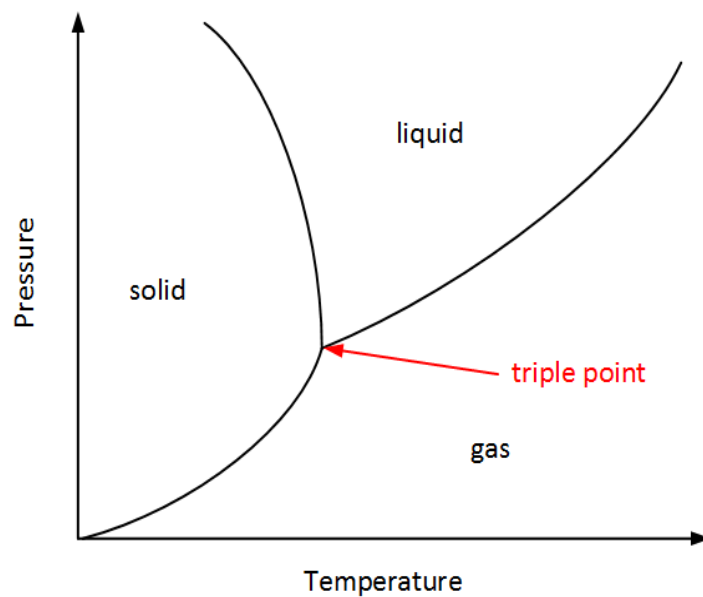


Fig.1.2 Typical phase diagram

The triple point marks the conditions at which the three phases can coexist. There are six possible phase changes that a material can typically go through, namely, freezing (liquid to solid), melting (solid to liquid), condensation (gas to liquid), vaporization (liquid to gas), sublimation (solid to gas) and deposition (gas to solid). Among all these types of phase changes, the solid-liquid and liquid-solid phase changes are widely used in many industrial applications and during these two processes, many parameters change, such as strain, density and RI, which the fiber sensors are sensitive to. Thus the research in this thesis will only focus on the solid-liquid and liquid-solid phase changes in PCMs.

1.2.1 Classification of PCMs

As there are a wide variety of PCMs, as an aid to a better understanding of the types and characteristics of the different PCMs, it is necessary to classify the different types of PCM. The classification of PCMs is as follows.

Organic PCMs

Organic PCMs are typically polymer materials with long chains of molecules, composed primarily of carbon and hydrogen. They tend to exhibit high orders of crystallinity when freezing and generally change their phase above 0 °C. Examples of organic PCMs include waxes, oils, fatty acids and polyglycols. Organic PCMs offer many advantages, for example, the absence of supercooling during freezing. Supercooling is a phenomenon when the material maintains its liquid state even when its temperature is lower than its freezing point. Supercooling may result in the PCM not releasing the stored energy when the temperature of the material is below freezing, which makes it difficult to accurately control the energy storage system. Since organic PCMs rarely possess supercooling, this makes them a good choice for energy storage applications. In addition, organic PCMs offer the advantages of being recyclable, chemically stable and non-reactive. The properties of some organic PCMs known as alkanes are summarized in Table 1.1 [14].

Table 1.1 Thermal properties of some well-known organic PCMs.

Organic PCMs	Melting point (°C)	Heat of fusion (kJ/kg)
Hexadecane	18.1	236
Octadecane	28.1	244
Nonadecane	32	222

Tricosane	47.5	234
Hexacosane	56.3	250
Triacontane	65.4	252

Inorganic PCMs

Inorganic PCMs are mainly salt hydrates and metallic materials. They offer the advantages of low cost and easy availability, higher heat storage capacity and thermal conductivity [15]. However, inorganic PCMs are also prone to supercooling, which can limit their practical application. The ability to accurately detect the presence of supercooling is necessary in inorganic PCMs in order to overcome this limitation. The thermal properties of some well-known inorganic PCMs are listed in Table 1.2 [15].

Table 1.2 Thermal properties of some well-known inorganic PCMs

Inorganic PCMs	Melting point (°C)	Heat of fusion (kJ/kg)
AlCl_3	192	280
LiNO_3	250	370
MgCl_2	714	452
$\text{Na}_2\text{P}_2\text{O}_7 \cdot 10\text{H}_2\text{O}$	70	184
$\text{Ba}(\text{OH})_2 \cdot 8\text{H}_2\text{O}$	78	266

Eutectic based PCMs

Eutectic PCMs consist of minimum of two components, and they solidify congruently without segregation, a phenomenon in which new solid and liquid compositions precipitate from the original PCM, at a temperature which is usually

lower than that of any of the mixture component [15]. Eutectic PCMs can be mixtures of organic-organic, inorganic-inorganic, or organic-inorganic PCMs. Eutectic PCMs typically have a very sharp phase change temperature, similar to pure materials. Compared to organic and inorganic PCMs, the most significant advantage of eutectic PCMs is their high thermal conductivity [16]. For energy storage systems based on PCMs, to achieve high input and output power, the heat charging and retrieval rate have to be sufficiently high, which is associated with a high thermal conductivity. Therefore using eutectic PCMs in thermal energy storage systems can lead to significant cost savings.

In summary the classification of PCMs is schematically illustrated in Fig. 1.3.

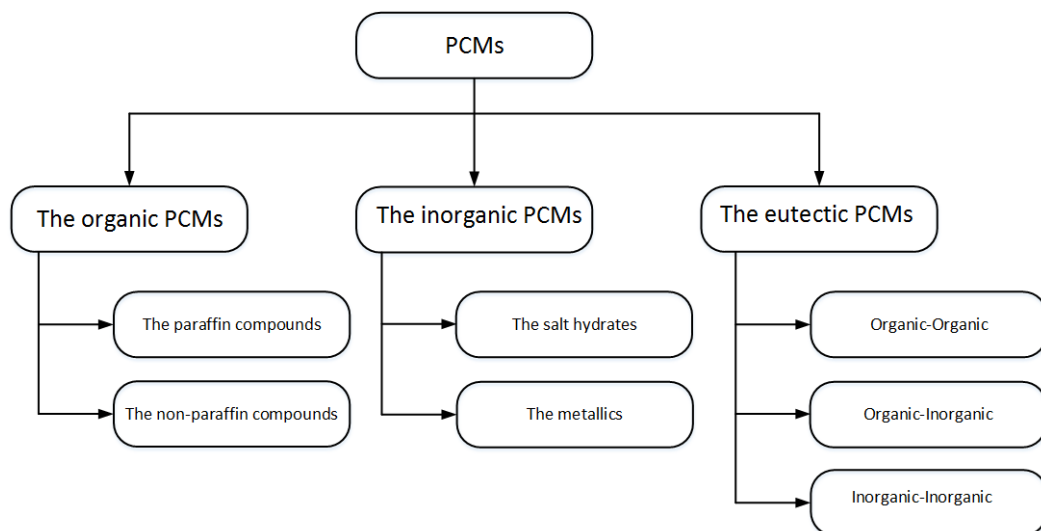


Fig.1.3 Classification of the PCMs.

1.2.2 Properties of phase change materials

The thermal properties of a material determine the material's response when heat passes through it. The main thermal properties of a material are its heat capacity, thermal expansion and thermal conductivity. In this research the main focus is on

the properties of PCMs that determine their performance within thermal energy storage systems (TES) briefly considered in the following sections.

Sensible heat

Sensible heat is the heat absorbed or released by a PCM as a result of increase or decrease of its temperature during which the PCM does not undergo any phase changes. It can be described as [17]:

$$Q_s = mc_{ap}(T_f - T_i) \quad (1.1)$$

where Q_s is the sensible heat, m is the mass of the PCM, c_{ap} is the average specific heat capacity of the PCM from the initial temperature to the final temperature, T_f is the final temperature and T_i is the initial temperature.

Sensible heat can be successfully utilized in TES systems with various non-PCMs, such as bricks or soils. For example, Ip *et. al* studied the long term thermal performance of a thermal storage unit in the form of a rammed earth-sheltered wall in a building and proved that the TES allowed to successfully maintain stable indoor conditions during winter times[18]. Dodoo *et. al* analysed and compared the thermal performance and life cycle of concrete and wooden buildings [19]. According to their study, concrete buildings have lower energy demand than wooden buildings, due to the higher thermal mass of concrete-based materials.

It should be noted however that a major drawback of the sensible heat storage is its low thermal capacity, in comparison to that associated with latent heat [20].

Latent heat

The latent heat is the heat absorbed or released during a phase transition (fusion, vaporization, sublimation) of a material to change its state. The latent heat of fusion (melting, solidification) be described by the following formula [17]:

$$Q_l = m\Delta h_m \quad (1.2)$$

where Q_l is the latent heat, m is the mass of the PCM. The term Δh_m is the specific enthalpy of the material changed as a result of melting or solidification. Specific enthalpy is a common term used in thermodynamics, defined as the energy for a given single unit mass of a substance, its units are typically kJ/kg.

Latent heat storage can be only achieved with PCMs. The main advantage of the latent heat storage over the sensible heat storage is that the energy density is higher. Fig. 1.4 shows the comparison of the energy storage capacity for materials with and without latent heat [21].

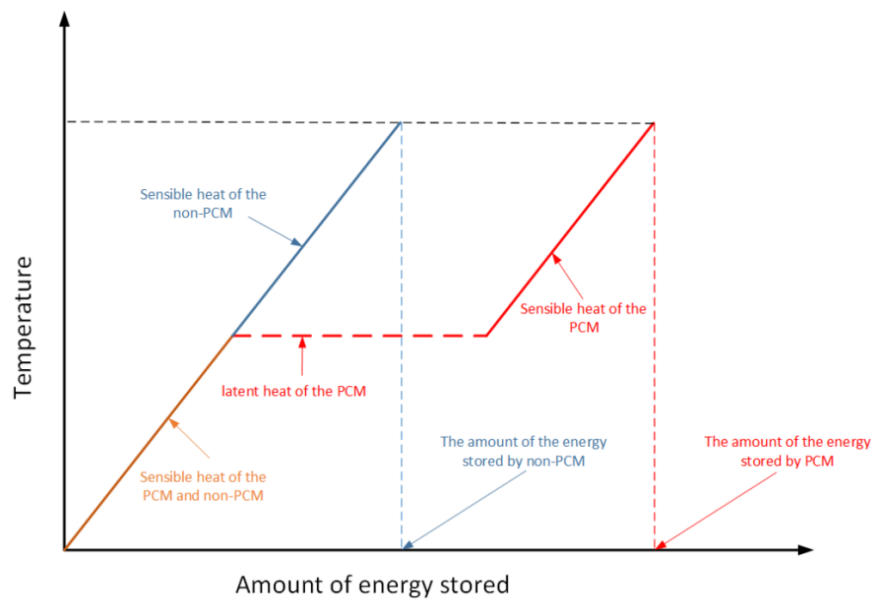


Fig.1.4 Schematic comparison of stored energy by a PCM and a non-PCM.

One can see from Fig. 1.4 that if both, PCM and non-PCM have the same sensible heat capacity, the total amount of energy stored by the PCM within the same temperature range will be significantly higher.

Supercooling

During the solidification process a liquid solidifies when its temperature decreases below the freezing point, due to the presence of seed particles (so-called nucleation agents), around which crystal structures can form. However, in the absence of a seed particle, even if the temperature is lower than the freezing point, the material can remain in the liquid phase, and this phenomenon is referred to as the supercooling [20]. Once the nucleation of the supercooled material is triggered, the temperature of the material increases to its real freezing point and it continues to solidify. A typical supercooling curve is shown in Fig. 1.5.

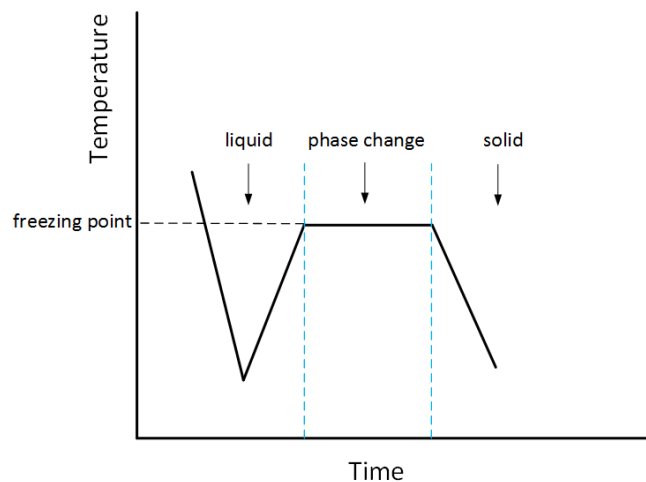


Fig.1.5 Typical supercooling curve

Supercooling can cause problems in the energy storage applications. Since a lower temperature is required to solidify a supercooled material, greater power is required to decrease the material's temperature and trigger the release of the latent heat, ultimately leading to a waste of energy. Therefore, the ability to accurately

detect the supercooling phenomenon is very important for improving the efficiency of energy storage in practical systems. After being used for several cycles, the thermophysical properties of a PCM may change [22], frequently leading to a higher likelihood of supercooling [23] and to a decrease in the efficiency of energy storage. Using thermocouples alone does not allow for the accurate detection of supercooling. However, combining thermocouples with fiber sensors has great potential for detection of supercooling. In this thesis, supercooling detection was not one of the objectives. However, the development of the method for detection of solid-liquid phase changes proposed in this thesis can be considered as the first step towards supercooling detection and will be the priority of the author's future work.

Thermal hysteresis

For some materials, the melting point does not coincide with the freezing point and such materials are said to exhibit thermal hysteresis. As an example, Fig. 1.6 illustrates typical changes in a PCM enthalpy (energy) accompanying its heating and cooling cycles. The red curve in the diagram shows changes in a PCM's energy during heating, where the step-like increase corresponds to the amount of latent heat required to melt the material into its liquid phase at the melting temperature. As the PCM is cooled subsequently from its liquid phase, the enthalpy change follows the blue curve. As soon as the material reaches its freezing point, there is also a step-like enthalpy change, corresponding to the latent heat released by the PCM as it solidifies.

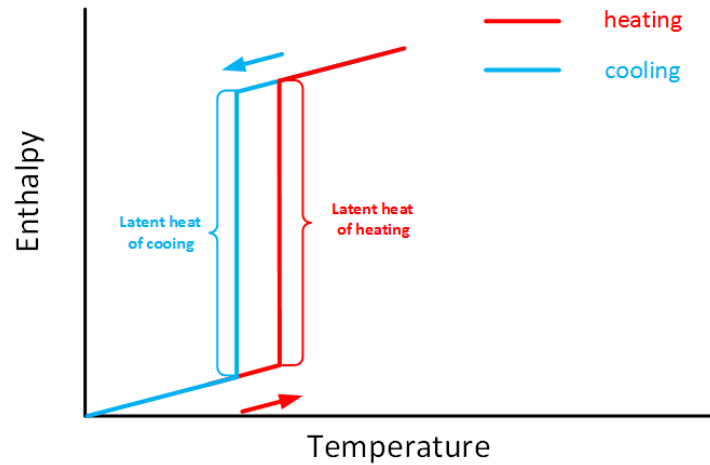


Fig.1.6 Typical enthalpy changes accompanying melting and solidification of a PCM exhibiting thermal hysteresis.

As it can be seen from the figure, the freezing temperature is lower than the melting temperature of the PCM so that during the cooling process the PCM remains in the liquid phase well past its melting point until it reaches the freezing temperature. The magnitude of thermal hysteresis may depend on the material surface roughness, on its crystal structure or seed particles size [24].

Thermal hysteresis makes temperature an unreliable indicator of the material's phase state and calls for an alternative means for the phase state detection, particularly if such a material is to be used in a TES.

Refractive index

During the phase change process, optical properties of PCMs change as well as many other physical parameters. One of the most important optical parameters of any material is its RI.

RI is a dimensionless number which characterizes the speed of light propagation within a certain material [25]:

$$n = \frac{c}{v} \quad (1.3)$$

where n is the RI, c is the speed of light in vacuum and v is the speed of light in the material.

RI is a function of a wavelength and an empirical relationship between the refractive index and wavelength of light for a particular transparent material is described by the Cauchy's equation [26]:

$$n = A + \frac{B}{\lambda^2} + \frac{C}{\lambda^4} + \dots \quad (1.4)$$

where A, B, C, etc., are coefficients that can be determined for a material by fitting the equation to measured refractive indices at known wavelengths. Usually it is sufficient to only use the first two terms of the equation.

In the phase change process, the temperature of the PCM increases or decreases while the energy is absorbed or released, and that could also influence the material's RI. The temperature dependence of the material's RI is called thermo-optic effect. The relationship between RI and temperature can be described as [27]:

$$\Delta n = \varepsilon \Delta T \quad (1.5)$$

where Δn is the RI change, ΔT is the temperature change and ε is the thermo-optic coefficient. The RIs of some well-known PCMs in liquid phase are shown in Table 1.3 [28-29].

Table 1.3 The RIs of some well-known PCMs in liquid phase

PCM	RI
Pentane	1.3577
Hexane	1.3756
Heptane	1.3878

Nonane	1.4058
Decane	1.412
Undecane	1.4173
Glycerine	1.4739

1.2.3 Applications of PCMs

Energy demand in practical domestic and industrial systems is not constant in time, but fluctuates due to a variety of factors. Fluctuations can be short term over a periods of hours or may follow a daily cycle or over a longer term, such as a seasonal cycle. TESs allow for the energy (often in the form of wasted heat) to be stored during the lower demand periods and to be released during the peak demand periods. Without storage a system providing energy must be designed to deal with the peaks in demand, even if these peaks are very infrequent. This can mean that without storage, an energy supply system can be effectively overprovisioned for much of its service life, which significantly increases capital and maintenance costs. The availability of energy from storage changes this dynamic, since with appropriate system design infrequent peak energy demands can be met from storage, without overprovisioning.

The unique thermal properties of PCMs are commonly utilized in many existing TES systems where heating or freezing of PCMs is accompanied by absorption or release of thermal energy by the PCM, as an effective means for energy conservation.

Smart buildings

Human demand for an indoor thermal comfort is a leading factor of gradual increase of the energy consumption by the building sector, which currently accounts for 30% of the overall energy consumption globally [30-31]. Therefore there is a need for an improvement of the thermal performance of buildings in order to achieve energy savings. In the past decades, multiple research efforts were focused on utilizing of PCMs for improvement of buildings thermal performance by utilizing their high-energy storage density. The main design solutions for incorporating PCMs in the buildings structure proposed to date include integrating PCMs inside walls, floors, ceilings, or alternatively into standalone heat or cold storage units [32].

For example, recently PCMs have been increasingly used to fabricate trombe walls (walls which are orientated to absorb as much solar energy as possible), or to fabricate wallboards, in order to increase their thermal inertia. Increasing the thermal inertia of the building allows for a better temperature stability inside the building without increasing its mass. Koo *et al.* studied the thermal performance of such a PCM wall both theoretically and experimentally and concluded that its maximum thermal storage capacity could be achieved when the phase change temperature of the PCM was close to room temperature [33]. Meng *et al.* evaluated the heat transfer performance of a PCM wall and developed a model describing the heat transfer based on the thermal resistance method and involving the heat isolation and heat absorption coefficients [34]. Lin *et al.* analyzed the thermal performance of a novel electric floor heating system with PCM plates [35]. Their results showed that circa 3.3 kWh of electric energy consumption could be shifted from the peak-demand to the off-peak period every day, which constituted 54% of the total electric energy consumption. Baek *et al.* analyzed the thermal

performance and energy saving potential of the PCM (aluminum) radiant floor heating system [36]. According to their research, such a system allowed for energy savings of about 2.4% annually.

Free cooling systems are promising sustainable technologies which aim to use the PCMs as a heat sink. For example, Zeinelabdein *et al.* proposed a novel free cooling system containing a PCM for hot-arid regions [37]. Their results indicate that their proposed system had the ability of reducing the cooling load substantially and the temperature of air supplied by the system was maintained well within the summer comfort zone of 25.5 and 30 °C for up to 14.5 h during the discharge period. Turnpenny *et al.* proposed a free cooling system which incorporated heat pipes embedded in a phase change material [38]. According to their research, a free-cooling system can prevent overheating of the office building in typical UK summer conditions.

Applications of PCMs in vehicles

Vehicles of all kinds play a key role in modern civilization, thus an improvement of their performance and maintenance becomes increasingly important. During a vehicle's operation, many of its components are required to work over a wide range of ambient temperatures, from sub-freezing to those reaching hundreds of degrees Celsius. The temperatures of certain components, such as the engine, are highly dependent on the speed of the vehicle. In such situations it could be very difficult to ensure uniform temperature of the various components of the vehicle, which could negatively affect both the vehicle performance and the lifetime of its components.

Due to their ability to absorb or release large amounts of energy during melting or solidification, PCMs are very popular in the design of thermal management systems for vehicles [39]. PCMs can serve as thermal buffers in order to stabilize the temperature of different parts, improving their performance and lifetime. The most common applications of PCMs in vehicles are the battery thermal buffering and the engine coolant loop thermal buffering. Electric and hybrid electric vehicles are growing in popularity due to the need for emission reduction and high energy efficiency. The performance of both types of vehicles is highly influenced by the battery performance and temperature instability during the charging and discharging cycles of the battery can significantly affect its performance and lifetime [40-41]. Sabbah *et al.* [42] compared the effectiveness of a passive (containing PCM) and active (air-cooled) thermal management systems by carrying out simulations and experiments. According to their research, under critical conditions, for example, at high operating temperatures or high discharge rates, the active thermal management system was not capable of keeping the temperature within the required operating range without expending significant fan power while the passive thermal management system could meet the requirements. Yan *et al.* [43] investigated the thermal performance of a battery thermal management system in dynamic cycling. According to their research, during the one charge/discharge cycle, there are two peaks in the temperature curve of the battery, which negatively affect its performance. However when a PCM was used in the system, the temperature peaks were suppressed and the performance of the battery improved. Babapoor *et al.* developed a novel thermal management system for batteries using carbon fiber-PCM composites [44]. Their experimental result illustrated that adding carbon fibers with the length of 2-mm and mass percentage

of 0.46% led to a better thermal performance under which the maximum temperature rise could be reduced by 45%.

Many vehicles use an water based coolant loop which is pumped to the radiator in order to remove the excess heat from the cooling system. However, in order to maintain lower temperatures larger radiators are required. To downsize the cooling system, many researchers attempted to incorporate PCMs in the design. Kim *et al.* [45] designed a novel small size engine cooling system with a heat accumulator based on a PCM. By utilizing the heat load averaging capabilities of the PCM, the size of the cooling system was decreased by 30% and the peak heat load was successfully averaged out.

Applications of PCMs in thermal storage

PCMs play an important role in TES applications [46]. Using PCMs in TES improves reliability and the performance of energy distribution networks [47]. Moreover, it also reduces the mismatch between the supply and the demand for the thermal energy. For example, PCMs are used in solar energy storage, where it is required to store the heat during the day for use at night. Kürklü *et al.* proposed a solar collector combined with water and a PCM [48]. Compared to the traditional hot water solar collectors, it demonstrated an improved absorption and insulation characteristics. Hammou *et al.* developed a hybrid TES system for managing simultaneously solar and electric energy based on a PCM (n-octadecane) [49]. The result of simulations carried out for the period over four consecutive winter months indicates that electric energy consumption may be reduced by as much as 30%.

Aerospace applications of PCMs

Maintaining a certain required temperature in space is very difficult due to the lack of atmosphere which usually provides warmth in the shade or protection from the

sun's heat. PCMs can be used to maintain a safe temperature inside a spacecraft, protecting crew members and equipment by adsorbing or releasing thermal energy during the phase change [50]. In 2016, NASA launched the "Phase change heat exchanger project", which tested a new type of heat exchanger that could help offset the heat in a spacecraft, enabling future missions to better regulate temperatures. Many other researchers showed great interest in this area. For example, Lafdi *et al.* reported numerical research predicting the thermal performance of graphite foams infiltrated with PCMs for space and terrestrial energy storage systems [51]. Their results showed that the average output power of the new storage system could be increased by more than eight times, while for terrestrial applications, the average output power using carbon foam with 97% porosity was about five times greater than that of the system using pure PCM. Cui *et al.* developed a model solar receiver composed of three different PCMs [52]. The three-PCMs solar receiver improved the energy storage rate and reduced both the fluctuation of working fluid temperature and the weight of the heat receiver.

1.3 The need for accurate detection of phase changes in PCMs

As mentioned in the former sections, the utilisation of PCMs is important to improve energy efficiency. However, to maximize the energy efficiency, it is extremely important to realize an accurate means of insitu detection of phase changes within PCMs. The solid-liquid phase state information for a PCM can be utilised as the basis for operating a PCM base thermal energy storage system. If such a storage system is operated without adequate information regarding its phase

state, then there is a strong chance that energy could be wasted, for example on unnecessary heating of the material. In the past few decades, many phase change detection methods were proposed, such as differential scanning calorimetry (DSC) or X-ray tomography and radiography. However, they all share a critical disadvantage of not being capable of detecting phase change in situ, which is important for real-world thermal energy systems. These traditional methods are briefly reviewed in Chapter 3.

Optical fiber sensors have had notable successes as sensors for a wide variety of measurands, on physical scales from kms to nm. They have a demonstrated adaptability to deal with different sensing challenges, many of them involving embedded or in-situ applications in materials. In particular fibre sensors have been successfully used where the sensor was embedded in a solid material or when immersed in liquids, making fibre sensors a strong candidate for use in a PCM which can be either a liquid or a solid. A complete review of possible optical fibers sensors is presented in a subsequent chapter of this thesis but for now, in order to provide a context for the Aims and Objectives of this research, some preliminary comments on optical fiber sensors are presented below.

Optical fiber sensors utilize changes in one or more optical or physical properties of the material during the phase change, for example changes in refractive index, transparency, light scattering or material density. Optical fiber sensors possess many advantages such as high sensitivity, low thermal mass, low thermal conductivity and small size, immunity to electromagnetic interference and possibility of real time and remote monitoring, making them potentially a feasible method for in situ phase change detection. However, fiber sensing for solid-liquid

phase change is still at a very early stage and up to now there have been only a few papers on this topic.

Although optical fiber sensing has great potential to be applied to phase change detection, there are several challenges which must be addressed. One of the biggest challenges is the well-known cross-sensitivity of many fiber optic sensors to different parameters. This is important since during the phase transition process several parameters (such as RI, temperature, strain, etc.) acting upon the sensor probe change simultaneously, and all of them could affect the sensor's response resulting in inaccuracies of phase change detection. A common approach to eliminating this cross-sensitivity is increasing the number of parameter-specific sensors, to allow one to compensate for unwanted cross-sensitivities. However, this approach increases the complexity of the method [53-54].

Another challenge is that solid-liquid phase changes are frequently accompanied by random perturbations that may affect the performance of the fiber optic sensors. For example, thermal convection during the heating of a material sample [55], and the variation of the thermal convection flows due to the phase change often cause the formation of air bubbles that tend to move from the bottom to the top of a container which may result in random perturbations of the sensor's position and shape and in turn lead to measurement inaccuracies.

In summary phase change detection is a much-needed technique in many application areas. However, the existing phase change detection methods have various shortcomings, with the temperature measurement method not being reliable due to the supercooling, and non-temperature measurement methods not being capable of detecting the phase change in-situ, which is important in both

industrial and home energy storage applications. It is thus necessary to find a new method to detect the phase change. Optical fiber sensing has the advantages of suitability for use in opaque materials, low cost, high resolution, and most importantly capability of in-situ measurements in real time. However until now, there has been very little research focused on phase change detection using fiber optic sensors, particularly for PCMs. Moreover, a number of challenges arising from cross-sensitivity of optical fiber sensors to multiple parameters and their susceptibility to measurement inaccuracies due to random perturbations during phase transitions have not been properly addressed to date. The research presented in this thesis aims to overcome these challenges by the development of accurate optical fiber sensors for in-situ phase change detection.

1.4 Aim and objectives of the thesis

The main aim of this research is to develop a new and reliable method for in-situ detection of phase states and phase changes in PCMs, based on optical fiber sensors. The specific objectives of this research are as follows:

1. Identify, investigate and analyze the most suitable types of optical fiber sensors as a basis for the sensing system capable of monitoring liquid-solid phase transitions in PCMs.
2. Develop appropriate analytical models to establish the relationship between physical parameters of PCMs during the phase changes and the corresponding output signals (or spectra), such as power ratio or interference dip wavelength shift of the selected fiber optic sensors.

3. Develop an experimental setup capable of accurate control of phase changes in the material sample, including control of the speed of heating/cooling and thermal convection. Identify a suitable PCM for verification of the analytical models and an experimental demonstration of the potential of the proposed sensor system.
4. Identify the factors that cause random disturbances of the sensors' performance and develop techniques to minimize the disturbances and increase the reliability of detection using optical fiber sensors and in addition develop methods to overcome the cross-sensitivity issues of individual fiber sensors.

1.5 Layout of the thesis

In **Chapter 1** the research background is introduced, including the concept, classification and the applications of PCMs and the most popular phase change detection methods are reviewed. The motivation, aim and objectives of the research are also introduced in this first chapter.

In **Chapter 2**, some typical fiber sensors (Fabry-Perot interferometer (FPI), Mach-Zehnder interferometer (MZI) and Michelson interferometer (MI)) are introduced, including the working principles, classification and applications of different fiber sensor structures. In this chapter the suitability of the typical fiber sensors structures for the detection of phase change is also discussed.

In **Chapter 3**, existing methods for the detection of phase changes in PCMs and other phenomena associated with a phase transition are reviewed. Both optical and

non-optical methods are introduced, analyzed and compared. A discussion on the advantages and disadvantages of both types of method is included.

In **Chapter 4** an all optical fiber Fresnel reflection sensor for detecting the solid-liquid phase change in n-octadecane is proposed and experimentally demonstrated. The results of this work suggest that such a simple optical fiber sensor can be used for detection of liquid-solid phase changes in other materials with similar to n-octadecane thermo-optic properties.

In **Chapter 5** a novel singlemode-no-core-singlemode (SNS) fiber optic sensor is proposed and experimentally demonstrated. The sensor probe is fabricated by splicing a short section of a NCF between two sections of standard SMFs. This sensor allows for the determination of the specific phase state based on a single measurement of the output sensor power after an appropriate calibration. Moreover, by using the SNS sensor the influence of small fluctuations of the output power due to the presence of air bubbles, voids and impurities can be eliminated, which makes the proposed sensor much more reliable in practice.

Chapter 6 focusses on another novel Fabry-Perot fiber structure fabricated by splicing a short section of a HCF between two single-mode fibers. Such a sensor can also be used for detection of the material's phase state at a particular point of its volume. Compared to the SNS fiber sensor, the Fabry-Perot sensor allows one to overcome the dependency of the sensor's performance on refractive index of the PCM, whilst also offering a better insight into the phase change mechanism in such materials.

Finally in **Chapter 7**, the key results and achievements are summarized, overall conclusions are presented and a brief overview of the future work is provided.

Chapter 2 Fundamentals of Optical Fiber Sensors for Phase Change Detection

Most commonly interferometric optical fiber sensors can be classified into four categories: Fabry-Perot interferometers (FPIs), Mach-Zehnder interferometers (MZIs), Michelson interferometers (MIs) and Sagnac interferometers. Among all the four types, the FPIs and MZIs have been most significant in this research. The working principle of these two types of fiber interferometers and their performance in terms of RI and strain sensing will be reviewed to analyze their potential for the detection of phase changes in PCMs.

2.1 Light propagation in an optical fiber

Light is an electromagnetic wave whose propagation in the optical fiber can be described by Maxwell's equations [56]:

$$\begin{aligned}\nabla \times \mathbf{E} &= -\frac{\partial \mathbf{B}}{\partial t} \\ \nabla \times \mathbf{H} &= \mathbf{J} + \frac{\partial \mathbf{D}}{\partial t} \\ \nabla \cdot \mathbf{D} &= \rho \\ \nabla \cdot \mathbf{B} &= 0\end{aligned}\tag{2.1}$$

where \mathbf{E} is the electric field vector, \mathbf{H} is the magnetic field vector, \mathbf{B} is the magnetic induction vector, \mathbf{D} is the electric displacement vector, \mathbf{J} is the current density vector and ρ is the charge density. The wave equations for the electric and magnetic field vectors are [56]:

$$\nabla^2 \mathbf{E} + \nabla \left(\mathbf{E} \cdot \frac{\nabla \varepsilon}{\varepsilon} \right) = \mu_0 \varepsilon \frac{\partial^2 \mathbf{E}}{\partial t^2} \quad (2.2)$$

$$\nabla^2 \mathbf{H} + \frac{\nabla \varepsilon}{\varepsilon} \times \nabla \times \mathbf{H} = \mu_0 \varepsilon \frac{\partial^2 \mathbf{H}}{\partial t^2}$$

where ε is the dielectric constant, μ_0 is the magnetic permeability in vacuum. Considering $\nabla \varepsilon$ is 0 in optical fibers, equations 2.2 for a monochromatic wave can be written as

$$\nabla^2 \mathbf{E} + \mathbf{n}_i^2 k_0^2 \mathbf{E} = 0 \quad (2.3)$$

$$\nabla^2 \mathbf{H} + \mathbf{n}_i^2 k_0^2 \mathbf{H} = 0$$

where n_i is the RI of the fiber, $i=1,2$ represents fiber core and cladding respectively, k_0 is the wave number in vacuum. Equations 2.3 are referred to as the Helmholtz equations. Assuming E_{z1} and H_{z1} are the projections of electric and magnetic field amplitudes on z axis in the fiber core, E_{z2} and H_{z1} are the projections of electric and magnetic field amplitudes on z axis in the fiber cladding. E_{z1} , E_{z2} , H_{z1} and H_{z2} are on the boundary between the core and cladding. The boundary conditions in optical fiber can be written as [56]

$$E_{z1} = E_{z2} \quad (2.4)$$

$$H_{z1} = H_{z2}$$

The equations below are the solutions of the equations (2.3) in cylindrical coordinates.

$$\mathbf{E} = \mathbf{E}(r, \varphi)e^{j(\omega t - \beta z)} \quad (2.5)$$

$$\mathbf{H} = \mathbf{H}(r, \varphi)e^{j(\omega t - \beta z)}$$

where z -axis represents the electromagnetic wave propagation direction in the fiber, as Fig.2.1 shows. β is the propagation constant.

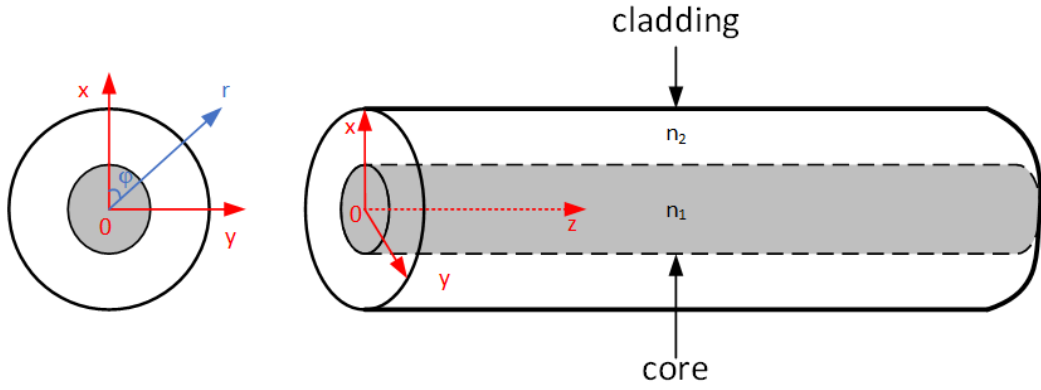


Fig.2.1 Optical fiber in cylindrical coordinates.

After substituting equations 2.5 to equations 2.3, the Helmholtz equations can be written as:

$$\frac{\partial^2}{\partial r^2} E_z + \frac{1}{r} \frac{\partial}{\partial r} E_z + \frac{1}{r^2} \frac{\partial^2}{\partial \varphi^2} E_z + (n_i^2 k_0^2 - \beta^2) E_z = 0$$

$$\frac{\partial^2}{\partial r^2} H_z + \frac{1}{r} \frac{\partial}{\partial r} H_z + \frac{1}{r^2} \frac{\partial^2}{\partial \varphi^2} H_z + (n_i^2 k_0^2 - \beta^2) H_z = 0 \quad (2.6)$$

E_z, H_z are the projections of electric and magnetic field amplitudes on z axis. For solving equations 2.6, assuming E_z, H_z are

$$E_z(r, \varphi, z) = AR(r)\Phi(\varphi)e^{-i\beta z} \quad (2.7)$$

$$H_z(r, \varphi, z) = BR(r)\Phi(\varphi)e^{-i\beta z}$$

A, B are constants. For solving equations 2.6, equations 2.7 can be substituted to equations 2.6, then equations 2.6 can be written as

$$\frac{\partial^2 E_z}{\partial r^2} + \frac{1}{r} \frac{\partial E_z}{\partial r} + \left(n^2 k_0^2 - \beta^2 - \frac{m^2}{r^2} \right) E_z = 0 \quad (2.8)$$

$$\frac{\partial^2 H_z}{\partial r^2} + \frac{1}{r} \frac{\partial H_z}{\partial r} + \left(n^2 k_0^2 - \beta^2 - \frac{m^2}{r^2} \right) H_z = 0$$

Where m is an integer. Equations 2.8 are the Bessel differential equations. Assuming a is the radius of the fiber core, and the RI distribution of the optical fiber can be written as

$$n_i(r) = \begin{cases} n_1 & r \leq a \\ n_2 & r > a \end{cases} \quad (2.9)$$

The solutions of equations 2.8 can be written as

$$E_z = \begin{cases} A_1 J_m \left(\frac{U}{a} r \right) & r \leq a \\ A_2 K_m \left(\frac{W}{a} r \right) & r > a \end{cases} \quad (2.10)$$

$$H_z = \begin{cases} B_1 J_m \left(\frac{U}{a} r \right) & r \leq a \\ B_2 K_m \left(\frac{W}{a} r \right) & r > a \end{cases}$$

J_m is the m^{th} order of Bessel function, K_m is the m^{th} order of modified Bessel function of the second kind. A_1, A_2, B_1 and B_2 are constants. U and W can be written as

$$U^2 = (k_0^2 n_1^2 - \beta^2) a^2 \quad (2.11)$$

$$W^2 = (\beta^2 - k_0^2 n_2^2) a^2 \quad (2.12)$$

The projections of electric and magnetic field amplitudes on other axes can be described as follows.

$$E_r = \frac{-i}{\omega^2 \mu_0 \varepsilon - \beta^2} \left(\beta \frac{\partial E_z}{\partial r} - \frac{im\omega\mu_0}{r} H_z \right) \quad (2.13)$$

$$E_\varphi = \frac{-i}{\omega^2 \mu_0 \varepsilon - \beta^2} \left(\frac{im\beta}{r} E_z + \omega\mu_0 \frac{\partial H_z}{\partial r} \right) \quad (2.14)$$

$$H_r = \frac{-i}{\omega^2 \mu_0 \varepsilon - \beta^2} \left(\beta \frac{\partial H_z}{\partial r} + \frac{im\omega\varepsilon}{r} E_z \right) \quad (2.15)$$

$$E_\varphi = \frac{-i}{\omega^2 \mu_0 \varepsilon - \beta^2} \left(\frac{im\beta}{r} H_z - \omega\varepsilon \frac{\partial E_z}{\partial r} \right) \quad (2.16)$$

Equations 2.10-2.16 describe the electromagnetic field in optical fiber.

2.2 Optical fiber sensors and their applications

As mentioned in the first chapter, optical fiber sensors have demonstrated adaptability to deal with different sensing challenges including sensing in-situ in liquids and solids, which shows the potential for detecting phase change in-situ in a PCM. In addition, optical fiber sensors have been successful applied on wide variety of measurands, on the physical scale from kms to nm, which means that the optical fiber sensors can achieve both measurement over an area and point measurement, which would satisfy variety of measurement needs of phase change detection in industry. Based on these two points, the optical fiber sensors have been chosen as candidates for phase change detection in this research. In this section, several types of fiber optic sensors relevant to this research will be briefly

introduced as a background to the experimental work described in subsequent chapters.

2.2.1 Fresnel-reflection based fiber sensor

A Fresnel-reflection based fiber sensor is the simplest sensor configuration used in this study. It works based on the principle of Fresnel reflection from the cleaved end of a section of an optical fiber used as sensor probe. Fig. 2.2(a) shows Fresnel reflection from a cleaved fiber end, while Fig. 2.2(b) shows a simplified schematic diagram for a Fresnel-reflection based fiber sensor system which uses an optical circulator to pass the reflected signal from the fiber end to a power meter.

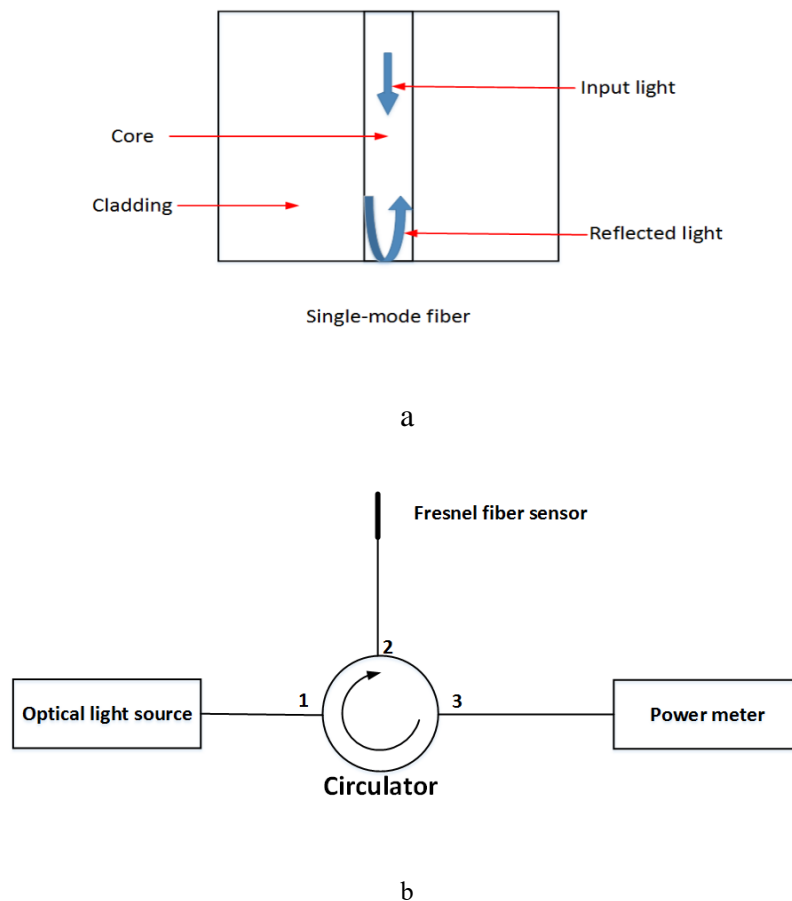


Fig.2.2 Schematic diagram of a Fresnel-reflection based fiber sensor. (a) a typical Fresnel fiber sensor head based on SMF. (b) a typical Fresnel fiber sensor system

Input light is launched into the fiber probe via an optical circulator, reflected back from the cleaved end of the fiber, passes through the circulator again and is eventually collected at the power meter. The output power measured by the power meter depends on the RI of the medium surrounding the sensor probe. By measuring the reflected power it is possible to determine the surrounding RI [57] and with a suitable calibration other measurands such as the solute concentration [58] or magnetic field intensity [59], in which a change in the measurand results in a change in the RI. More importantly, by continuously monitoring the changes in the surrounding RI this simple probe can be applied to detection of phase changes in various materials as was demonstrated by Mani *et al.* [60] who reported a Fresnel reflection fiber sensor for monitoring the crystallization of water and an aqueous solution of NaCl. The main focus of their work was on the studies of crystallization of distilled water under supercooling conditions as it was subjected to rapid cooling using liquid nitrogen. This work shows the potential of Fresnel fiber sensor for detecting the phase change both in heating and cooling cycles.

2.2.2 Interferometric fiber sensors

Bulk optic and fiber optical interferometers utilise the interference between light carried along two paths with different effective lengths. If a measurand such as strain alters the length of one of the light paths, then the interference changes as a function of the level of strain, to form a simple strain sensor. There are a wide variety of interferometric configurations, with the most relevant to this research described below.

Fabry-Perot fiber interferometer. A typical FPI is formed by placing two highly reflective mirrors in parallel to form a Fabry-Perot cavity. The two mirrors are

separated by a short distance to reflect the light beams within the cavity resulting in the interference between them. Fig 2.3 shows a typical FPI which is formed by splicing a section of a hollow core fiber (HCF) between two SMFs. Since the core of the HCF is air, interfaces between the HCF and two SMFs act as the mirrors and the HCF core as the cavity.

Both intrinsic and extrinsic FPIs work on the same principle.

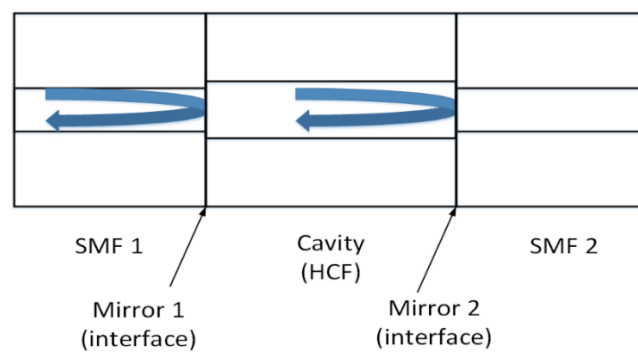


Fig.2.3 Schematic diagram of optical fiber FPI.

Multiple reflections and interference within the Fabry-Perot cavity produce multiple periodic dips within the FPI spectrum, whose positions are determined by the phase difference between the reflected light beams as described in [56]:

$$\delta = \frac{2\pi}{\lambda} n2L \quad (2.4)$$

where L is the FPI cavity length, λ is the wavelength of the incident light beam, and n is the RI of the cavity material. Any changes in the phase difference induced by external factors, such as strain, cause a wavelength shift of the interference dips, and the value of the shift can be related to the measurand of interest.

Ferreira *et al.* proposed a fiber FPI refractometer with a micron-sized hollow-tube silica fiber cavity with a sensitivity of 1053.44 nm/refractive index unit (RIU) [61].

Chen *et al.* proposed a fiber FPI, which is fabricated by splicing a short section of a thin core fiber to SMFs at both ends with an average RI sensitivity of 240 dB/RIU over a wide RI range of 1.3326–1.4305 and a maximum sensitivity of 1110.7 dB/RIU at the RI of 1.4305 [62]. Quan *et al.* proposed an FPI fabricated based on Vernier effect by splicing a section of photonic crystal fiber to a fiber tube [63]. The sensor probe length was approximately 340 μm with two FP cavities, one is formed by the fiber tube and the other one is formed by the photonic crystal fiber. These two cavities are fabricated for generating Vernier effect, to amplify the sensitivity by orders of magnitude. In this case, the sensor provided an ultra-high RI sensitivity of 30899 nm/RIU.

The FPIs can be also applied to sensing of strain. As the strain is applied to the FPI cavity, its length increases, which causes the phase difference between the interfering light beams to change. If the cavity material possesses photo-elastic effect, the effective RI of the cavity will change in response to the strain, which will also affect the light interference. Thus by observing the wavelength shift of the selected interference dip, the strain can be detected. Zhibo *et al.* proposed an extrinsic FPI strain sensor where the cavity was formed by a small air gap between two cleaved SMFs inside a glass capillary [64]. The demonstrated strain sensitivity was 40.178 nm/ $\mu\epsilon$. Zhichao *et al.* proposed an FPI with a 49 mm long hollow core fiber with strain sensitivity of 115.57 nm/ $\mu\epsilon$ in the range of strains of up to 1000 $\mu\epsilon$ [65].

Mach-Zehnder interferometer

In an MZI the interference occurs between two beams of coherent light from a single light source that travel by different paths. Fig. 2.4 shows a schematic

diagram of a typical fiber sensor based MZI. The light is split by a 3 dB coupler into the reference arm and the sensing arm, which are later re-coupled by another 3 dB coupler and monitored by a light detector. When used as a sensor, the reference fiber arm is isolated from any influence while the sensing fiber arm is exposed to the measurand. If the measurand, such as temperature, strain or the RI of the sample changes, the effective light path of the sensing arm will change. Variations in the parameters of the sensing arm result in the variation of the phase difference between the two beams, and lead to changes in the wavelength of the output interference pattern recorded by the optical spectrum analyzer (OSA). By measuring the changes at the detector the change in the measurand can be determined assuming proper calibration has taken place.

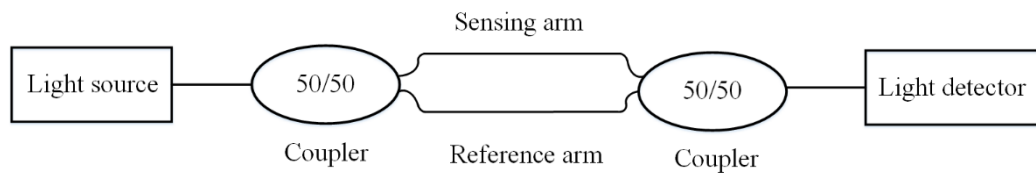


Fig.2.4 Schematic diagram of a typical fiber sensor based MZI

Recently the traditional MZI design illustrated in Fig. 2.4 has been increasingly replaced by in-line MZI fiber sensors where both the light paths are contained within the same fiber section. A typical in-line MZI fiber sensor based on a multimode-single mode-multimode fiber structure is shown in Fig. 2.5. As the input light from the multimode fiber 1 (MMF1) enters the SMF section, both core and cladding modes are excited within the SMF. When the light eventually re-couples into the second MMF (MMF2), the cladding and the core modes excited within the SMF section interfere with each other creating multiple interference dips in the transmission section. The phase difference between the cladding mode

and the core mode of the SMF can be described as in [66]:

$$\Delta\varphi = \frac{\lambda^2}{\Delta n_{eff}L} \quad (2.5)$$

where λ is the characteristic wavelength, which is the wavelength of the interference dip, Δn_{eff} is the difference between the effective RIs of the cladding and core modes and L is the length of the SMF. In addition to the multimode-singlemode-multimode structure above, there are also many other MZIs fabricated by using different types of fibers. They all share the same operating principle based on multimode interference.

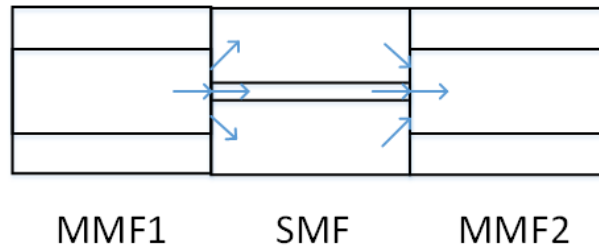


Fig.2.5 Typical in-line MZI fiber sensor based on a multimode-single mode-multimode structure

Measurement of RI with MZI fiber interferometers is typically achieved due to the sensitivity of the RI of the cladding modes within the middle section to the surrounding RI. For example, Cheng *et al.* proposed an MZI based on a slight tapered photonic crystal fiber for RI sensing and demonstrated the sensitivity of 1600 nm/RIU for the probe with a length of approximately 2 cm [67]. Li *et al.* proposed a twin-core fiber based MZI for RI sensing [68]. The sensor was fabricated by splicing a section of a twin-core fiber between two sections of SMF with a reported sensitivity of 10981 nm/RIU for a probe length of 200 μm .

MZIs are also frequently applied in sensing of strain. Xinran *et al.* proposed an

MZI for strain sensing based on a 35 mm long section of a twin core photonic crystal fiber spliced with two SMFs with strain sensitivity of $1.78 \text{ pm}/\mu\epsilon$ [69]. Avila-Garcia *et al.* proposed a core-offset strain-sensitive MZI structure with a maximum sensitivity of $7.46 \text{ pm}/\mu\epsilon$ [70]. Recently many MZIs have been fabricated using fiber tapering method, allowing for a significant improvement in the strain sensitivity, which is due to the interference dips are formed by the evanescent wave, which is exposed in the sample. Ke *et al.* proposed an MZI for strain sensing based on a S-tapered MMF [71]. This structure was realized by non-axially tapering a traditional singlemode-multimode-singlemode fiber into an S-shape using a fusion splicer. This sensor had a high strain sensitivity of $-103.8 \text{ pm}/\mu\epsilon$ while the length of the probe was 2 cm.

In summary, fiber based FPI and MZI sensors have a number of advantages for sensing of RI and strain in PCMs for detection of phase changes, such as small size, low thermal mass, low thermal conductivity and high sensitivity. In this research a number of FPI and MZI structures were chosen for the development of new methods of phase change detection in PCMs. These types of sensors are sensitive to RI, temperature or strain and these parameters change following the phase transition. Since fiber sensors are capable of detecting these parameters, therefore fiber sensors have the potential of detecting phase change. The current fiber sensors for phase change detection will be reviewed in the next chapter.

Chapter 3 Overview of methods for the detection of phase changes in PCMs

3.1 Introduction

Since most of practical applications of PCMs including those in smart buildings, vehicle cooling systems, TES and space technology rely on the phase change process, it is important to develop practical techniques for accurate detection of the phase state and phase changes. One of the most critical barriers in industry-wide applications of PCM based technologies is the full control of phase transition processes, e.g. charging and discharging of latent heat TES systems [72]. The accurate estimation of the stored energy (enthalpy), also referred to as the state-of-charge (SOC) of latent heat TES systems, is more complex than the sensible heat in TES systems where the stored energy is a linear function of the mass of a PCM, its average specific heat capacity and its temperature change. A phase transition (solidification or melting) in the latent heat TES systems is associated with the release or absorption of a large amount of latent heat, which cannot be directly measured as a temperature change usually due to the isothermal conditions or effects of supercooling and thermal hysteresis. To be able to measure the SOC correctly it is important to distinguish if the PCM is either in its liquid or solid state. For TES systems based on PCMs, the information about the SOC is essential from the control strategy point of view, for example, to decide when charging or discharging processes should be stopped or to estimate the stored energy for the dynamic power demands. Therefore, a robust, reliable and accurate sensor is deemed needed to determine the SOC of the PCM at any time [73]. Moreover, such experimental methods could become an important tool for development,

validation and implementation of new advanced melting and solidification numerical models for PCMs which include such effects as supercooling or thermal hysteresis [74, 75].

This section provides an overview of the existing methods for the detection of phase changes in PCMs.

3.2 Common methods for the detection for phase changes in PCMs

As discussed in the former section, the technique of phase changes detection is necessary for industrial applications, thus researchers developed many methods of detection for phase changes in PCMs. In this section, the well-known methods will be briefly introduced.

Direct observation

This method allows to detect phase changes in transparent materials [76], such as water. However, it is not applicable to opaque materials, or if the detection is required in a setup where direct observation is impossible.

X-ray tomography and radiography

These methods allow for the visualization of the solid-liquid interface regardless of optical transparency on a microscopic scale due to the density changes caused by the phase transitions [77]. Both methods suffer from the disadvantage of relatively high cost and being laboratory-based, lack portability. In addition, both of the methods require a safety system to avoid the exposure of human personnel to radiation.

Resistance diagnostics

As most materials show changes in electrical resistance upon melting, the variations of the resistance of the PCMs can be used to detect the solid-liquid phase change [78]. This measurement technique involves letting electric current flow through the sample during its phase transition and measuring the changes in resistance. It is a low cost technique compared with the X-ray, but it suffers from complexity. Moreover, the accuracy of the method depends on the size of the material sample, so that for a certain cross-sectional area, the value of the PCM resistance is determined by the length of the material sample. If the length of the sample is so small that the resulting value of the resistance is smaller than the resolution of the measurement equipment, it is not possible to detect the phase change, which means that for resistance diagnostics it can be difficult to achieve high spatial resolution phase change detection in the case of multi-point measurements.

Differential scanning calorimetry (DSC)

This method is one of the most popular techniques for phase change detection and it involves measurements of the difference in the amount of heat required to increase the temperature of the PCM sample and reference material as a function of temperature. Both the PCM sample and reference material are maintained at nearly the same temperature throughout the experiment. The principle underlying this method is that when the sample undergoes phase change, more or less heat is required to flow into the sample than into the reference, to make sure that the temperatures of the sample and the reference are the same. Whether more or less heat is required depends on whether the process is exothermic or endothermic.

When the sample undergoes melting, since it is an endothermic process and the sample absorbs heat in melting, more heat must flow into the sample to increase the temperature of the sample at the same rate as the reference. Likewise, when the sample undergoes solidification, since it is an exothermic process and the sample releases heat in solidification, less heat is required to increase the temperature of the sample at the same rate as the reference. By observing the changes in the heat flow, the method can be used to determine the phase state within a very small volume of the material sample. As was demonstrated by Lazaro *et al.* [79], the measurement accuracy of DSC depends significantly on the cooling and heating rates. A typical DSC figure (DSC curve of n-octadecane) is shown in Fig. 3.1 [80]. It should be noted that DSC does not allow for the determination of the phase state at specific points within the sample's volume, and thus is unsuitable for energy storage applications which involve large PCM volumes, a disadvantage which is also shared by some of the other traditional methods.

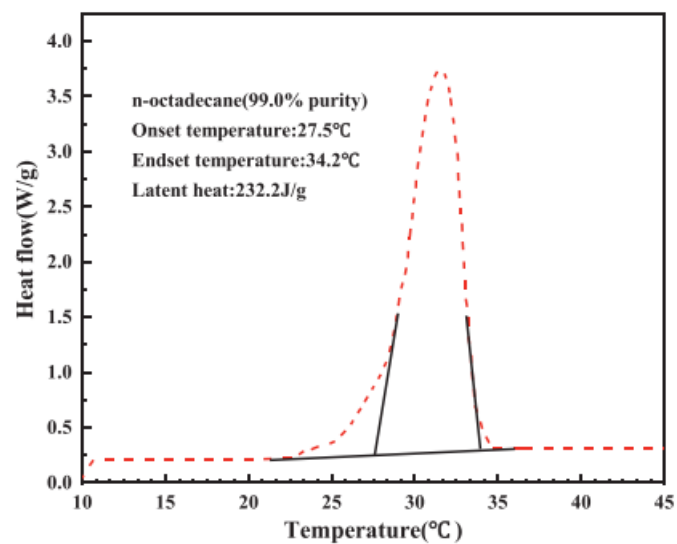


Fig.3.1 A typical DSC graph (DSC curve of n-octadecane).

Methods for detecting other phenomena associated with phase change

As mentioned above, during the phase change process, supercooling may also occur and has a significant effect on thermal storage applications, thus it is necessary to detect this phenomenon. Supercooling is the phenomenon that materials keep their liquid phase even when their temperatures are lower than their freezing point. Thus it is possible to detect supercooling by monitoring the material temperature and whether the material is in liquid phase or not. This also means that the techniques for the detection of phase changes can be used to also detect supercooling. For example, Aubuchon [81] used DSC for the detection of crystallization of supercooled water. In the experiment the heat flow was monitored during the water solidification process, so that occurrence of the peak in the heat flow whilst the temperature of the water was lower than its freezing point, indicating the presence of supercooling. Liu *et al.* studied the degree of supercooling during the formation of ice slurry under different stirring rates, cooling rates and ethylene glycol concentrations [82]. They detected supercooling by direct observation of the phase state of the water-ethylene glycol mixture and recording the temperature simultaneously. The authors used this method to detect supercooling for the ethylene glycol aqueous solution with different concentrations and concluded that higher ethylene glycol concentrations resulted in a narrow supercooled region and higher unpredictability of the formation of ice. Kalke *et al.* reported measurements of supercooling in the North Saskatchewan River [83]. Four locations on the North Saskatchewan River were chosen for the measurements. The supercooling of the river was detected by measuring the temperature of the water at the selected locations over three winters seasons between 2015 and 2018. The temperature measurements were carried out by using RBR Solo T temperature loggers with an accuracy of ± 0.002 °C, which were

housed in metal enclosures and fixed in the river bed. If the temperature was lower than 0 °C while the water is still in liquid phase, the presence of supercooling was confirmed.

Another area which is associated with phase change sensing is the detection of the presence of ice. Ice formation on aircraft surfaces can disrupt the airflow and lead to a loss of aircraft control. This phenomenon occurs when supercooled droplets strike the aircraft surface and begin to solidify forming an ice layer so that the stability of the aircraft is compromised. Zhang *et al.* proposed an ice detection sensor based on the electromechanical impedance method [84]. The sensor is fabricated by using piezoelectric wafer and relies on the change of electric impedance of the piezoelectric wafer caused by ice formation. The sensor has the advantages of high sensitivity to the small changes in local mass, but its spatial resolution is low. Gao *et al.* proposed a method for ice detection based on ultrasonic guided-wave modelling [85]. By using this model, the thickness and type of ice formation can be determined from guided-wave signals. The authors also carried out an experiment to verify the correctness of the model. However, it should be noted that the equipment designed for detecting ice has the disadvantage of a complex setup and low spatial resolution.

3.3 Optical fiber sensors for phase change detection

3.3.1 Existing optical fiber sensing methods for phase change detection

Previously in Chapter 2, a general overview of different optical fiber sensor types was provided. In-line with the theme of this Chapter, this section considers optical

fiber based sensors but now with a specific focus on using fiber sensors for phase change detection in PCMs.

As mentioned in the previous chapter, optical fiber sensors show great potential to be applied in detecting phase change, due to their adaptability to deal with different sensing challenges including situations where the fiber is embedded in a solid material or immersed in a liquid. PCM materials can be in a solid or liquid state and in principle therefore a suitable optical fiber sensor can be used within a PCM for phase change detection.

When phase change of the PCM occurs, the material density also changes, causing a variation in the RI of the PCM, which can be described as [86]

$$n = 1 + k\rho \quad (3.1)$$

where n is the RI of the PCM, k is an empirically determined constant, ρ is the density of the PCM.

To date only a limited number of studies focused on the detection of solid-liquid phase changes involving optical fiber sensors have been reported. Most of them are developed based on the principle that the RI of PCM changes as a result of the phase transition. For example, Millo *et al.* developed a fiber-optic evanescent wave spectroscopic method for the detection of solid-liquid phase changes in water based on the changes of the sample's absorbance [87]. The sensor head was fabricated from a section of a silver halide-based fiber, placed in a special cell whose construction allowed a slow heat transfer to a liquid sample. The authors chose double distilled water and heavy water as samples for the experiment. The absorption spectrum can be divided into regions corresponding to O–H stretch

mode, H–O–H bend mode and frustrated rotation and translation modes. By observing the vibration of the three regions of the spectrum, the phase change can be detected. However, the technique is relatively complex and requires the use of special silver halide-based fibers.

Wahl *et al.* reported a dual-sensor system for monitoring phase transitions in both pure water and an aqueous ethanol mixture based on changes of the RI and temperature, and the strain applied on the sensors during phase change [88]. The sensor was fabricated from an FBG connected in parallel with a singlemode-thin core-singlemode structure fiber sensor. The authors researched the effect of temperature on the output signal, RI and strain during the phase change. Based on the information supplied by these three parameters, the solid and liquid phases can be characterized. Moreover, the sensor was also capable of estimating the concentration of the aqueous ethanol mixture in the remaining liquid during the phase change. The main disadvantage of their method was a relatively low spatial resolution, as the sensor system consisted of two sensor heads, which were not at exactly the same location, potentially resulting in measurement errors. Since the technique involves two sensors, another factor which would cause error is the slightly movement of the sensor heads relative to each other caused by the pressure during the phase change. Thus the measurement accuracy of this sensing technique needs to be improved. Boerkamp *et al.* proposed an intrinsic exposed core optical fiber sensor for studies of the surface crystal growth process [89]. The sensor head was fabricated from a section of 6 cm optical fiber with an exposed core. CaCO_3 was chosen as the material sample for the experiment. To examine the growing crystals, scanning electron microscopy was used to record the images of the fiber surface. The authors recorded the attenuation of the fiber sensor output as a

function of the size of crystals on the fiber surface, and calculated the sensitivity of the sensor to the crystal growth based on heterogeneous crystallization layer height and average crystal contact area on fiber, which is 1.12 dB/ μm and 0.31 dB/ μm^2 . The authors demonstrated experimentally the capability of the sensor to monitor the crystallization process. However, there are two kinds of crystallization processes, heterogeneous crystallization and homogeneous crystallization. The proposed sensor was only sensitive to heterogeneous crystallization processes, not sensitive to homogenous crystallization processes, which limits its usefulness and applications.

3.3.2 Optical fiber sensing techniques for detecting the phenomena associated with phase change

Although the methods based on well-known phase change detection techniques can detect supercooling successfully, they have the disadvantages of low measurement resolution, or rely on visual observation, which limits their applications. Compared to traditional methods, optical fiber sensors have several advantages which have been outlined earlier in this section, making them potentially better methods for the detection of the phenomena associated with phase changes, such as supercooling. Up to now there is a very limited body of research on optical fiber sensors for supercooling detection, but some researchers have started start focusing on this new area. In 2016 Mani *et al.* reported a Fresnel reflection fiber sensor for monitoring of crystallization of a supercooling aqueous solution of NaCl based on changes in the reflectivity of the fiber probe associated with changes in the material RI during the phase transition [60]. The sensor head was fabricated from a section of a single-mode fiber and placed into a NaCl

solution, which was chosen as the material sample. A thermocouple was used to record the temperature of the sample. The RI of the NaCl solution varied following the phase change, which caused changes in the output power of the sensor. On heating, the author observed irregular variations of the output signal as the temperature increased towards the stable eutectic temperature of $-22.4\text{ }^{\circ}\text{C}$, which implied that the NaCl solution was supercooled and the sensor was capable of detecting the supercooling. The main disadvantage of the method was the dependency of the sensor's accuracy on local perturbations, such as air bubbles within the material. Since the sensor relied on the RI change of the sample during phase change, if the air bubbles moved to the sensor head, this would change the signal power and provide unreliable information.

In addition to the research related to the detection of supercooling, several researchers investigated the application of fiber sensors in monitoring of ice formation. Ikeades proposed a fiber sensor for the direct detection of ice formation [90]. The fiber sensor, consisting of a set of seven fibers, was arranged in a linear array equidistantly at a distance of 1 mm and placed in a small hollow wing, which was positioned vertically in an icing tunnel, where the air was cooled generating ice at a zero angle of attack. One of the fibers was used as source fiber, which transmitted the light into the ice, the others were used as signal fibers, receiving scattered and reflected light from the ice as it formed. The power of the scattered and reflected light was influenced by the growth of the ice, and based on this principle, the author realized direct monitoring of ice formation and growth for both glazed ice and rime ice. The sensor was highly susceptible to mechanical disturbances, since the power of the scattered and reflected light was easily influenced by interfering substances such as dust. Prasad *et al.* proposed a fiber

Bragg grating sensor for ice detection [91]. The sensor consisted two FBGs, one of which was placed at the outside of a container filled with water, to measure the temperature only. The second FBG was placed inside the water container, to measure both temperature and strain during the phase change. Before ice formation, the spectrum of the second FBG was only affected by the temperature, while it would be affected by both strain and temperature during ice formation. The authors investigated the influence of both temperature and strain on the wavelength shift of the FBG spectra during ice formation. By separating the influences of strain and temperature, the ice formation can be detected. However, since one of the FBGs was at the outside of the container and the other one was placed inside of it, the value and speed of temperature changes both outside and inside the container were not exactly the same, thus leading to an error in the temperature analysis and decreasing the accuracy of the ice formation detection. Wahl *et al.* presented theoretical predictions for the solid-formation and melting temperatures of ice in four binary water-alcohol mixtures containing methanol, ethanol, 1-propanol and 1-butanol [92]. The authors proposed the procedures for the calculation of melting point, freezing point and heterogeneous based on the nucleation theory. Based on this, the authors successfully achieved ice formation detection using a fiber sensor, which was fabricated by connecting a section of a thin core fiber and FBG in parallel.

3.4 Conclusion

Up to now, the development of fiber optic-based techniques for in-situ detection of solid-liquid and liquid-solid phase transitions in PCMs is still in its early stage of development. In comparison with the well-known traditional methods for phase

change detection, fiber-optic methods offer the capability to detect phase changes in-situ and in real time, which is particularly important in practical energy storage research and applications. Moreover, these techniques utilise sensors that are relatively simple, which makes them very attractive for practical applications. Optical fibers have a relatively low cost, for example, standard SMFs used in telecommunications and NCFs cost approximately €5.00 and €7.00 per meter. More complex hollow core fibers have a higher cost of approximately \$500 per meter. Taking into account that a typical length of the fibers required for sensors fabrication is in the order of millimeters or centimeters, the cost of a fiber sensor probe even with the inclusion of the manufacturing costs is comparable with the cost of a typical electronic sensor (such as thermocouple). However, it should be noted that the costs associated with the overall interrogation of the fiber optic sensors are relatively high (circa \$500 - \$1500) and include the costs of the single-wavelength fiberized laser source and detector.

It should be noted however, that while traditional electronic sensors and associated electronic interrogation and signal processing equipment are at least one order of magnitude cheaper, they are unable to detect phase change if supercooling or hysteresis occurs, or when the thermophysical properties of the PCM are not well known.

The comparison between the optical fiber sensing method and traditional techniques for phase change detection is summarized in Table 3.1.

Table 3.1 Comparison of different techniques for the detection of phase changes

	Suitable for opaque materials	Low cost	Simple structure	Suitable for in-situ detection	High resolution
Direct observation	no	yes	yes	no	no
X-ray tomography	yes	no	no	no	yes
Resistance diagnostics	yes	yes	no	no	no
DSC	yes	no	yes	no	no
Fiber sensing	yes	no	yes	yes	yes

However there are still some difficulties in applying fiber sensing technique to real thermal energy storage and other industrial applications. The current challenge to the application of fiber sensing techniques is that the measurement accuracy with which the phase change point can be determined needs to be improved and in addition, there is a need to maximise the immunity of the sensor to external mechanical disturbances, which can also compromise accuracy. To solve these problems, the research objectives proposed in Chapter 1 were pursued and were achieved in this research.

Chapter 4 Optical Fiber Fresnel Reflection Sensor for Detection of Phase Changes

4.1 Introduction

As mentioned in the previous chapters, PCMs play an important role in practical thermal energy storage applications due to their ability to absorb or release large amounts of energy during melting or solidification. However, most of the non-optical methods for phase change detection are unable to achieve the in-situ measurement, while existing optical fiber sensors have some limitations [60, 87], as discussed in Chapter 1. It is therefore necessary to improve the performance of the fiber sensors for accurate detection of liquid-solid phase changes in practical systems.

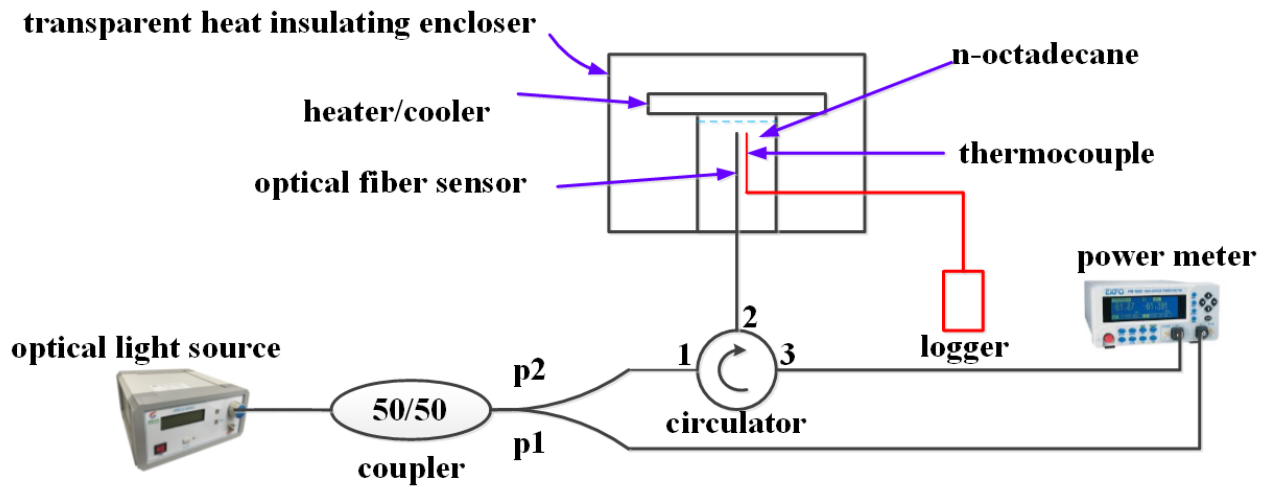
In this chapter a novel method for in-situ detection of the solid-liquid and liquid-solid phase changes in n-octadecane, based on Fresnel reflection fiber sensor probe, is proposed and experimentally demonstrated. The working temperature range of the fiber sensors depends on the melting point of the material used to fabricate them. In this thesis, all the proposed fiber sensors are fabricated from the silica optical fiber. The melting point of silica is 1710 °C, thus all the proposed sensors in this thesis have the potential of working at a temperature higher than 1000 °C. Some popular alkane materials, including the sample (n-octadecane), have phase change temperatures lower than 70 °C, thus the silica fiber sensors have the

potential of detecting phase change for such kind of PCMs. In this work, n-octadecane was chosen for the proof of principle demonstration of the proposed method because the material's crystallization occurs over a narrow range of temperatures, with high degree of repeatability. In addition, the closeness of the freezing point to room temperature allows for a simpler experimental setup. Moreover, the material is transparent in the liquid phase and opaque in the solid phase, which makes it possible to observe the phase change in the vicinity of the probe for comparison and verification purposes.

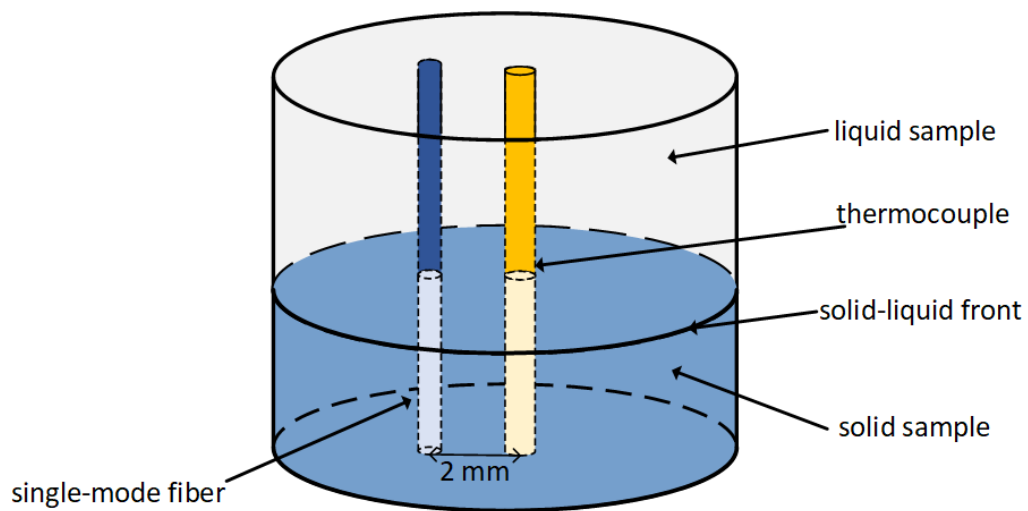
4.2 Experimental setup and operating principle

The experimental setup for the demonstration of the proposed method is shown in Fig. 4.1. The sensing system consists of a 3 dB coupler, whose input port is connected to a broadband source (S5FC1021S, Thorlabs, 1200-1660 nm), one of the outputs of the coupler is connected to one of the channels of the optical power meter (Model 4100, Dbm optics) and another output is connected with Port 1 of the optical circulator. Ports 2 and 3 of the optical circulator are connected to the sensor probe and the second channel of the optical power meter respectively. The sensor probe is fabricated from a standard single-mode fiber with a cleaved end immersed into the sample of n-octadecane. The coating is removed from a small area near the end of the fiber and this area of the fiber is marked with red ink. 25 ml of liquid n-octadecane is used as a sample. Since the density of liquid n-octadecane is 0.777 g/ml, the weight of the sample is 19.4 g. The n-octadecane sample is placed in a transparent glass container with a diameter of 2 cm and a height of 8 cm. Since the liquid sample is transparent while the solid sample is not, visual observation of the red mark indicates that at this point the sample is in the

liquid phase. The sensor is placed inside the material sample to ensure that the sensor is always inside the sample even though the volume of the n-octadecane sample changes before and after the phase change. The temperature in the vicinity of the fiber probe was monitored with a K-type thermocouple with an error of ± 1.1 °C, where T is the actual temperature. The thermocouple was fixed close to the probe. A Peltier element with the rated voltage of 12 V was used as a thermoelectric heater/cooler, with the maximum power of 60 W, placed on the top of the glass cylindrical container, to eliminate the effect of thermal convection. The electric current through the Peltier element is controlled by using a voltage source, with voltage output circa 2 V. From the figure it can be seen that the temperature of the sample measured by the thermocouple is not the exact temperature of the sample at the detection point, but is very close to it and thus can be still used to validate the reliability of the fiber sensor. Moreover, since the heating experiment lasts for approximately two hours and the cooling experiment lasts for approximately four hours, the temperature change of the n-octadecane is very slow and the data were collected when the temperature of the sample is stable, thus the data collection process is considered to be reliable.



a



b

Fig.4.1 (a) Schematic diagram of the experimental setup. (b) 3D image of the sensing area.

To reduce the possible effects caused by any power instabilities of the light source, a ratiometric measurement scheme is used in the experiments [60, 93]. In the experiment, input light from the optical source (with total power $2*(I \pm x)$) travels through the 3-dB splitter, where it is divided equally between 2 outputs of the splitter P1 and P2. Light from P2 (with power $(I \pm x)$) is launched into Port 1 of the

optical circulator and then through its Port 2 is coupled into the fiber probe, immersed into the material sample. The light travels to the end of the fiber probe where it is reflected with reflectivity (R), which can be described using Fresnel equation for normal incidence:

$$R = \left(\frac{n_1 - n_2}{n_1 + n_2} \right)^2 \quad (4.1)$$

where n_1 is the RI of the single-mode fiber core (assumed equal to 1.4494 at the wavelength of 1550 nm) and n_2 is the RI of the material surrounding the sensor.

The light reflected back from the end of the probe is then launched into Port 2 of the optical circulator and then arrives to Channel 1 of the optical power meter.

Light from the output of the splitter P1 ($I \pm x$) is launched into Channel 2 of the optical power meter. The ratio of the optical powers at both channels of the power meter expressed in decibels is calculated using the following expression :

$$R = 10 \lg \frac{R(I \pm x)}{(I \pm x)} = 10 \lg R \quad (4.2)$$

where I is one half of the input power of the optical source (one arm of the 3 dB coupler), x is the power fluctuation of the optical source, R is the reflectivity of the fiber probe

The simulated relationship between the reflected power ratio and the RI of the surrounding material of the sensor probe using equations 4.1 and 4.2 is plotted in Fig. 4.2 (blue line). As one can see from Fig. 4.2, for all n_2 values (the RI of the sample under test) smaller than n_1 (the RI of the fiber core), the reflected power ratio decreases monotonically with the increase of n_2 until the latter becomes equal

to n_1 . For n_2 values greater than n_1 the reflected power ratio increases monotonically with an increase in the surrounding RI (n_2).

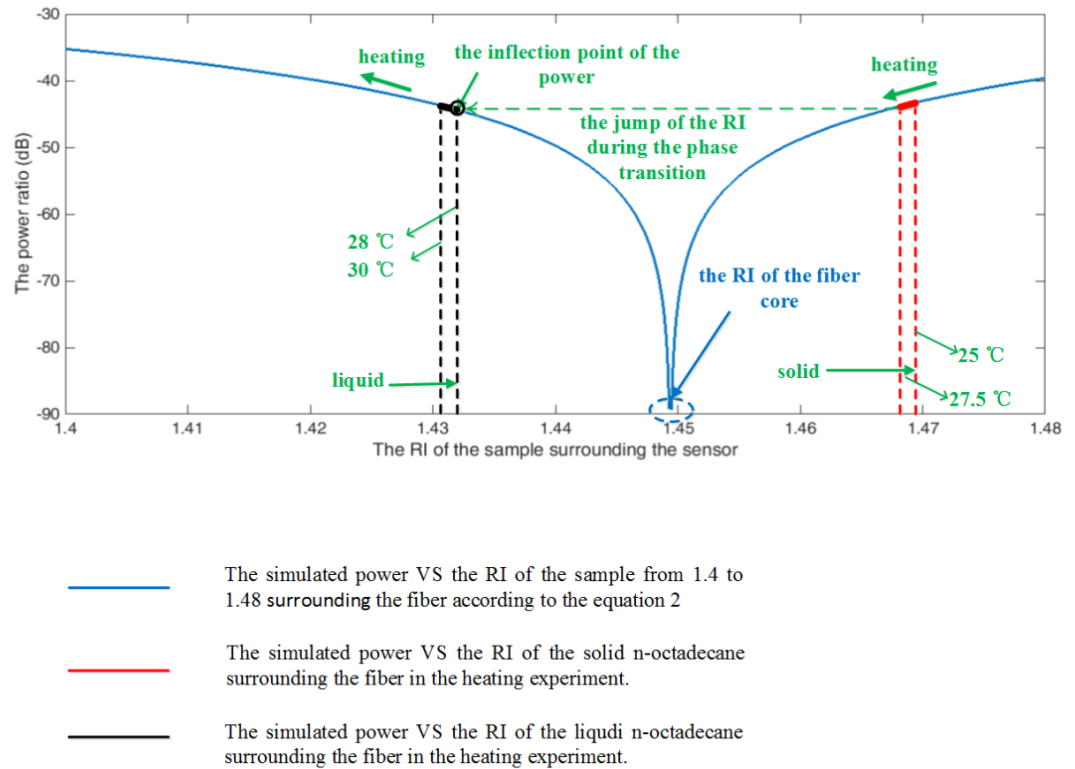


Fig.4.2 Simulated relationship between the reflected power ratio and the refractive index of the surrounding material of the probe.

It should be noted that it is possible to develop an equivalent to Fig. 4.2 for any PCM, based on the behaviour of its RI with temperature and phase changes.

The RI of n-octadecane decreases with an increase in temperature. In its solid phase, the RI experiences a moderate monotonic decrease with temperature, but as soon as the material becomes liquid, its RI decreases sharply from circa 1.468 to 1.432 [94]. Based on these approximate values for the refractive index of n-octadecane and its temperature dependence, the behaviour of the optical power ratio reflected by the probe can be interpreted as follows in accordance with the model presented in Fig. 4.2.

In the experiment, the temperature range chosen for the n-octadecane is from 25 °C to 30 °C, with the phase change occurring at approximately 28 °C. Since the solid n-octadecane has an RI that is larger than that of the fiber core, any increase in temperature results in a decrease of the material's RI and the reflected power ratio ($n_2 \geq 1.4494$, the core refractive index). This is illustrated with the red line in Fig. 4.2, for the temperature increase from 25 °C to 27.5 °C. As soon as the n-octadecane sample melts into liquid, its RI undergoes a discontinuous decrease so it becomes lower than that of the fiber core. From that point, any further increase in temperature causes a decrease in the RI value once more but now because the RI is lower than that of the fiber core, in accordance with Equation 4.2 and the blue trace in Fig. 4.2, the reflected power ratio increases (region $n_2 \leq 1.4494$, the core refractive index), which is illustrated as the black line shown in Fig. 4.2 for a temperature change from 28 °C to 30 °C.

Therefore as the n-octadecane sample goes through the phase change, not only there is a discontinuous jump in the RI as the temperature increases, but there is also a change in the slope of the power ratio versus RI, as confirmed by the different slopes of the red and black lines in Fig. 4.2. Assuming one is observing the reflected power ratio as the temperature increases, there is in effect an inflection point evident in the reflected power ratio with temperature. This inflection point in the reflected power ratio is the key to determining the occurrence of the phase change in the vicinity of the fiber probe. Analogous behaviour is observed during cooling, where the inflection point indicates the liquid-solid phase change.

Finally, it should be noted that the RI values used above for n-octadecane are known to be approximately 1.468 for solid and 1.432 for liquid phases at the

wavelength of 600 nm [94]. Since the experimental setup used here operated at 1550 nm, Cauchy's equation [95] was used to approximate the values of the refractive index of n-octadecane at 1550 nm. The results of the calculations showed that the RI of n-octadecane decreases by 0.1% in its solid phase and by 0.08% in the liquid phase over the wavelength range from 1200 - 1600 nm. Given such small variations, the influence of the wavelength on the RI can be neglected.

4.3 Experimental results and discussion

In order to experimentally demonstrate the operation of the proposed sensor, a series of heating and cooling experiments were carried out for a 19.4 g sample of n-octadecane with a purity of 99% (Sigma Aldrich), using the experimental setup shown in Fig. 4.1. During heating thermal convection can occur, which may result in a movement of fluid from the bottom to the top of the sample. This movement of the liquid could exert a microforce upon the sensor, and also it could result in trapping of air bubbles at the sensing end of the probe, which affects the output power. To eliminate the effects of thermal convection, the Peltier element used for heating and cooling the sample was placed at the top of the container. The fiber probe and the thermocouple were inserted into the container through the bottom of the container, and the distance between the fiber probe and the thermocouple was approximately 2 mm. The thermocouple was connected to a logger for recording the temperature of the n-octadecane in close proximity to the fiber sensor probe. To ensure the stability of the surrounding temperature, the experimental setup was placed inside a transparent heat insulating enclosure. A photo camera was placed inside the transparent enclosure and connected with a PC. The camera shutter was

controlled by a PC. The photo images were taken at the same time as the reflected power ratio and temperature data were recorded with steps of 0.5 °C.

Fig. 4.3 illustrates the dependence of the measured reflected power ratio of the sensor probe versus temperature for the n-octadecane sample during its heating and cooling cycles. The heating experiment was carried by setting the temperature of the Peltier element to 50 °C when the material sample was at room temperature (20 °C). Every data point in Fig. 4.3 is an average of five different heating experiments. The average error is 0.017 dB. The most likely source of error is the system noise itself as the power variation of 0.016 dB was measured when the fiber sensor was immersed into the n-octadecane at a fixed room temperature. The other possible source of error is the changing mechanical forces acting upon the fiber during the phase change, which result from the density change during the phase change of the n-octadecane, leading to slight movement or bending of the probe caused by mechanical stress. It also should be noted that some power variation is observed when the fiber sensor is immersed in the liquid sample both during heating and cooling. The possible source of this power variations is the temperature dependence of the reflectivity of the probe as a result of temperature dependence of the refractive index of the liquid.

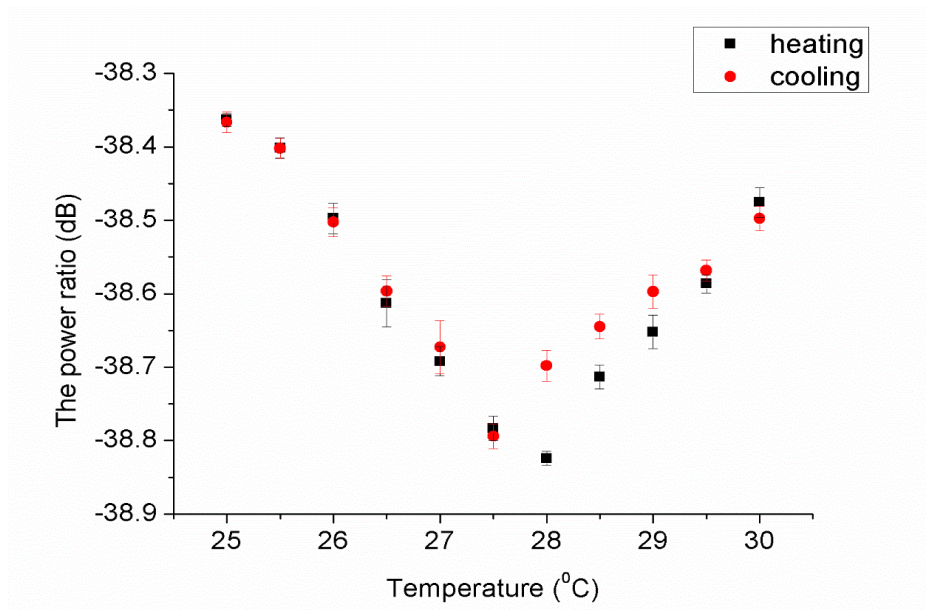
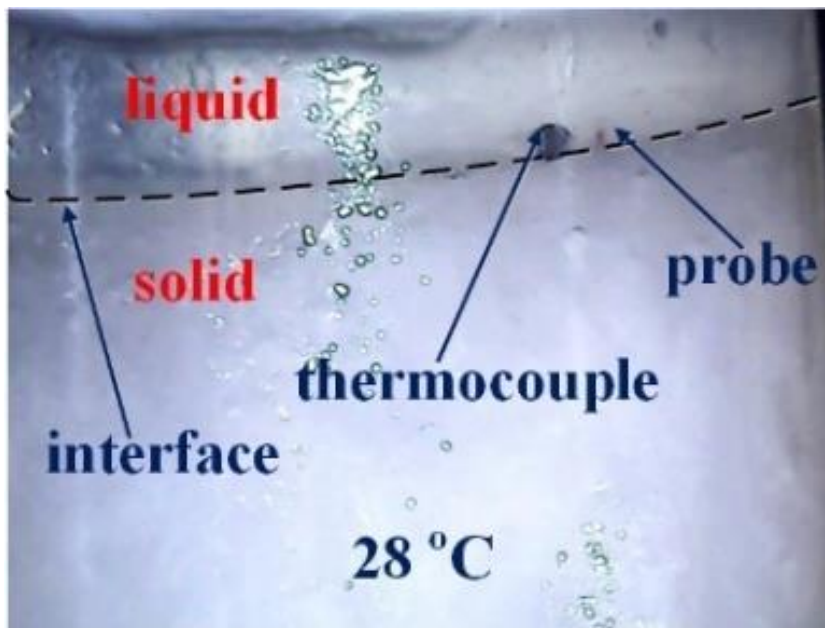
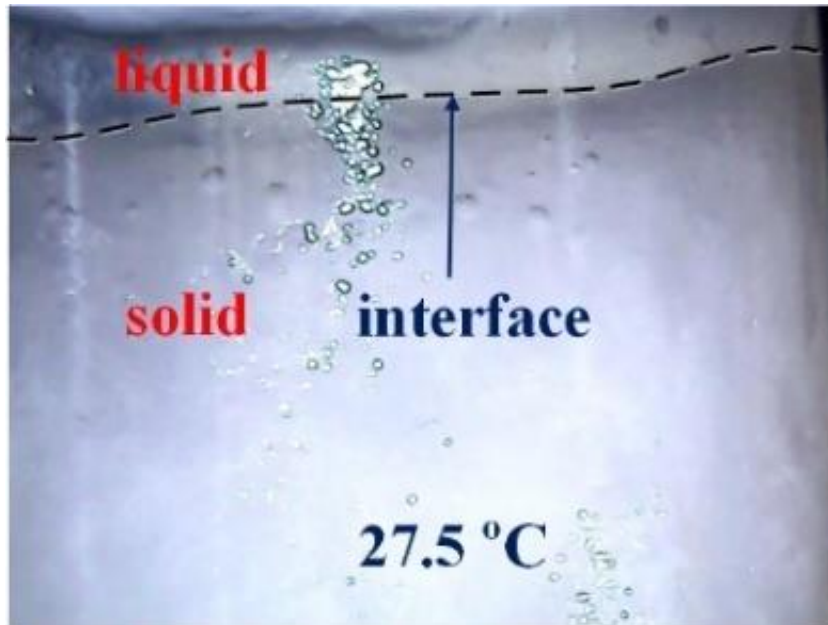


Fig.4.3 Reflected power ratio measured at different temperatures during the heating and cooling cycles of the n-octadecane sample: inflection point at $\sim 28^{\circ}\text{C}$ in the heating experiment corresponds to the solid-liquid phase change and that at $\sim 27.5^{\circ}\text{C}$ corresponds to the liquid-solid phase change on cooling.

As can be seen from the figure, in the heating experiment the reflected power ratio changes from -38.36 dB to -38.78 dB in the range of temperatures from 25°C to 27.5°C , confirming that heating of n-octadecane in the solid phase causes its RI to decrease, resulting in the decrease of the reflected power ratio. Comparison of the experimentally measured reflected power ratio values with the calculated results (shown in Fig. 4.2) leads to the corresponding estimated RI change of solid n-octadecane from 1.4783 to 1.4769 assuming there is no absorption by the n-octadecane. In the vicinity of 28°C n-octadecane becomes liquid, which causes the change in the power ratio dependence as predicted by the proposed physical model. In the temperature range from 28°C to 30°C , the measured reflected power ratio changes from -38.82 dB to -38.48 dB . During the heating in its liquid phase the RI of n-octadecane continues to decrease, but in this case the RI values of n-octadecane become smaller than RI of the silica fiber, resulting in the increase of

the reflected back power ratio as predicted by the simulations in Fig. 4.2, where a change in the power ratio from -38.82 to -38.48 dB corresponds to the change in the liquid RI from 1.4226 to 1.4215.

It should be noted that in the experiment the RI of n-octadecane is slightly different from the value reported in the reference [94] possibly because of the absorption loss in n-octadecane, differences in the material purity and temperature, which could be a result of the finite distance between the thermocouple and the probe. Fig. 4.4 shows images of the n-octadecane sample taken at different temperatures. From Fig. 4.4 it can be seen that during heating, when the temperature of the sample is lower than 28 °C, the fiber sensor is not visible, which proves that it was in the solid sample before melting. However, as soon as temperature reaches 28 °C, the fiber sensor becomes visible, which proves that it is in the liquid sample after melting. The whole process shown in Fig.4.4 is consistent with the heating experiment result. It can be seen, that the point of inflection within the experimental graph corresponds to the solid-to-liquid phase transition of n-octadecane demonstrating that monitoring of the reflected power ratio change in time (or with temperature) and determining the point of inflection of the reflected power ratio dependence allows for an accurate detection of the phase change of the material at the location point of the sensor probe. It should be noted that if the proposed method is used for detecting the phase change, the temperature information is not needed, and the sensor is capable of providing information regarding the phase state at a particular location within a volume of material in real-time, by continuous monitoring of the power ratio of the sensor.



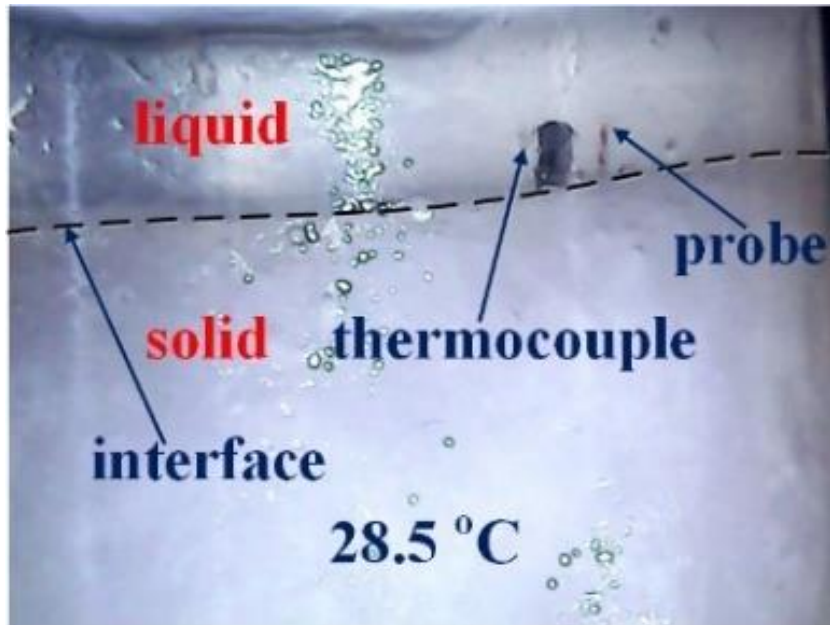


Fig.4.4 Photographs of the solid-liquid interface position at different temperatures: at 28°C both the thermocouple and fiber optic probe tips are clearly visible (the image corresponds to the inflection point in Fig. 4.3).

For the cooling experiment the temperature of the Peltier element was set to 20 °C, while the material sample was in the liquid phase at 30 °C. Cooling of the n-octadecane sample causes an increase in its RI. The reflected power ratio changes from -38.49 dB to -38.79 dB as the temperature decreases from 30 °C to 27.5 °C. In accordance with the simulations, the RI in this temperature interval changes from 1.4216 to 1.4225. At 27 °C the n-octadecane becomes solid which causes the sudden increase in the reflected power ratio up to -38.67 dB, followed by its subsequent increase to -38.37 dB. During the cooling in the solid phase, the RI increases but since the RI of the solid n-octadecane is larger than the RI of the fiber core, the power ratio increases as predicted by the simulation, where a change in the power ratio from -38.67 dB to -38.37 dB corresponds to the change in the solid RI from 1.4772 to 1.4782. The freezing point is lower than the melting point due to the hysteresis phenomenon, which is a thermodynamic phenomenon previously considered in section 1.2.2. The average error is 0.019 dB. The possible source of

the error is the same as that in the heating experiment. As it can be seen from Fig. 4.3, the inflection of the reflected power ratio dependence corresponds to the phase change point for the n-octadecane sample. Fig. 4.5 illustrates the gradual shift of the interface between liquid and solid phases during the cooling experiment. From Fig. 4.5 it can be seen that during cooling, when the temperature of the sample is higher than 27 °C, the fiber sensor is visible, which proves that the sensor is in the liquid sample before solidification. However when the temperature reaches 27 °C, the sensor becomes invisible, which proves that it is in the solid sample after solidification. The solidification process shown in Fig.4.5 is consistent with the cooling experiment result. It can be seen that during cooling the point of inflection within the experimental graph corresponds to the image where the solid-liquid interface reaches the fiber probe, confirming the phase change at the location of the probe.

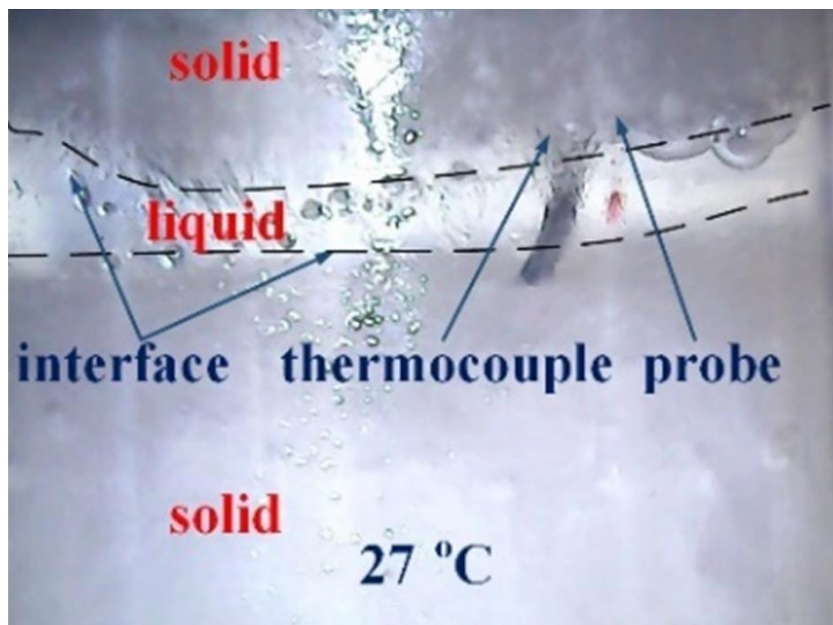


Fig.4.5 Photographs of the solid-liquid interface position at different temperatures: at 27.5°C both the thermocouple and fiber optic probe tips are in contact with the solid surface (the image corresponds to the inflection point in Fig. 4.3).

Moreover, one can determine whether the n-octadecane is in the solid or liquid phase from the slope of the power ratio (ΔP) as shown in Table 4.1. During the heating process, if the slope is negative, then the sample is solid, while if the slope is positive, the sample is liquid. During the cooling process, if the slope is positive, the sample is solid, if the slope is negative, the sample is liquid. The sensor can thus detect the phase change at a certain point within the sample by comparing two consecutive reflected power ratio measurements during the material heating or cooling cycles.

It should be stressed that the aim of the above experiments was not to determine the phase change temperatures (melting or solidification points) of the n-octadecane sample, but its actual phase state in the vicinity of the fiber sensor. Both, melting and solidification points of the sample may vary depending on the chemical purity of the material and even on the rate of heating or cooling. Thus the accuracy of the phase change detection in the above experiments was verified by visual observations of the real phase state in the vicinity of the sensor.

Nevertheless, it is also useful to estimate the accuracy of detection of the material's temperature, which is a parameter indirectly measured by the sensor. Given that the accuracy of the power meter is ± 0.005 dB, and the experimental slope of the power ratio – temperature dependence during heating cycle is circa 0.18 dB/ $^{\circ}\text{C}$, the accuracy of temperature measurement is $\pm 0.02^{\circ}\text{C}$.

Table 4.1. The relationship between the material's phase and the slope of the power ratio.

	Solid phase	Liquid phase

Heating	$\Delta P < 0$	$\Delta P > 0$
Cooling	$\Delta P > 0$	$\Delta P < 0$

Besides, if supercooling occurs, the temperature will be lower than the solidification temperature measured by the thermocouple, and the phase of the sample will be detected as liquid phase by the sensor, so that supercooling can be detected.

From the results of heating and cooling experiments it can be seen that this sensor represents a novel direct phase change measuring method. It should be noted that its main disadvantages are the need for more than one measurement to realize the phase change detection, and relatively high susceptibility to disturbances within the sample under test. The advantages and disadvantages of this sensor are summarized in Table 4.2.

Table 4.2. The novelty, advantages and disadvantages of the Fresnel fiber sensor.

Novelty/advantages	<ol style="list-style-type: none"> 1. A new method (optical fiber sensing) of phase change in-situ detection for n-octadecane 2. High spatial resolution
Disadvantages	<ol style="list-style-type: none"> 1. Need for continuous monitoring (sampling) of the output power 2. High susceptibility to irregularities and disturbances within the material sample

4.4 Conclusion

In conclusion, in this chapter a method for in-situ detection of the solid-liquid and liquid-solid phase changes in n-octadecane, based on Fresnel reflection in a fiber

sensor probe has been proposed and demonstrated experimentally. From the experimental results it can be seen that the melting point is approximately at 28 °C and the freezing point is at 27.5 °C. The accuracy of the phase change detection was confirmed by visual means. The proposed method, which relies on continuous monitoring of the power ratio of the sensor, allows for a simple, accurate and reliable in-situ detection of liquid-solid and solid-liquid phase changes in n-octadecane without the need for temperature measurements. Moreover, at the same time supercooling of PCMs can be detected which is a critical issue for optimization of and control of latent heat thermal energy storage technologies. This point-sensing technique can be expanded by increasing the number of sensor probes and applied to studies and optimization of heat distribution within the PCM material employed in energy storage systems. The results of this work suggest that such a simple optical fiber Fresnel reflection sensor can be used for the detection of liquid-solid phase changes in other materials with thermo-optic properties similar to those of n-octadecane.

Chapter 5 A Fiber Heterostructure based Optical Fiber Sensor for Detection of Phase Changes

5.1 Introduction

In the previous chapter a Fresnel-reflection based fiber sensor for phase change detection in n-octadecane was proposed. It had the advantage of a simple structure and can provide accurate and reliable phase change detection in-situ without the need for temperature measurements. However it also had some shortcomings such as the need for continuous monitoring (sampling) of the output power and high susceptibility to the irregularities and disturbances within the material sample, including impurities and air bubbles, making it less reliable in real world applications.

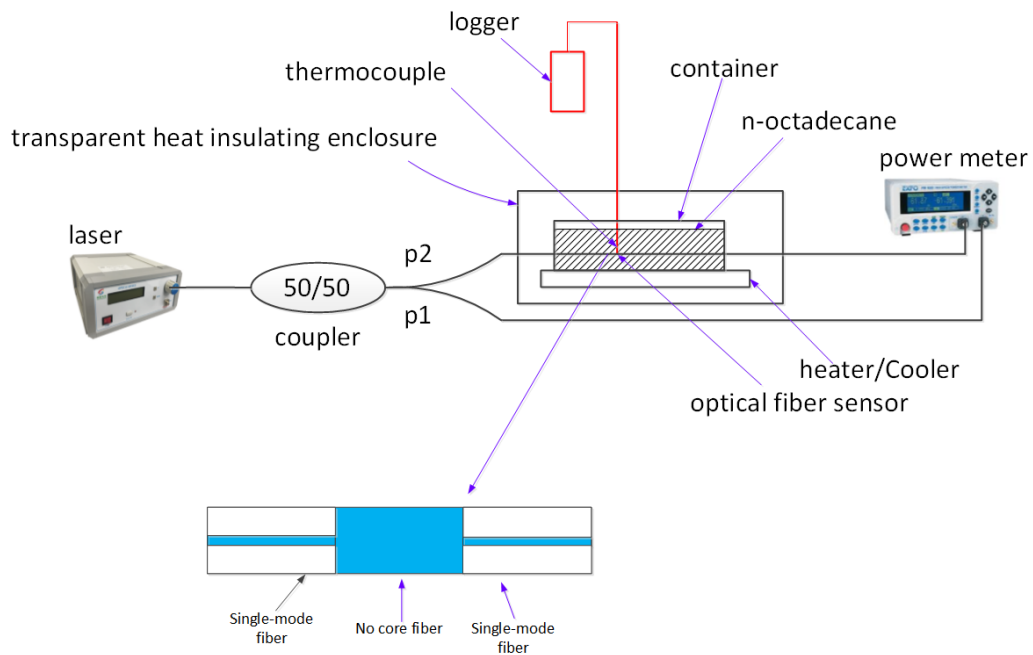
To overcome the shortcomings of the Fresnel fiber probe, in this chapter an alternative fiber optic sensor for in-situ detection of the solid-liquid and liquid-solid phase changes in n-octadecane is proposed and experimentally demonstrated. The sensor probe proposed in this chapter utilizes a so-called fiber heterostructure fabricated from two distinct fiber types by splicing a short section of a NCF between two sections of standard SMFs to form a single-mode-no core-single-mode (SNS) fiber sensor. Similar to the singlemode-multimode-singlemode fiber sensor (SMS) introduced earlier, the proposed SNS sensor operates based on the multimode interference phenomenon. . A conventional SMS structure which uses a standard multimode fiber as the center section is largely impervious to changes

in the surrounding RI, because of the presence of a cladding surrounding the core. Clearly in this application sensitivity to the surrounding RI is necessary, hence an NCF is used as the center section of the SMS structure as it has a much higher sensitivity to the RI of the external environment [96]. In addition to the advantages offered by the Fresnel fiber probe, the SNS sensor proposed in this chapter allows to determine the specific phase state based on a single measurement of the output sensor power after an appropriate calibration. Moreover, using the method proposed here the influence of small fluctuations of the output power due to the presence of air bubbles, voids and impurities can be eliminated, which makes the proposed sensor a lot more reliable in practice.

5.2 Experimental setup and operating principle of the sensor

The proposed sensor system is shown in Fig. 5.1. To eliminate the effect of power fluctuations in the output of the optical source over time, a ratiometric scheme has been used that determines the ratio between the output power from the sensor and that from a reference arm [97]. The system consists of a 3 dB fiber coupler, the input port of which is connected to a laser (NETTEST, wavelength: 1550 nm), one of the outputs of the coupler is connected to one of the channels of the two-channel optical power meter (Model 4100, Dbm Optics) as a reference and another output is connected to the fiber sensor. The output fiber of the sensor is connected to the second channel of the optical power meter. The sensor probe which is immersed into a sample of n-octadecane is fabricated from a short section of a NCF spliced between two sections of standard SMF. The coating is stripped from the NCF section and the SMF near the NCF section is marked with blue ink to allow for

better observation of the probe's position when it is immersed in the material sample. By stripping the coating from the NCF, light in the NCF can interact with the PCM sample and potentially allow for the output power of the SNS to be modified by the RI change of the sample. In addition since n-octadecane is transparent in its liquid phase and is opaque in the solid phase, the visibility of the blue mark may be used as the means of verification that the sample is in liquid phase. The temperature in the vicinity of the fiber sensor probe is monitored with a K-type thermocouple fixed near the probe (~2 mm). The thermocouple has an error of ± 1.1 °C, where T is the actual temperature. A Peltier element with the rated voltage of 12 V was used as a thermoelectric heater/cooler, with the maximum power of 60 W.



a

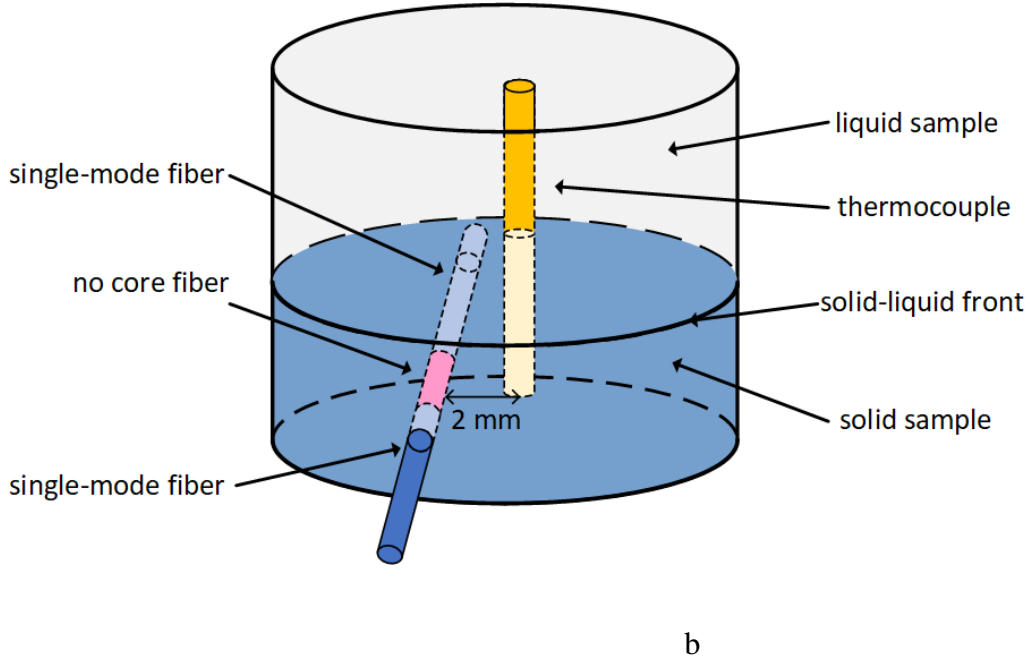


Fig.5.1 (a) Schematic diagram of the experimental setup. (b) 3D image of the sensing area

From the figure it can be seen that the temperature of the sample measured by the thermocouple is not the exact temperature of the sample at the detection point, but is very close to it and thus can be still used to validate the reliability of the fiber sensor. Moreover, since the heating experiment lasts for approximately two hours and the cooling experiment lasts for approximately four hours, the temperature change of the n-octadecane is very slow and the data were collected when the temperature of the sample is stable, thus the data collection process is considered to be reliable.

Assuming the input and output SMF sections are identical and L is the length of the NCF, when the sensor is immersed in the solid sample, whose RI is higher than that of the NCF, the optical field in the NCF consists of leaky modes and the output of the sensor can be described as [98]:

$$P = 10 \log_{10} \left(\frac{|\int_0^\infty E(L)E_0 ds|^2}{\int_0^\infty |E(L)|^2 ds \int_0^\infty |E_0|^2 ds} \right) \quad (5.1)$$

where $E(L)$ is the electrical field at the end of the NCF section and E_0 is the electrical field amplitude of the fundamental mode within the SMF. The electrical field of the leaky modes in the NCF can be described as [98]

$$E(L) = \sum_{m=1}^M b_m E_m e^{i\beta_m L} e^{-a_m L} \quad (5.2)$$

where E_m and b_m are electrical field and excitation coefficients of the m^{th} leaky mode in the NCF respectively, β_m and a_m are the propagation and attenuation constants respectively and M is the total number of modes in the NCF.

When the sensor is immersed in the liquid sample whose RI is lower than that of the NCF, the field of the NCF consists of guided modes which can be described as [99]:

$$E(L) = \sum_{m=1}^M b'_m E'_m e^{j\beta'_m L} \quad (5.3)$$

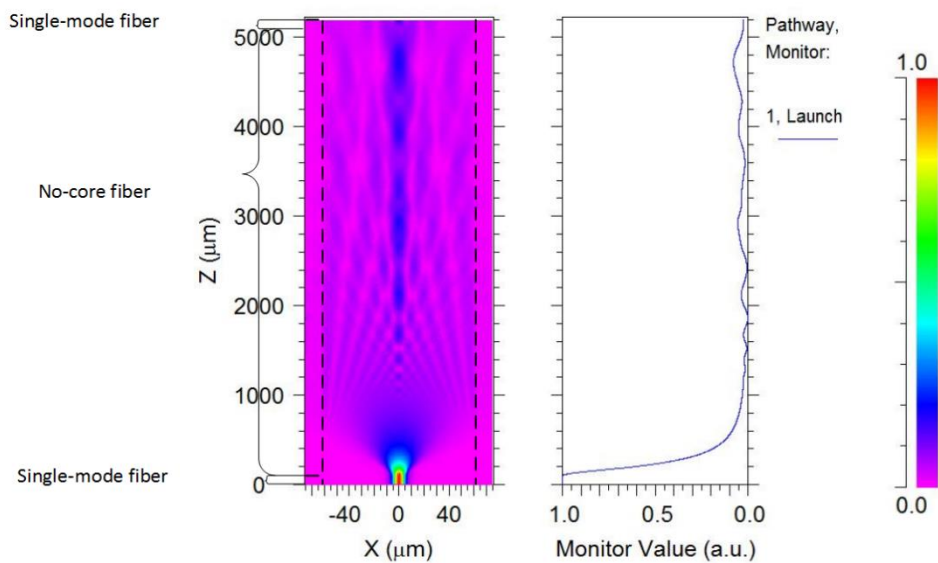
where b'_m is the excitation coefficient of each mode, E'_m are the eigenmodes of the NCF and β'_m are the propagation constants of each eigenmode of the NCF. The electrical field of the leaky modes and eigenmodes can be calculated by using equation 2.3.

According to the data presented in the previous chapter, the RI values for n-octadecane are approximately 1.468 in the solid and 1.432 in the liquid phases at a wavelength of 600 nm. These values decrease only by 0.08% for the solid and by 0.07% for the liquid phase at a wavelength of 1550 nm [95]. Also, the RI of n-octadecane decreases with temperature. While in the solid phase it experiences only a small decrease, as soon as n-octadecane becomes liquid, its RI decreases sharply with temperature from circa 1.468 to 1.432. The RI of the NCF is 1.444, which is lower than that of solid n-octadecane, therefore when the sensor is

surrounded by the solid n-octadecane, light propagating through the no-core section is no longer confined to the fiber due to the absence of total internal reflection at the glass/PCM interface, which results in low power output from the sensor. As soon as the n-octadecane melts into liquid, the RI of the sample decreases to approximately 1.432, becoming lower than the RI of the NCF. The modes with the incident angle larger than the critical angle will be totally reflected so the output power increases sharply. Therefore the phase state of the n-octadecane sample can be determined by measurement of the transmitted power level (“low” power corresponds to solid and “high” power corresponds to liquid phases), and the phase change can thus be determined by detecting the step-like change in the sensor’s output.

Fig. 5.2 illustrates the simulated optical power distribution within the NCF section and the transmitted output powers for the sensor immersed in the n-octadecane before and after melting. The optical power distribution is calculated by solving Helmholtz equations (Section 2.1). The Z axis is the direction of light propagation, and the X axis is transverse to the light propagation direction. The monitored values show the changes of light intensity along the Z axis. The simulations have been carried out using the commercial software package BeamPROP (Rsoft, Pasadena, CA, USA). In the simulations the free space wavelength was set as 1550 nm, the RI of the single-mode fiber core and cladding were set as 1.468 and 1.44 respectively, and the RI of the NCF was set to 1.444. The lengths of the two sections of the single-mode fibers spliced with the NCF were set to 1 mm and the length of the NCF was set as 5 mm, which is the same as the length used in the experiments. The reason for choosing such a short length is to ensure a good spatial resolution for the measurements in the PCM. The diameters of the core and

cladding of the single-mode fiber are taken as $8.3\ \mu\text{m}$ and $125\ \mu\text{m}$, the diameter of the NCF was set as $125\ \mu\text{m}$. In the simulations the RI of the solid n-octadecane was assumed equal to 1.468 and the liquid n-octadecane RI was set as 1.432. From the simulation it can be seen, that when the material sample is solid (Fig. 5.2a), the light power launched from the first single-mode fiber section into the NCF ($Z=100\ \mu\text{m}$) is coupled out of the NCF into the solid sample whose RI is higher than that of the NCF, causing the low power output of the sensor. As soon as the sample melts into a liquid (Fig. 5.2b), the RI of the material sample becomes smaller than that of the NCF, so that the light power is more strongly confined within the NCF section leading to a higher power coupled back into the second single-mode fiber and thus to the higher output of the sensor.



a

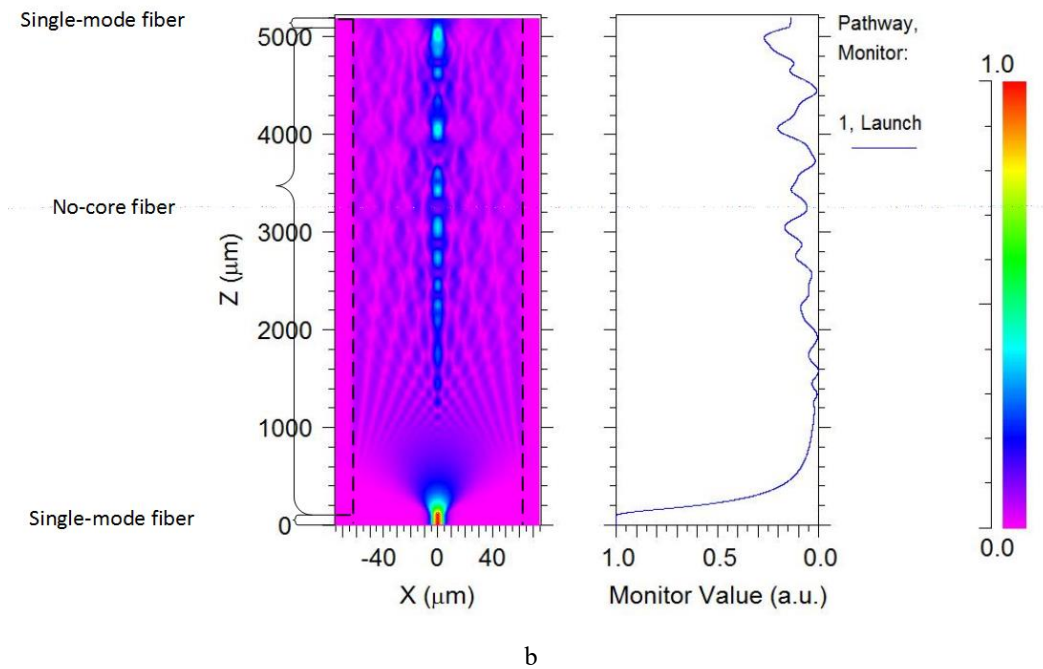


Fig.5.2 Simulated output power distributions (left) and light intensity along the Z axis (right) when the sensor is immersed in: (a) solid, (b) liquid n-octadecane.

5.3 Experimental results and discussion

Prior to the experiments with n-octadecane, the sensor's spectral response was initially characterized in the air by simply connecting its input to the broadband optical source and its output to the optical spectrum analyzer. The experimental transmission spectrum of the sensor in air is shown in Fig. 5.3. From the figure it can be seen that the output power varies with wavelength, but the difference is less than 4.5 dB over a wide spectral range from 1520 nm to 1600 nm. In the experiments the laser wavelength was set at 1550 nm.

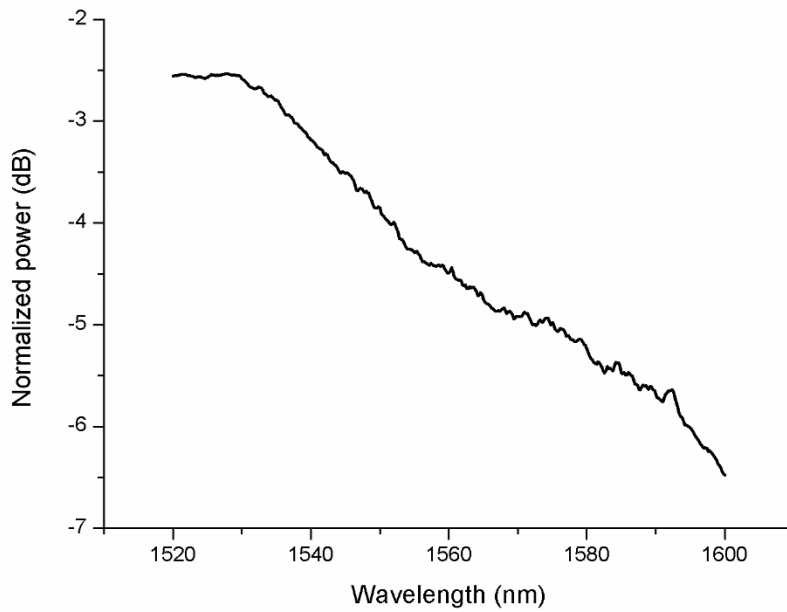


Fig.5.3 Experimental transmission spectrum of the sensor.

5.3.1 Experimental preparation and setup

In order to experimentally demonstrate the operation of the proposed sensor, a series of heating and cooling experiments were carried out for a 19.4 g sample of n-octadecane with 99 % purity (Sigma Aldrich), using the experimental setup shown in Fig. 5.1. The fiber probe and the thermocouple are immersed into the n-octadecane sample with the distance between the fiber probe and the thermocouple set at approximately 2 mm. The sensor is placed inside the material sample to ensure that the sensor is always inside the sample even though the volume of the n-octadecane sample changes before and after the phase change.

The thermocouple was connected to a logger to record the temperature of the n-octadecane close to the fiber probe. A digital camera was also placed inside the enclosure and connected with a laptop for recording images. The camera shutter was controlled by a PC. The photo images were taken at the same time as the

output power of the sensor and temperature data were recorded with steps of 0.5 °C. For the heating experiment the hot side of the Peltier element was set to the temperature of 50 °C, causing the heat to propagate slowly upward through the sample and resulting in its progressive melting, so that the interface between the solid and liquid phases could be seen moving up through the sample and recorded by the camera.

During the cooling experiment the Peltier's current direction was reversed so that its surface at a temperature of 15 °C was in contact with the sample, causing solidification of the sample which propagated slowly upward through the sample and again produced a visible interface between the liquid and solid phases that was recorded by the camera.

To ensure the stability of the surrounding temperature, the experimental setup was placed inside a transparent heat insulating enclosure. During the heating experiment the surrounding temperature inside the enclosure was 20 °C, well below the temperature range of interest near the phase change point (circa 27.5 °C). Prior to conducting the experiments, the sample and the Peltier element were kept within the enclosure for a period of time to reach the starting temperature of 20 °C. The enclosure was used in order to eliminate any sporadic phase changes in the sample due to the surrounding environment and to ensure that the only heat source that could cause a phase change was the heater. In turn this resulted in a well-defined interface between the solid and liquid n-octadecane that was easily and repeatably observable by the camera. In the case of cooling a well-defined sharp interface between the solid and liquid n-octadecane was ensured by setting the temperature within the enclosure to 30 °C and thus the sample's overall temperature was also 30 °C.

Prior to the cooling experiment, in order to ensure a well-defined sharp interface between the solid and liquid n-octadecane, the temperature of the heater was first set to 30 °C for a period of time sufficient for the sample's overall temperature to reach 30 °C. Then the Peltier heater's current direction was reversed so that the cold side of the heater, set at the temperature of 15 °C, was in contact with the sample, causing its slow solidification up from the bottom of the cuvette and producing a sharp and clearly visible interface between the liquid and solid phases that was recorded by the camera.

5.3.2 Experimental results

Based on the data returned by the sensor and the thermocouple, Fig. 5.4 illustrates the dependence of the output power ratio which is the ratio of the powers of the sensor probe and the light source, versus the temperature of n-octadecane during its heating and cooling cycles.

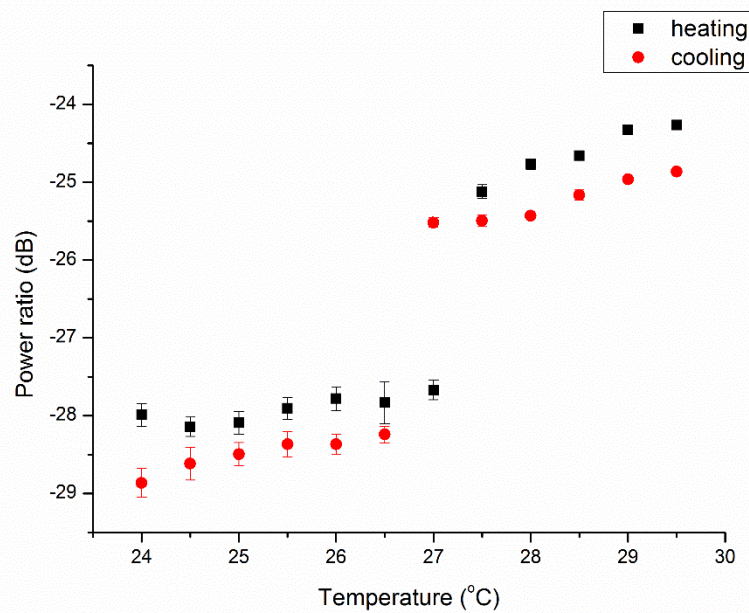


Fig.5.4 Experimentally measured normalized output power during heating and cooling cycles.

Each data point in Fig. 5.4 is an average of five different heating (or cooling) experiments. The average error of the data when the sensor is surrounded by the solid phase is 0.158 dB, while the average error of the data when the sensor is immersed liquid is 0.042 dB. The difference in errors between the phases is likely due to the sensitivity of the fiber probe to strain and bending. The strain and stress forces acting upon the fiber sensor in the solid phase are greater in comparison with those in the liquid state as a result of the higher material density of solid n-octadecane [97]. Moreover, restricted mobility of the fiber probe in the solid phase may result in random variations of the stress/strain upon the sensor due to the micro-bending of the fiber.

As can be seen from the graph, the results for the cooling and heating cycles differ slightly in terms of the average power levels in both liquid and solid phases. This also could be attributed to the influence of stain and bending on the probe. Since in each of the experiments the directions of movement of the solid phase front are different, this leads to the difference in bending forces and resulting curvature of the probe.

Fig. 5.4 shows that for the heating experiment, in the range of temperatures from 24 °C to 27 °C the normalized transmitted power experiences minor fluctuations ranging from -27.99 dB to -27.67 dB. Since the RI of the solid n-octadecane is approximately 1.47, which is higher than the RI of the NCF, the output power is low. As soon as the temperature of n-octadecane reaches 27.5 °C the sample melts into a liquid and its RI decreases to approximately 1.42, which is lower than the RI of the NCF. Thus the light rays with an incident angle larger than the critical angle experience total internal reflection, which causes a sudden increase in the transmitted power. The critical angle can be described as [56]:

$$\theta_c = \arcsin \frac{n_2}{n_1} \quad (5.4)$$

where n_1 in this case is the RI of the NCF and n_2 is the RIs of the liquid n-octadecane. As the temperature increases further, the RI of the n-octadecane decreases, leading to the decrease of the critical angle, so that a greater proportion of the optical power is confined to the NCF, causing a slight increase in the output power with the temperature of the liquid. It should be noted that when the sensor is immersed in liquid during heating, a small variation on the power ratio is observed. One possible source of this power variation is the micromechanical forces caused by the thermal convection, leading to a slight bending of the sensor. The recorded images show that the step-like change in the sensor output aligns very well with the visible phase change recorded by the camera. Fig. 5.5 shows images of the n-octadecane sample taken at different temperatures during the heating experiment. From the photos it can be seen that at 27 °C the sensor is not visible, which means the sample surrounding the sensor is solid, while at 27.5 °C the fiber sensor is visible, which proves that above 27.5 °C the sample surrounding the sensor is in the liquid phase.

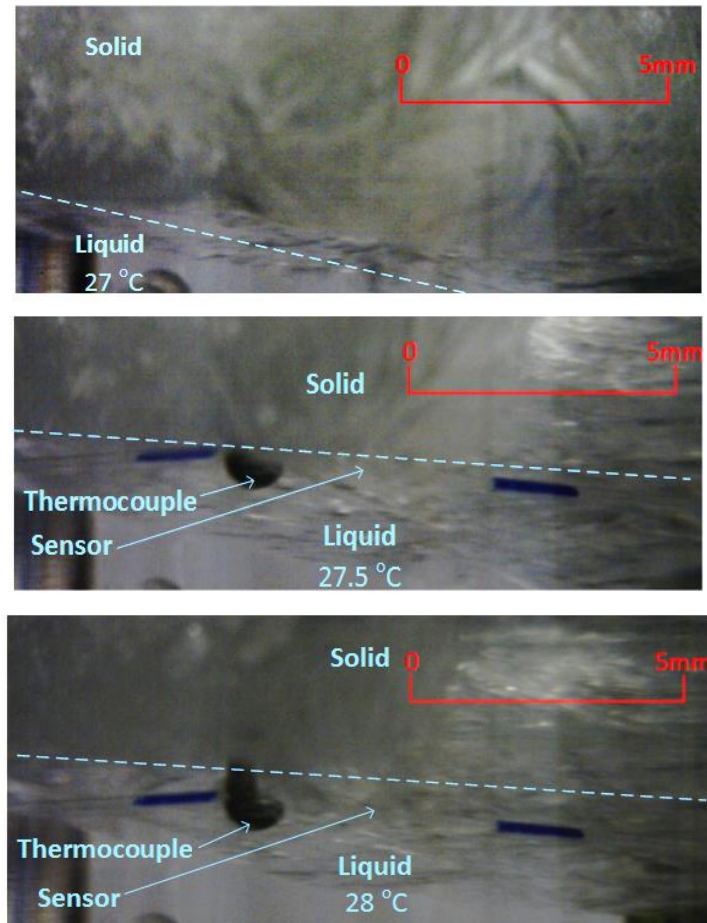


Fig.5.5 Photographs of the sample at different temperatures during heating experiment.

Fig. 5.4 also illustrates the behaviour of the measured normalized output power of the sensor probe versus the temperature of n-octadecane during a number of cooling cycles. The average error of the data when the sensor is inside the solid phase is 0.155 dB, the average error of the data when the sensor is immersed in liquid is 0.043 dB. Similarly to the heating case, the average error is higher when the sensor is inside the solid sample. From Fig. 5.4 it can be seen that the experimental results are in a good agreement with the simulations.

As the liquid sample is cooled from 29.5 °C to 27 °C, the probe's output power decreases slightly by about 0.7 dB, which is consistent with a temperature-induced increase of the material's RI in the liquid phase. It should be noted that there is also a slight variation of the power ratio when sensor is in liquid sample, and the

possible source of the error is similar to that during heating. When the temperature decreases to 26.5 °C the n-octadecane sample solidifies. The output power decreases rapidly from -25.52 dB to -28.24 dB as there is no total reflection for light rays in the NCF section. Fig. 5.6 illustrates images of the n-octadecane sample taken at different temperatures during cooling. From the photos it can be seen that at 27.5 °C and 27 °C the sensor is still visible, which means the sample surrounding the sensor is liquid, while at 26.5 °C the fiber sensor is no longer visible, which proves that from 26.5 °C the sample phase surrounding the sensor is solid.

The phase change temperature measured during cooling experiments (27 °C) is lower than that recorded during heating experiments (27.5 °C) which is in a good agreement with the data reported in [77].

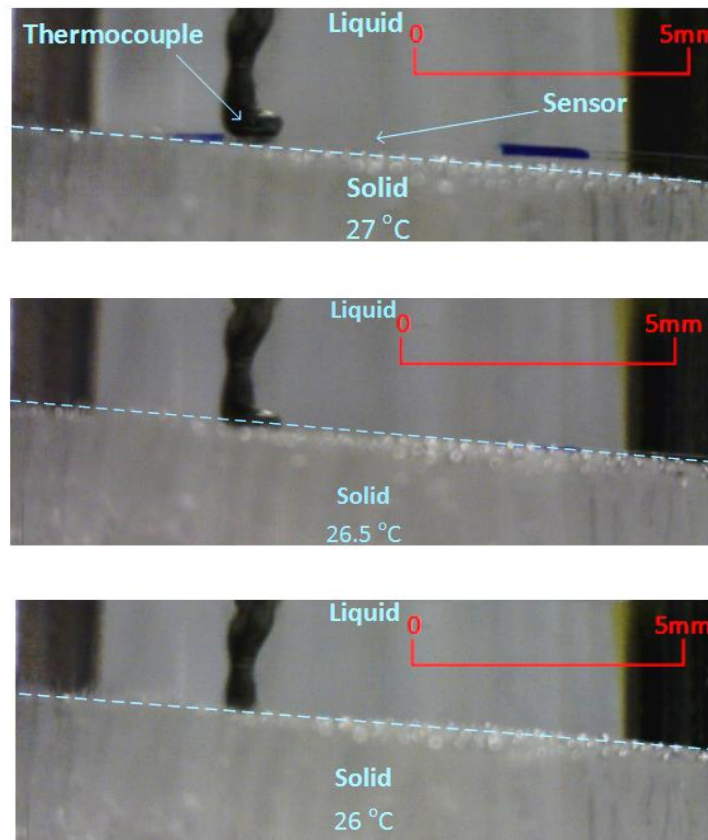


Fig.5.6 Photographs of the phase front at different temperatures during cooling.

From the above experiments it can be seen that due to the sharp changes of the RI of the sample associated with solid-liquid or liquid-solid phase transitions, the output power level from the sensor probe can be used as a measure or an indicator of the material's phase: the sensor output power is low when the n-octadecane sample is solid and is high if the n-octadecane sample is liquid. Therefore the specific phase can be detected by a single measurement, which is an improvement compared to the sensor proposed in Chapter 4, since that sensor needs at least two distinct output power measurements to detect the phase of the sample.

5.3.3 The use of signal processing to improve phase change detection

Signal processing can be used to improve the reliability of phase change detection. The first step in signal processing is to digitize the outputs from the sensor fiber and the reference fiber following optoelectronic conversion. Subsequently software based averaging and noise reduction using low pass filtering or more sophisticated signal processing can be carried out to improve the effective signal-to-noise ratio. Finally the sensor output power level is compared to a reference power level with the reference optical power level chosen as an intermediate output power value equidistant from the lowest and highest possible outputs from the sensor, recorded during the heating/cooling cycles. The result from the comparison will indicate either solid or liquid phases. The input from the reference fiber can be used to fine-tune the reference level used, so as to eliminate the effect of optical source power variations. It should be stressed that the aim of the above experiments was not to determine the phase change temperatures (melting or solidification points) of the n-octadecane sample, but its actual phase state in the

vicinity of the fiber sensor. Both, melting and solidification points of the sample may vary depending on the chemical purity of the material and even on the rate of heating or cooling. Thus the accuracy of the phase change detection in the above experiments was verified by visual observations of the real phase state in the vicinity of the sensor.

Nevertheless, it is also useful to estimate the accuracy of detection of the material's temperature, which is a parameter indirectly measured by the sensor. Given that the accuracy of the power meter is ± 0.005 dB, and when phase change occurs, the temperature changes 0.5 °C while the power ratio changes approximately 2.72 dB, thus temperature dependence is circa 5.44 dB/°C, the accuracy of temperature measurement is ± 0.0009 °C.

5.3.4 Experimental results for slow natural cooling

To study the sensor's ability to operate in the conditions where temperature and thermal convection changes are less controlled and less predictable, another cooling experiment was carried out, during which the temperature inside the enclosure was set to 15 °C and liquid n-octadecane was left to cool naturally. The initial temperature of the n-octadecane sample was 30 °C. Unlike cooling from the bottom of the container in the former experiment, in this case cooling of the sample occurs from its outer walls towards the center of the sample, so that the increasing pressure (due to the increasing sample density) is applied to the fiber from all directions. In such conditions there is no visible solid-liquid interface and the phase change is likely to be affected by various random factors. This in turn may result in larger fluctuations of the sensor output. The purpose of this experiment was to evaluate the performance of the sensor in such conditions, and the results are

illustrated in Fig. 5.7, where each point is an average of five measurements. As it can be seen from the figure, in the temperature range from 24 °C to 26.5 °C, the power ratios are in the range from -28.84 dB to -28.47 dB, which means that the sensor's output is low and the n-octadecane is in its solid state in the vicinity of the sensor. In the temperature range from 27 °C to 29 °C the output power ratios in the range from -25.22 dB to -24.56 dB. The output power is high indicating that the sensor is immersed in liquid n-octadecane.

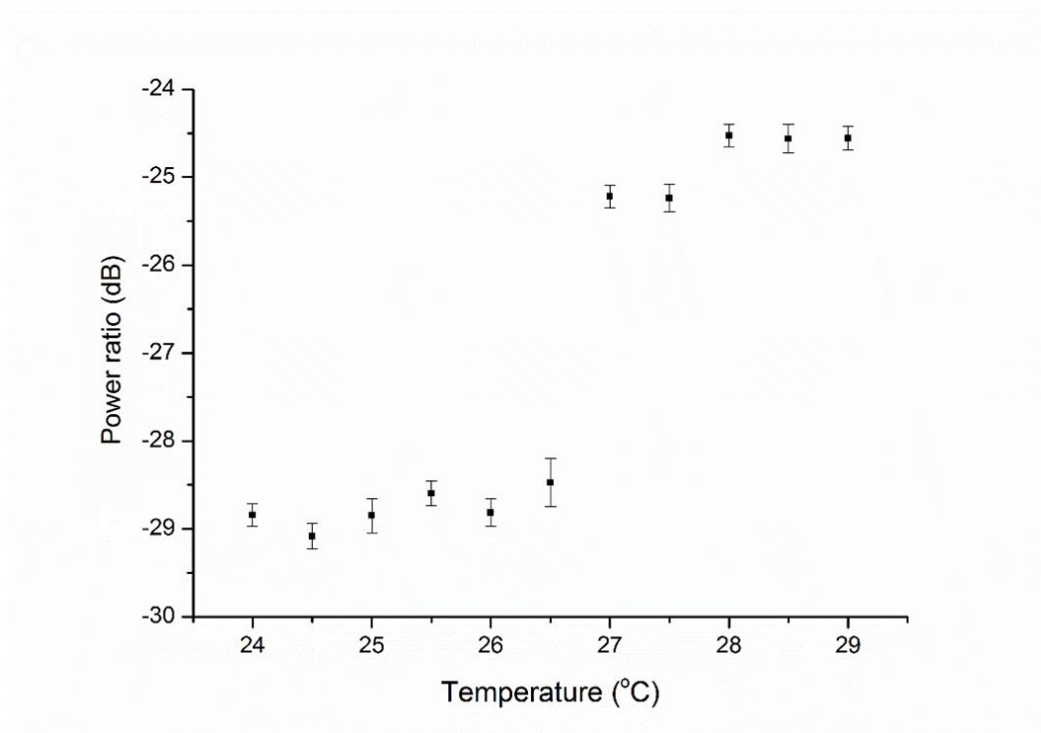


Fig.5.7 The result of the cooling naturally experiment.

Every data point in Fig. 5.7 is an average of five different cooling experiments. The average error of the whole experimental result is 0.16 dB. Compared to the previous experiment (Fig.5.4), the average error is larger and there is even a small decrease in the power output when the sample is in its liquid phase, which did not occur previously (Fig.5.4). One possible explanation is that in the latter experiment,

the changes in the values and direction of the bending and strain applied to the fiber immersed in the sample were random during the entire process. However, even though the bending and the strain change randomly, it can be seen from Fig.5.7 that the information provided by the sensor allows for the unambiguous detection of the occurrence of solidification at 26.5 °C, which is exactly the same result as in the former experiment. It can be concluded thus that the sensor is capable of providing reliable phase information even when it operates in a more realistic non-laboratory environments where solidification or melting is not unidirectional. This also shows the potential of the sensor to deal well with real-world conditions than the sensor proposed in the former chapter. Moreover, the SNS fiber sensor only requires a single measurement to correctly detect the current phase state of the material. However, the sensor can be only applied in the PCMs which display a step-like RI change during the phase transition. The novelty, advantages and disadvantages are summarized in Table 5.1

Table 5.1. Novelty, advantages and disadvantages of the SNS fiber sensor.

Novelty/advantages	<ol style="list-style-type: none"> 1. Resistance to external perturbations (cross-sensitivity) 2. High spatial resolution 3. Only requires a single measurement to achieve detection
Disadvantages	<ol style="list-style-type: none"> 1. The application is limited by the RI of the PCMs

5.4 Conclusion

A novel optical fiber sensor based on an SNS fiber structure for detection of the phase state of n-octadecane has been proposed and demonstrated experimentally

in the chapter. From the experimental results it can be seen that the melting point is approximately 27.5 °C and solidification occurs at 27 °C, which is very close to the values reported in literature [97]. Since the output power level of the sensor changes abruptly from low to high with the transition of n-octadecane from solid to liquid state (and vice versa), detection of the specific phase of the n-octadecane can be realized with a single power measurement and without the knowledge of the sample's temperature. It should be noted that in the former chapter, the Peltier element was placed on the top of the container for minimizing the external perturbations, such as the influence from thermal convection, but in this chapter, the sample was heated and cooled from the bottom. This is because compared to the Fresnel-reflection fiber sensor proposed in the previous chapter, the SNS sensor offers better performance in terms of resistance to external perturbations, such as the occurrence of bubbles, impurities and mechanical disturbances. Besides it only requires a single measurement to detect the phase state, while the Fresnel-reflection sensor requires at least two measurements. The results of this work suggest that the proposed sensor is potentially capable of detecting liquid-solid and solid-liquid phase changes in other materials whose thermo-optic properties are similar to those of n-octadecane, namely in the materials whose phase transitions are accompanied by a step-change of refractive index between the values lower and higher than that of the silica fiber at the operating wavelength of the optical source.

Chapter 6 Optical fiber Fabry-Perot sensor based on a singlemode-hollow core-singlemode fiber

6.1 Introduction

In the previous chapter an SNS fiber sensor for phase change detection in n-octadecane was proposed. Although it has the advantages of resistance to external perturbations and only requires a single measurement to achieve detection, it cannot be used for the detection of phase changes in materials with a continuous RI change during the phase change, or the materials for which the RI of both solid or liquid phases is lower or higher than that of the fiber core, (e.g., the RI of ice is 1.3 and the RI of water is 1.33, which are both smaller than that of silica glass). To overcome this shortcoming, it is necessary to find out a new phase change measurement method which does not necessarily rely on a sharp change in the material's RI during the phase change. In this chapter a Fabry-Perot (FP) fiber sensor is proposed and experimentally demonstrated whose operation does not rely on RI changes in the PCM.

As it is shown in Fig. 6.1, the sensor probe is fabricated by splicing a short section of a HCF, with a length in the order of microns, between two SMFs, to form a single-mode-hollow core-single-mode (SHS) FP fiber sensor. Light from a broadband source launched into the input SMF (SMF-1) experiences multiple reflections due to the differences in RI at the interfaces between the SMF-1 and

HCF, between the HCF and the second SMF section (SMF-2) and between the end face of SMF-2 and the material under test. The portion of light reflected back from the end face of SMF-2, as a result of Fresnel reflection at the glass-PCM interface, travels through the same series of interfaces in the reverse direction creating an output interference spectrum which contains multiple interference dips. Compared to the sensors proposed in the former chapters, the interference dips arise from the light propagating in different fibers, not from modes in the same fiber. Any phase changes of the material sample in the vicinity of the fiber probe result in changes in the various parameters acting upon the probe (such as temperature, strain or bending) which in turn will cause the shift of the output interference spectrum. With the probe immersed into the material sample the phase change is detected by monitoring the wavelength shift of the selected interference dip.

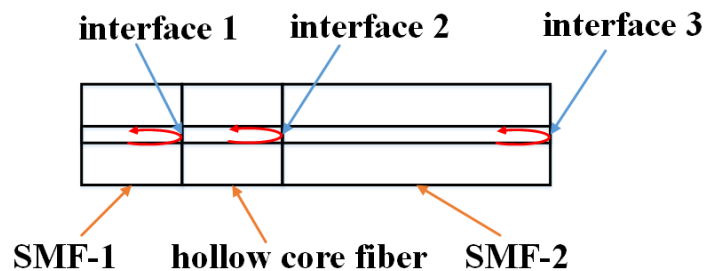


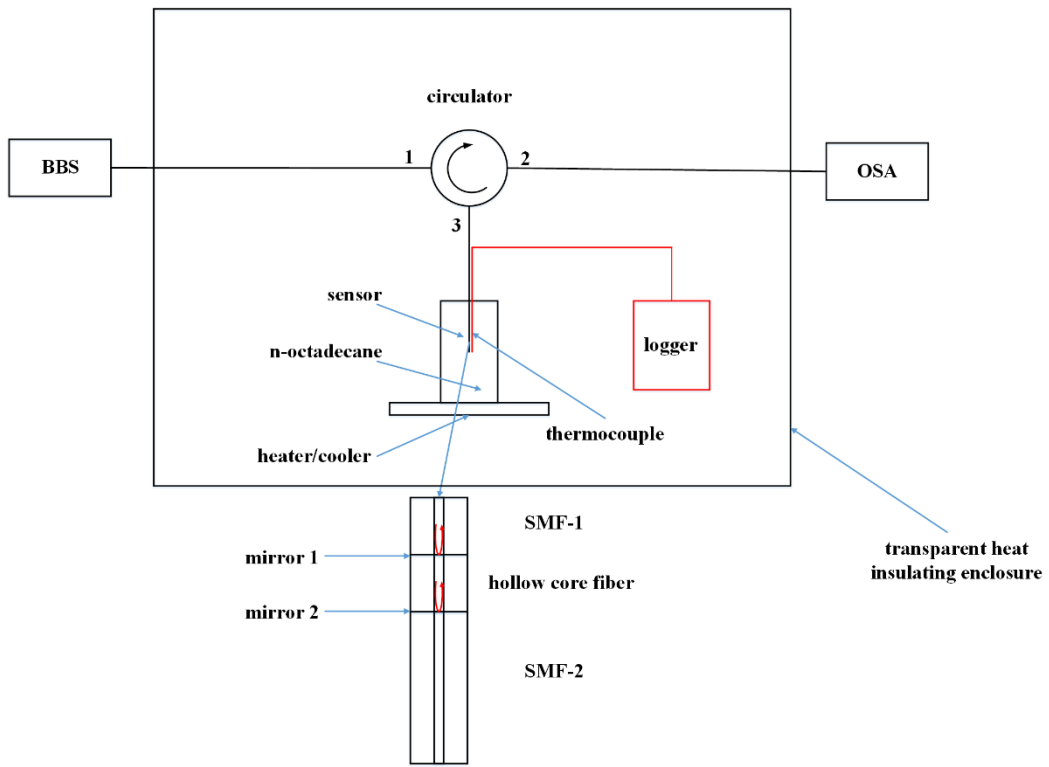
Fig.6.1 Schematic diagram of the sensor probe.

In this chapter, n-octadecane was again chosen for a proof-of-principle demonstration of the proposed fiber sensor due to the same reasons as in the former chapters. Although the RI of n-octadecane changes in a step-like manner when the material undergoes the solid-liquid phase transition, the sensor proposed here is based on an FPI structure which is fabricated in a manner so that that the sensor is unaffected by local RI changes but is influenced by the changes in stress placed on the sensor by the solid phase. By monitoring the spectrum it is possible to

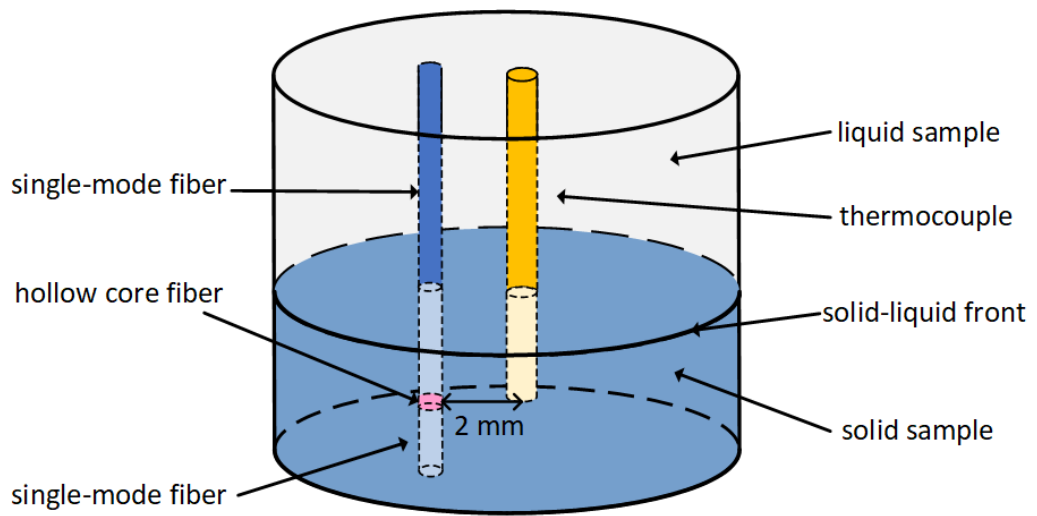
distinguish between the solid and liquid phases and thus to determine the solidification temperature. It is shown that the method proposed in this chapter can be used for accurate in-situ detection of liquid-solid and solid-liquid phase changes in n-octadecane, without the need for RI measurements. This point-sensing technique could in principle be expanded by increasing the number of sensor probes to create a sensor array for detecting the phase change at several points within a PCM, for example, in studies and optimization of heat distribution within a PCM material employed in energy storage systems. This work has potential applications in studies of phase changes in PCMs facilitating a deeper understanding of the underlying physical mechanisms.

6.2 Experimental setup and operating principle

The experimental setup for the demonstration of the proposed sensor is shown in Fig. 6.2. Port 1 of the optical circulator is connected to a broadband light source (BBS) S5FC1005S(P), Thorlabs), while port 2 is connected with the fiber sensor probe and port 3 is connected to an optical spectrum analyzer with the resolution of 0.02 nm (OSA Q8384, Advantest).



a



b

Fig.6.2 (a) Schematic diagram of the experimental setup. (b) 3D image of the sensing area

The probe is fabricated from a very short (300 μm) section of a HCF (10 μm inner air core diameter, 126 μm outer silica cladding diameter) with its coating removed. The HCF section is “sandwiched” between two sections of a standard single-mode fiber (SMF-1 and SMF-2) by means of fusion splicing. Due to the limitations of the fiber cleaver, 300 μm was the shortest length for the HCF fiber which was fabricated in this research, but even shorter lengths could potentially be obtained. The length of SMF-2 is 1 cm. The protective fiber coating was removed from a small area near the end of SMF-1 then it was spliced with the sensor probe and this area was marked with blue ink. Since the liquid sample is transparent while the solid sample is not, visual observation of the blue mark can be used to determine if the sample is in the liquid phase. The temperature in the vicinity of the fiber probe was monitored with a K- type thermocouple with the error of ± 1.1 $^{\circ}\text{C}$. The thermocouple was fixed close to the probe, which is approximately 2 mm away from the sensor. From the figure it can be seen that the temperature of the sample measured by the thermocouple is not the exact temperature of the sample at the detection point, but is very close to it and thus can be still used to validate the reliability of the fiber sensor. Moreover, since the heating experiment lasts for approximately two hours and the cooling experiment lasts for approximately four hours, the temperature change of the n-octadecane is very slow and the data were collected when the temperature of the sample is stable, thus the data collection process is considered to be reliable.

A Peltier element with the rated voltage of 12 V was used as a thermoelectric heater/cooler, with the maximum power of 60 W, placed at the bottom of the container filled with n-octadecane.

Light from the BBS, launched into SMF-1 experiences partial reflections at the interfaces between SMF-1 and HCF (mirror 1) and between the HCF and the SMF-2 (mirror 2), as illustrated in Fig. 6.2. A portion of the light reflected at mirror 2 is recoupled back in the SMF-1 where it interferes with the light reflected by mirror 1. Additionally, a portion of the input light transmitted through mirror 2 experiences further reflections at the end face of SMF-2 (interface 3). Some of the light reflected from the end face of SMF-2 is re-coupled into the HCF and interferes with the light reflected by mirror 2. It should be noted that SMF-1 is effectively a connecting fiber and its length does not have any effect on the spectrum because it does not form part of a Fabry-Perot cavity.

The HCF section spliced between the two SMFs can be considered as an air cavity with the ends of SMF-1 and SMF-2 acting as cavity mirrors (mirror 1 and 2). The SMF-2 forms the second cavity, where reflections occur at mirror 2 and the cleaved end of the SMF-2, acting as the third mirror. Thus the entire structure can be viewed as two cascaded FPIs. A free spectral range (FSR) for an FPI can be determined from the expression [100]:

$$FSR = \frac{\lambda_1 \lambda_2}{2nL} \quad (6.1)$$

where λ_1 and λ_2 are the neighboring dips in the interferometer's spectrum, n and L are the RI and the length of the FPI cavity respectively. As one can see from the formula, the FSR is inversely proportional to the length of the cavity. The sensor proposed in this paper has two cavities: the HCF and the SMF-2. For the HCF cavity, the value of n is the RI of the core of the HCF (air) and L is the length of the HCF. For the SMF-2, the value of n is the RI of the core of the SMF-2 and L in this case in equation 6.1 is the length of the SMF-2.

The length of the SMF-2 establishes the optical path difference between the light reflected by mirrors 2 and 3. To better understand the properties of the proposed fiber structure the effect of length of SMF-2 on the reflection spectrum was investigated. Three fiber structure samples were fabricated as follows. Three samples with the HCF lengths of $\sim 300 \mu\text{m}$ and SMF-2 lengths of 1 cm, 1.5 cm and 2 cm were selected. Fig. 5.3 shows the experimentally measured spectra for the above samples with different SMF-2 lengths.

In order to eliminate the effect of variations in the light source spectral flatness on measurements, the measured spectral response of the sensor was normalized with respect to the spectrum of the BBS. From Fig. 6.3 it can be seen that changes in the length of the SMF-2 section do not significantly affect the fiber probe's spectrum, which means that the effect of the FPI formed by the SMF-2 can be neglected. It is for this reason that the length of the FPI formed by SMF-2 is deliberately set to be much longer than the length of the HCF, in order that the corresponding FSR is much smaller by comparison to that associated with the HCF cavity. The ripples appearing in the spectra in Fig. 6.3 are thus associated only with the HCF cavity. Note that the vertical axes in Fig. 6.3 and Fig. 6.4 are in dB rather than dBm as they both show spectra normalized to the input spectrum of the BBS.

In further experiments the lengths of the HCF and SMF-2 were set to $300 \mu\text{m}$ and 1 cm respectively, and a typical output spectrum for the probe is shown in Fig. 6.4.

Due to the variations in the environment surrounding the fiber probe, the length of the HCF cavity may change. In addition, as the environmental temperature changes, the temperature and the pressure within the HCF core may also change, changing

the effective RI for the modes propagating within the HCF core. The spectral shifts of the interference dips as described in [101] are given by:

$$\Delta\lambda = \lambda\left(\frac{\Delta n}{n} + \frac{\Delta L}{L}\right) \quad (6.2)$$

where λ is the central wavelength of a selected dip, Δn and ΔL are the variations of the RI and the length of the air cavity respectively. Assuming that only the temperature of the medium surrounding the probe environment changes, equation (6.2) can be differentiated as

$$\frac{d\lambda}{dT} = \lambda\left(\frac{1}{n}\frac{dn}{dT} + \frac{1}{L}\frac{dL}{dT}\right) = \lambda(\delta + \alpha) \quad (6.3)$$

where α is the thermal expansion coefficient of the HCF and δ is the effective thermo-optic coefficient of the HCF cladding. From equation (6.3) it can be seen that the wavelength shift of the selected dip caused by a temperature variation is a linear function of temperature.

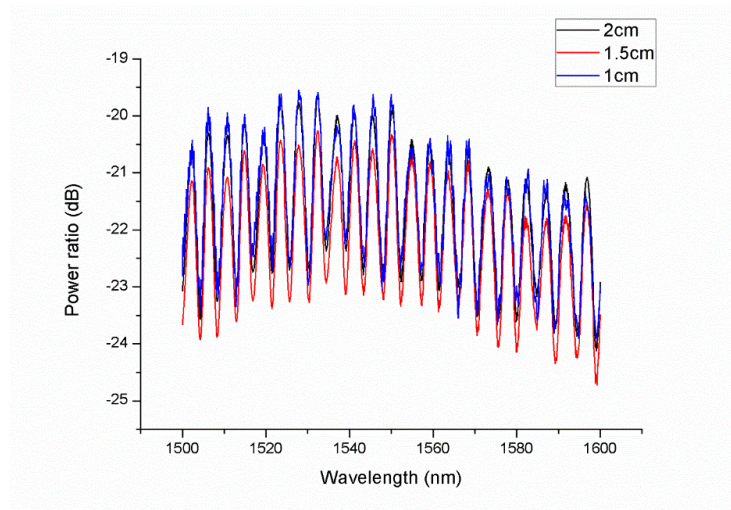


Fig.6.3 Experimental spectra of the fiber probes with different lengths of SMF-2.

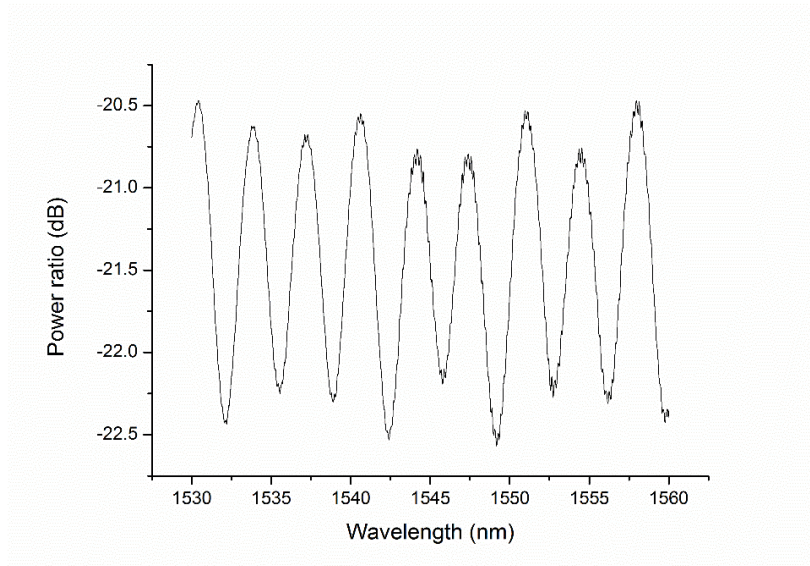


Fig.6.4 Typical experimental reflected spectrum of the sensor probe.

As it can be seen in Fig. 6.4, the spectrum has a strong periodic component, the lowest point in each period is regarded as an interference dip. When the fiber probe is immersed in the material undergoing the phase change from solid to liquid, the temperature change of the material, as well as the variation in the material's density leads to strain and bending forces acting upon the fiber, in turn causing spectral shifts of the interference dips [102-104]. Since the speed of the liquid phase front propagation may vary at different points within the sample, the direction and amplitude of the strain and the bending forces acting on the sensor probe are random in nature, resulting in a non-monotonic wavelength shift of the interference dips within the reflected spectrum. As soon as the sensor becomes fully immersed in liquid, the strain and the bending forces, significant in the solid phase, become negligibly weak so that the influence of temperature dominates the changes in the spectral positions of the interference dips, leading to a linear behaviour consistent with the temperature response of the probe, described above. Therefore by analyzing the dependence of the wavelength shift of a selected spectral dip within the sensor's reflection spectrum versus the material's

temperature, it is possible to determine the temperature point at which the nature of the dependence changes from non-monotonic to linear (or vice versa in the case of liquid to solid transition), thus the phase change can be detected.

6.3 Experimental results and discussion

6.3.1 Experiment preparation and setup

As a first step towards the phase change experiments, the temperature dependence of a selected spectral dip was investigated. The spectral dip at 1549 nm was chosen for this purpose as it is the dip with the highest extinction ratio and as such is easy to be observed. To improve the reliability of the measurement, the average wavelength of the zero-crossings of the selected dip was used for the detection. Since the amplitude of the selected dip changed during phase change, and the range of it was from 1 to 2 dB, thus the zero-crossings were identified by finding out the intersection points of the selected interference dip with the horizontal line which was 1 dB higher than the lowest point of the dip. The temperature response of the fiber probe was measured using the experimental setup shown in Fig. 6.2. To provide an initial reference for later experiments, water was used at this point as the material sample instead of n-octadecane. The water sample was heated from 20 °C to 30 °C in 1 °C steps and the corresponding changes in the spectral position of the selected interference dip were recorded. The measurement result is shown in Fig. 6.5, from which it is observed that the temperature response is as expected approximately linear and that the temperature sensitivity of the probe is estimated as 0.006 nm/°C. It should be noted that since the water sample does not undergo phase changes within the studied temperature range, the observed spectral shift of the interference spectrum is solely due to the temperature induced change in the

HCF's RI caused by the thermo-optic effect, and the changes in the size of the HCF caused by thermal expansion.

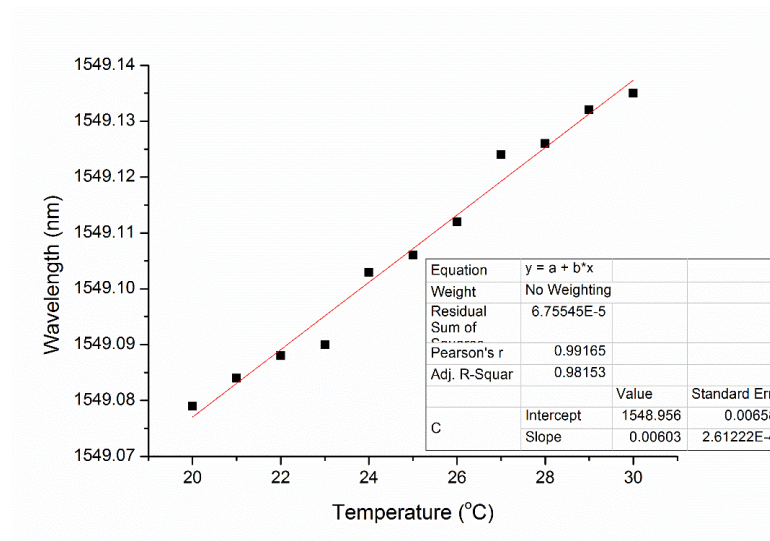


Fig.6.5 Temperature response of the sensor probe.

In order to experimentally demonstrate the operation of the proposed sensor, a series of heating and cooling experiments were carried out for a 19.4 g sample of n-octadecane with 99% purity (Sigma Aldrich) in a cuvette with a diameter of 3 cm and height of 4 cm, using the same experimental setup. The fiber probe and a thermocouple were immersed into the n-octadecane sample with an approximate 2 mm distance between the fiber probe and the thermocouple.

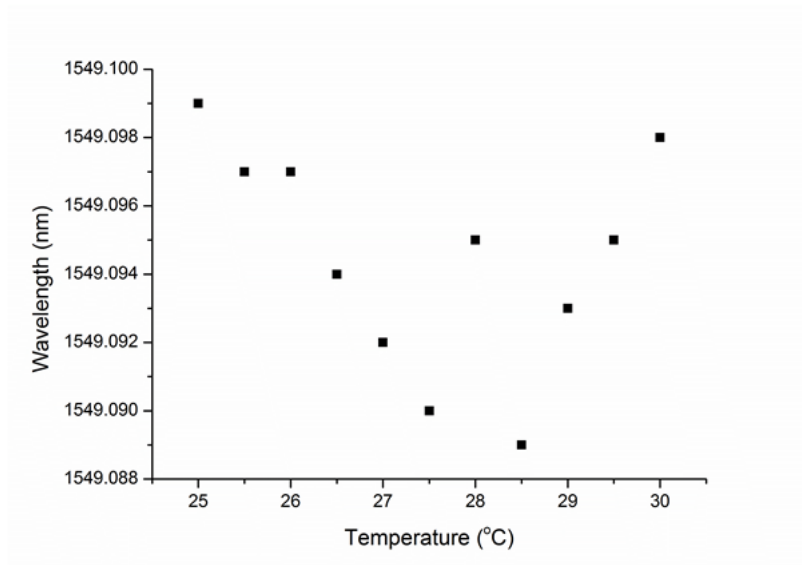
The sensor is placed inside the material sample to ensure that the sensor is always inside the sample even though the volume of the n-octadecane sample changes before and after the phase change. The thermocouple was connected to a logger to record the temperature of the n-octadecane in close proximity of the fiber sensor probe. To ensure stability of the surrounding temperature, the experimental setup was placed inside a transparent heat insulating enclosure. A photo camera was placed inside the enclosure and connected with a laptop for recording images. The

camera's shutter was controlled by the PC and a photo image was taken each time the wavelength of the selected dip and temperature data were recorded.

6.3.2 Experimental results

The wavelength of the selected dip in the heating experiment are shown in Fig. 6.6. The heating experiment was carried out by setting the temperature of the Peltier element to 50 °C causing progressive melting of the sample from the bottom of the cuvette so that the liquid phase front propagated slowly upwards through the sample, where the temperature of the surrounding environment was set as 20 °C to ensure a well-defined sharp interface between the solid and liquid n-octadecane. As can be seen from Fig. 6.6 (a) in the temperature range from 25 °C to 30 °C, the wavelength shift of the selected spectral dip is distinctly non-monotonic by comparison to the temperature response curve in water in the temperature range from 27.5 °C to 28.5 °C. It is linear when the temperature is above 28.5 °C. As one can see from Fig. 6.6 (b) the slope of the linear section of the temperature dependence is 0.0058 nm/°C, which is very close to the temperature sensitivity (slope) measured in water. Below 27.5 °C the slope is opposite in sign to the slope above 28.5 °C. This is due to the fact that before the material melts into liquid, as the temperature increases, the combined effects of the multi-directional strain forces acting upon the sensor are the primary cause of the wavelength shift of the selected dip. Since the strain and bending forces arise from the variation in the material's density and the propagation speed of the liquid phase front, these forces may vary at different points within the sample, the direction and amplitude of the strain and the bending applied to the fiber causes a distinct wavelength shift which is very different from the linear spectral responses observed below 27.5 °C and

above 28 °C. Once the material sample becomes liquid, the strain forces acting upon the fiber become weaker and more uniform and the surrounding temperature becomes the dominant factor. By recording the spectral response changes with temperature, the change from a solid to a liquid phase can be distinguished and thus from Fig. 6.6 it can be seen that the phase change of the sample occurs at 28.5 °C. Fig. 6.7 presents a series of photos that show the gradual movement of the interface between liquid and solid phases during the heating experiment. It can be seen that when the temperature is lower than 28 °C, the sensor is not visible, which proves that it is in solid before melting. When the temperature reaches 28.5 °C, the sensor becomes visible, which proves it is in liquid after melting. The process shown in Fig. 6.7 is consistent with the heating experiment result.



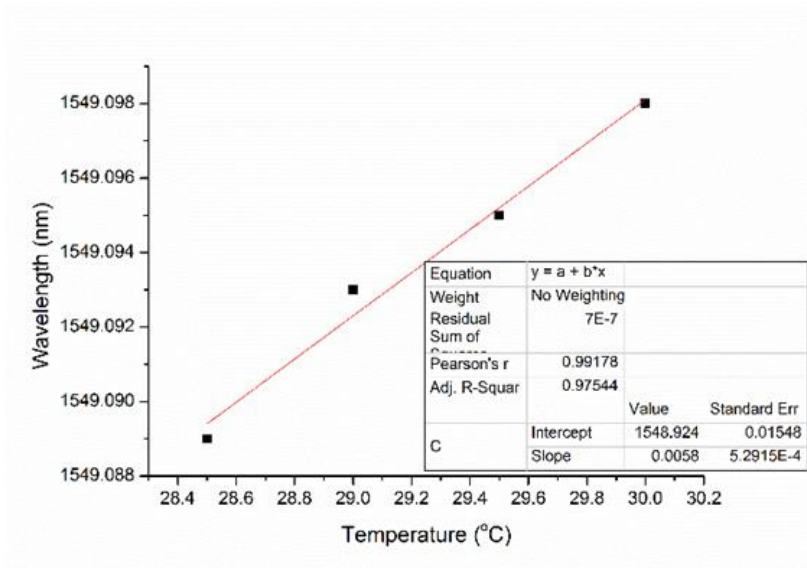


Fig.6.6 Heating experiments results: (a) dip wavelength shift during the heating cycle; Fig. 6.6 (b) dip wavelength shift after the sample melts into liquid.

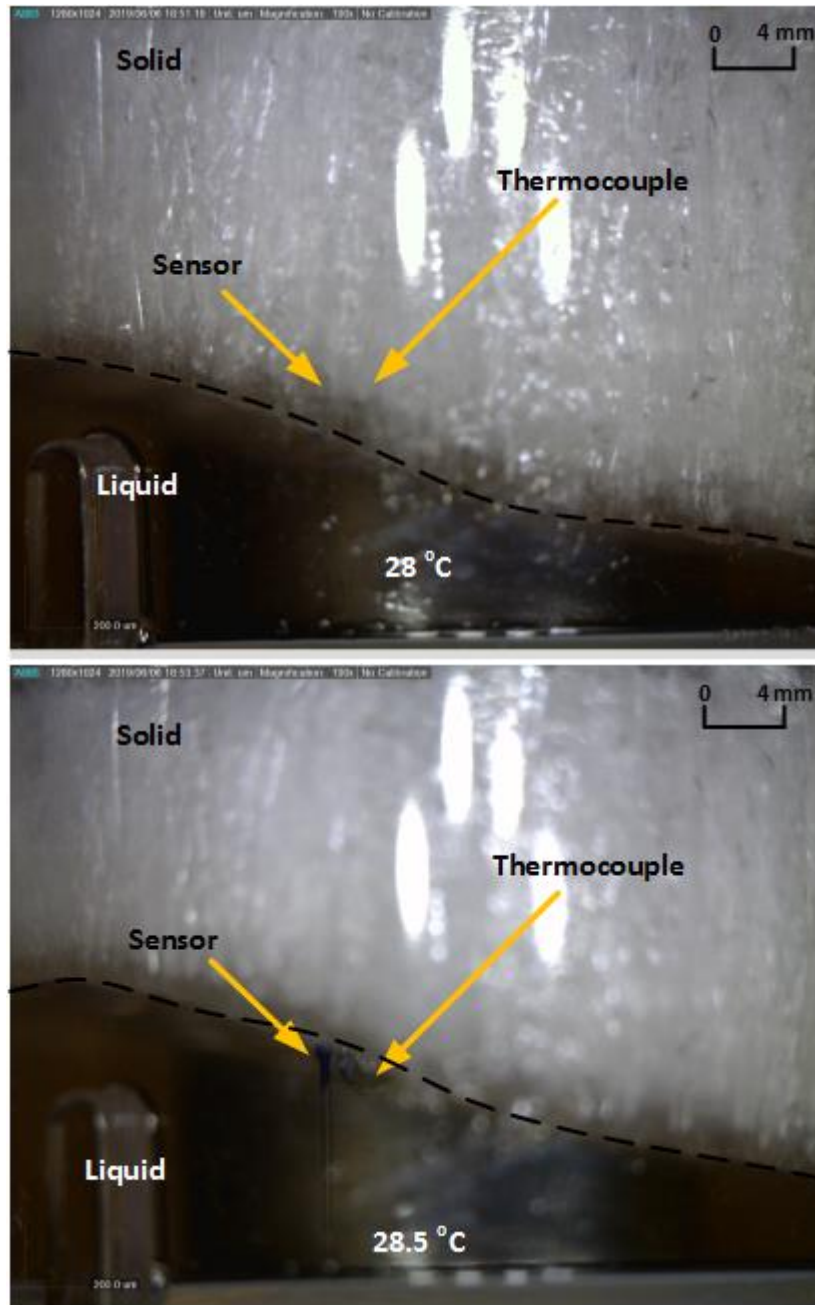
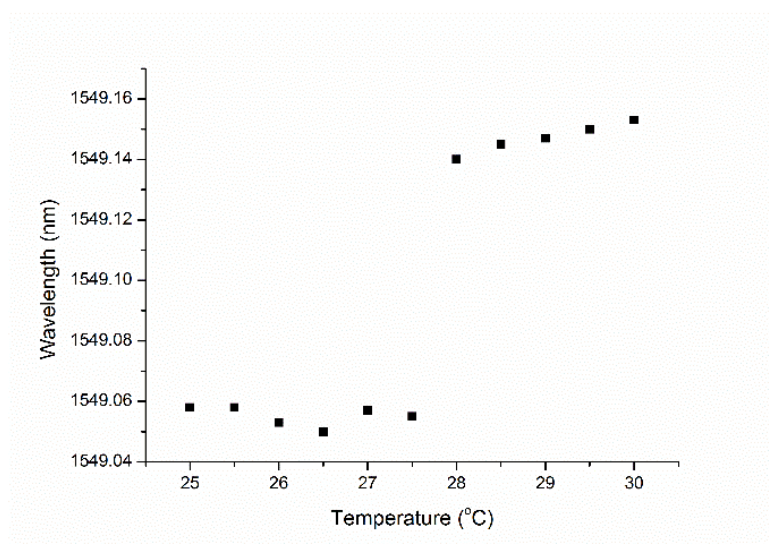


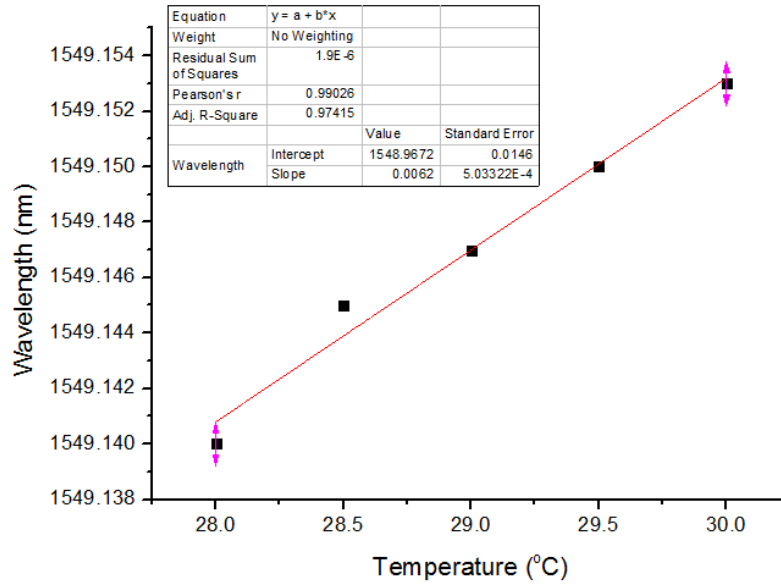
Fig.6.7 Photographs of the solid-liquid interface position at different temperatures: at 28.5 °C both the thermocouple and fiber optic probe tips are clearly visible.

For the cooling experiment the current direction within the Peltier heater was reversed so that the cold side of the heater was in contact with the sample, causing solidification from the bottom of the cuvette slowly upwards through the sample and again produced a visible interface between the liquid and solid phases that was recorded by the camera. The temperature of the Peltier element was set to 10 °C,

while the temperature of the surrounding was set to 30 °C to ensure a well-defined sharp interface between the solid and liquid n-octadecane. The wavelength of the selected dip is shown in Fig. 6.8. From Fig. 6.8 (b) it can be seen in the temperature range from 30 °C to 28 °C the wavelength shift is linear and the slope is 0.0062 nm/°C, which is very close to the temperature response of the probe in water. This is due to that when the temperature is higher than 28 °C, the sample is in a liquid phase, and the wavelength position of the dip is affected only by temperature. From 27.5 °C to 24 °C the changes in the spectral position of the selected dip becomes non-monotonic, as can be seen in Fig. 6.8 (a).



a



b

Fig.6.8 The cooling experiment spectral results: (a) the dip wavelength shift during the cooling cycle (b) the dip wavelength shift before the sample solidifies.

When the temperature becomes lower than 28 °C, the sample is surrounded by solid n-octadecane. In the solid phase as the temperature decreases, the strain forces acting upon the sensor increase due to the increased density of the material, resulting in randomly directed stress and bending forces acting upon the fiber probe, resulting in a non-linear behaviour of the selected dip for the data points below 27.5 °C. From Fig. 6.8(a) it can be seen that the phase change occurs at 28 °C on cooling. The images in Fig. 6.9 show the gradual movement of the interface between liquid and solid phases during the cooling experiment. When the temperature is 28 °C, the sensor is visible, which proves that the sensor is in liquid before the solidification of the sample. However, the temperature reaches 27.5°C, the sensor is invisible, which proves that the sensor is in solid sample when n-octadecane is solidified. The whole process shown in Fig. 6.9 is consistent with the cooling experiment results. The material is liquid when the temperature is 28 °C and it becomes solid at the temperature of 27.5 °C, which confirms the result

of the fiber probe experiment. The solidification temperature in the cooling experiment is lower than the melting temperature in the heating experiment due to the known small thermal hysteresis of n-octadecane [105]. The wavelength shift when the sample is solid on heating and on cooling are different because the strain and bending forces in each cycle of the experiment are different, so the wavelength shift associated with a solid sample is not repeatable. However since the rate of the wavelength shift for a sensor immersed in a liquid phase is highly repeatable, the phase change point can be accurately detected.

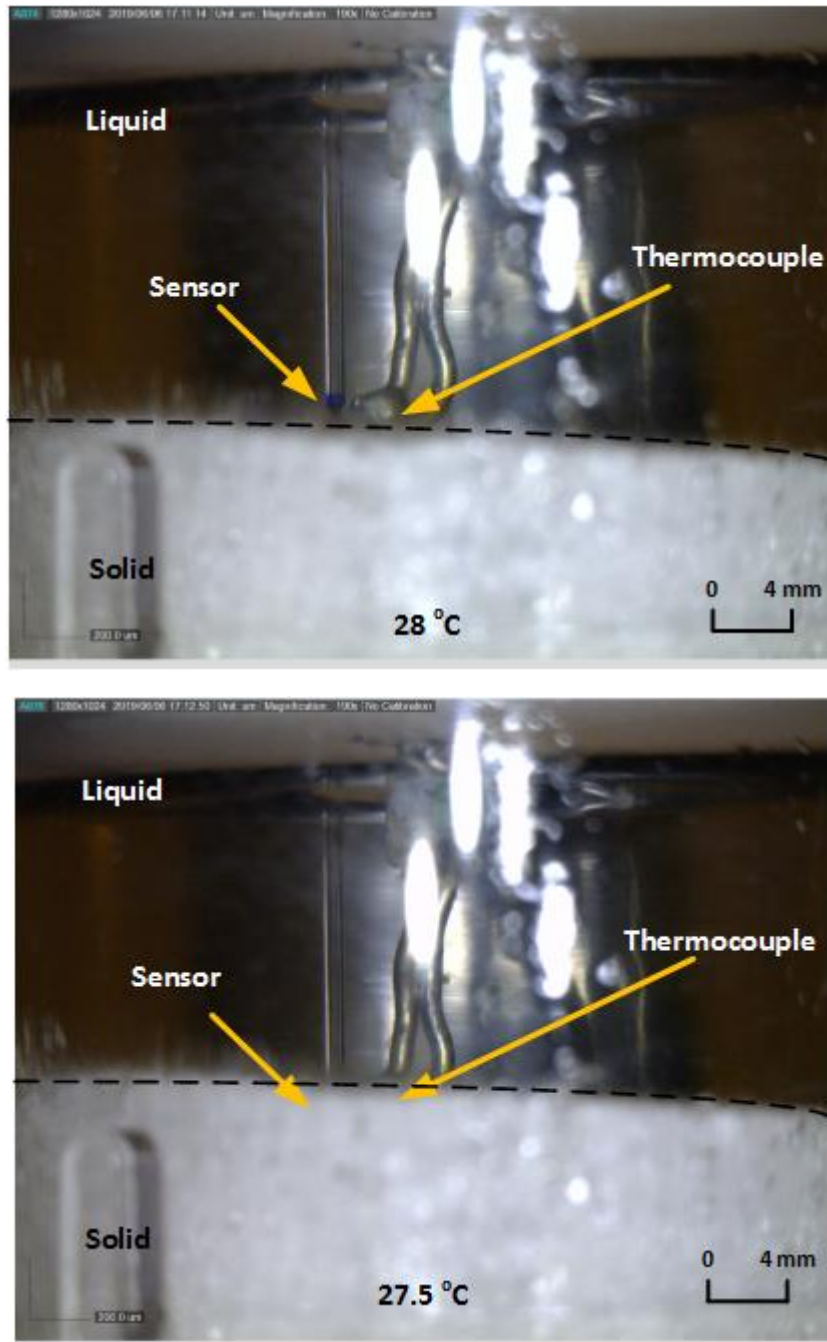


Fig.6.9 Photographs of the solid-liquid interface position at different temperatures: at 28 °C both the thermocouple and fiber optic probe tips are clearly visible while they are immersed in the solid sample at 27.5 °C.

A side-by-side comparison of the heating and cooling results is shown in Fig. 6.10. From the figure it can be seen that the wavelength shift changes in the cooling experiment are larger than those in the heating experiment. One reason for this is that both the direction and value of the strain and curvature change for the sensor are different and non-repeatable between heating and cooling cycles. It also can be

seen that the initial characteristic wavelength of the dip is not the same at the start of the heating and cooling experiments. The reason for this is that the initial conditions of the sensor in heating and cooling experiments are different, which causes the slight difference on the characteristic wavelength of the dip.

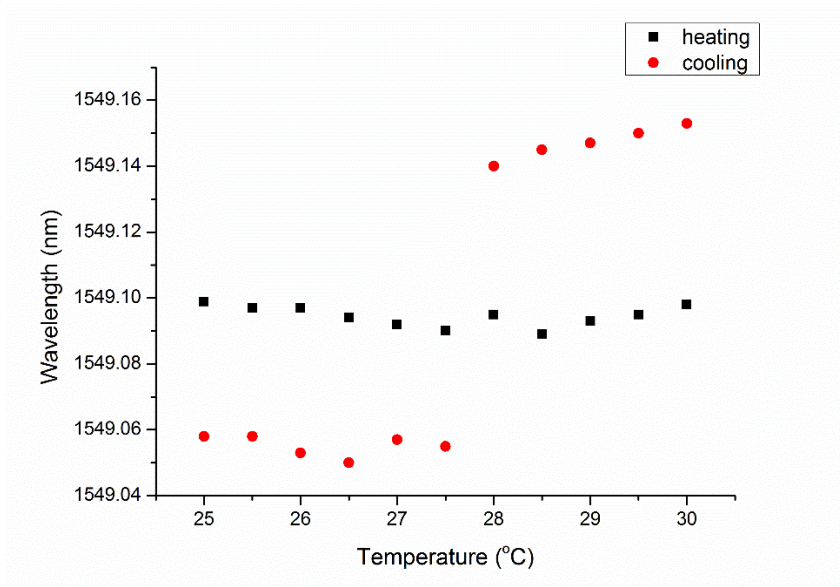


Fig.6.10 The comparison of the heating and cooling experiment results.

It should be noted that the phase change temperature measured by this sensor is slightly different from the data [97], and a possible reason for this is the differences in positions of the thermocouple and the degree of smoothness of the solid-liquid interface in each experiment. Since the proposed method of phase change detection relies on the comparison between the measured slope of the wavelength shift of the selected dip with temperature with the known value of the temperature slope in liquid, its accuracy depends on several factors including measurement error of the thermocouple and the distance between the thermocouple and the sensor. In addition, the measurement sampling interval is an important factor as the accuracy of detection increases with the increase of the number of consecutive data points used for the linear fitting and comparison between the slopes. It also should be

noted that the wavelength accuracy of the OSA is $\pm 0.02\text{nm}$, and the temperature sensitivity is $0.006\text{ nm}/^\circ\text{C}$, thus the accuracy of temperature measurement is $\pm 3.3^\circ\text{C}$. The temperature accuracy can be improved by using an OSA with higher accuracy. Besides, the temperature measurement is not the target, the result of the temperature measurement is only used as a reference. The reliability of the sensor is proven through visual means. From the above experiments it can be seen that the applications of the Fabry-Perot fiber sensor are not limited by the RI of the PCMs, and it has the novelty of utilizing cross-sensitivity to achieve phase change measurement. However, its disadvantage is the need for more than one measurement to achieve phase change detection. The novelty, advantages and disadvantages are summarized in Table 6.1.

Table 6.1. Novelty, advantages and disadvantages of the Fresnel fiber sensor.

Novelty/advantages	<ol style="list-style-type: none"> 1. Utilizes cross-sensitivity to monitoring phase change 2. Not limited by the RI of PCMs
Disadvantages	<ol style="list-style-type: none"> 1. Need for continuous monitoring (sampling) of the output power

6.4 Conclusion

In conclusion, a novel method with the potential for in-situ detection of the solid-liquid and liquid-solid phase changes in n-octadecane, based on a Fabry-Perot SHS optical fiber probe has been proposed and demonstrated. From the experimental results it can be seen that the phase change point is approximately at 28.5°C on heating and 28°C on cooling. The proposed method allows for a simple, accurate and reliable in-situ detection of the liquid-solid and solid-liquid phase changes in

n-octadecane. In contrast to the sensing system presented in chapter 4, here the Peltier element was placed at the bottom of the container. This was possible due to much better immunity of the sensor to external perturbations, such as the occurrence of bubbles, impurities and mechanical disturbances. Moreover, compared to the sensors described in previous chapters, the application of the proposed sensor is not limited by the RI of the PCMs. This point-sensing technique can be expanded by increasing the number of sensor probes and can be applied to studies and optimization of heat distribution within PCM materials employed in energy storage systems. The sensor is capable of providing accurate information regarding phase change and phase state, which is important in studies of phase change mechanism and energy storage applications. the proposed method has potential applications in studies of phase changes in PCMs facilitating a deeper understanding of the underlying physical mechanisms.

Chapter 7 Conclusions and future work

In this chapter, the conclusions resulting from the research described in this thesis and the key contributions to knowledge are presented. Future work as a possible extension of this thesis is also discussed.

7.1 Conclusions from the research

The main goal of this research is the development of a new and accurate method for in situ detection of phase states and phase changes in phase change materials, based on optical fiber sensors. In Chapter 1, a series of objectives were identified to meet the aim stated above. The main findings and conclusions presented and discussed here are divided into four sections based on the different objectives and research strands investigated and reported in this thesis as follows. The specific objectives identified in Chapter 1 of this thesis of this research are as follows:

1. *Identify, investigate and analyze most suitable types of optical fiber sensors as a basis for the sensing system capable of monitoring liquid-solid phase transitions in PCMs.*

This has been achieved by designing, fabricating and experimentally validating three optical fiber sensors based on different operating principles. The operation of the Fresnel-reflection based fiber sensor and the SNS fiber sensor relies on changes in the refractive index of the PCM due to the phase transition, resulting in changes of the output transmitted or reflected by the sensor light power. The operating principle of the Fabry-Perot fiber sensor is underpinned by the relationship between the sensor's output and the strain, pressure and bending forces acting upon the sensor during the material's phase

change. Compared to the traditional methods of phase change detection, all three novel sensors proposed and developed in this thesis have the advantages of capability of in-situ detection of phase changes in PCMs, high reliability and simple structure. Moreover, each of the proposed sensor structures offers its own unique advantages as follows:

- The Fresnel-reflection based fiber sensor due to its small size provides high spatial resolution in point measurements.
- The SNS fiber sensor has the capability of detecting the phase change based on a single measurement as opposed to the need for continuous monitoring of the output power level.
- The Fabry-Perot fiber sensor has the advantage of that its working principle does not depend on the change of PCM's RI. This allows to expand the range of PCM materials the sensor can be used with, since there is no longer the need for the material to satisfy certain conditions for its RI values.

The suitability of the proposed fiber optic sensors for the detection of solid-liquid and liquid-solid phase changes has been demonstrated experimentally for a typical PCM n-octadecane sample in laboratory conditions.

2. *Develop appropriate analytical models to establish the relationship between physical parameters of PCMs during the phase changes and the corresponding output signals (or spectra) of the selected fiber optic sensors.*

Theoretical analyses have been carried out for all three proposed sensors.

For the Fresnel-reflection based fiber sensor, a simple analytical model based on Fresnel equations has been developed and the sensor's output power as a function of the material's RI has been simulated (Fig.4.2). It is shown that temperature and phase induced changes of the PCM's refractive index influence the light power output from the sensor and the phase change can be accurately and reliably identified by finding an inflection point within the output power dependence. The results of theoretical analysis and simulations are in a good agreement with experiments.

For the SNS fiber sensor, a model based on the beam propagation method has been developed and the influence of the surrounding RI on the sensor transmission was analyzed using commercial BeamPROP software package. It is shown that if the RI of the solid PCM is larger than that of the no-core fiber, the total internal reflection condition is violated and light is no longer confined to the fiber, leading to low output power. If during its solid-liquid transition the PCM changes its RI to a value lower than that for the fiber, light remains confined to the fiber probe and the sensor's output is high. The phase change can be detected by observing the level of the output power ratio.

For the Fabry-Perot fiber sensor, using an analytical model (equation 6.3), it is determined that the wavelength shift of the interference dips occurs due to changes in temperature, strain and bending forces acting upon the fiber. In the phase change process, when the sensor is surrounded by a solid PCM all of the above factors influence the positions of the spectral dips, causing non-linear shift of the sensor spectrum with temperature. Once the phase transition occurs and the PCM becomes liquid, the wavelength shift of the selected dip is predominantly due to temperature influence and is a linear function of

temperature. Most importantly, the value of the spectral shift of the selected spectral dip in the sensor's transmission spectrum experiences a step-like change during both solid-liquid and liquid-solid phase changes, thus by monitoring the spectral shift of the selected dip phase change can be detected.

3. *Develop an experimental setup capable of accurate control of phase changes in the material sample, including control of the speed of heating/cooling and thermal convection. Identify a suitable PCM for verification of the analytical models and experimental demonstration of the potential of the proposed sensor system.*

In order to realize accurate temperature control of the PCM, a transparent temperature insulating enclosure was used to stabilize the temperature of the material sample's environment. The insulating enclosure allowed to reduce the influence of temperature fluctuations in the laboratory environment leading to a better control of the speed of heating and cooling of the PCM sample. The Peltier element placed at the outside wall of the container was used to control the temperature and speed of heating/cooling of the sample.

In the Fresnel-reflection based fiber sensor experiment, it was necessary to eliminate the thermal convection within the PCM sample, which causes disturbances in the sensor response. For this purpose the Peltier element was attached to the top of the container.

To validate the performance of the fiber optic sensors, a thermocouple and a digital camera were used simultaneously during experiments. The thermocouple was placed in the vicinity of the optical fiber sensor and its readings were used as temperature reference. The digital camera was used to

take photos of the PCM sample focusing on the area with thermocouple and fiber optic sensor. Since the chosen PCM (n-octadecane) displays visible changes in its transparency between the milky-white appearance in its solid phase and a transparent liquid phase, the location of the phase front is visually observed and recorded by the camera. This allowed one to validate the data from the proposed sensors experimentally by analyzing the movement of the phase front from the series of images taken by the camera.

4. *Identify the factors that cause random disturbances of the sensors' performance and develop techniques to minimize the disturbances and increase reliability of detection using optical fiber sensors. Develop methods to realize reliable measurement under the cross-sensitivity issues of individual fiber sensors.*

In the phase change process, many parameters of the PCM such as density, volume, RI, and temperature undergo changes at the same time. When a sensor relies on monitoring of only one of the parameters (for example, RI) in order to detect the phase change, other influences such as temperature, pressure and strain forces due to the changes in volume and density of the sample can cause a measurement error, which is known as cross-sensitivity. Other disturbances could arise as a result of thermal convection or the formation of air bubbles in the liquid phase.

In this research the air bubbles and the thermal convection were identified as major sources of disturbances and measurement inaccuracies. To eliminate these effects, the PCM was heated/frozen from the top to suppress the convection, thus only the RI change of the PCM affected the output power.

The proposed SNS fiber sensor is sensitive to strain, bending and the RI of a PCM with all of the above parameters influencing the sensor output. However it was determined that although the strain and bending cause fluctuations of the output power in the solid phase, their magnitude is negligibly small compared to the power difference caused by the RI change during the phase transition.

The proposed Fabry-Perot fiber sensor relies on the measurement of the slope of the wavelength shift of the selected dip and its comparison with the temperature sensitivity. If the wavelength shift with temperature is different from the calibrated temperature response, this indicates the presence of strain and bending forces and thus the sample is in the solid state. If sensor response coincides with the calibrated temperature sensitivity the sample is judged to be in its liquid state. Thus the Fabry-Perot sensor proposed in this research utilizes the cross-sensitivity effects for a reliable and accurate phase change detection.

The Fresnel fiber sensor and the SNS fiber sensor do not rely on the temperature measurement to detect a phase change. Although the Fabry-Perot fiber sensor requires temperature measurement to detect phase change, it breaks the limitation from the RI of the PCMs. The accuracy of phase changes detection for all the three sensors was confirmed by visual observations, thus the errors in temperature measurements have no effect on sensing of the phase changes.

7.2 Novelty and Originality of the Research Presented in the Thesis

Compared to the well-known phase change methods, the proposed sensors in this thesis have significant worthwhile advantages. A general summary of the sensors is shown as the following table.

Table 7.1 Summary and analysis of the proposed fiber sensors

Sensor	Principle	Detection Mode	Advantages/Contributions
Fresnel	RI	Reflected power ratio	Proposed a new method (optical fiber sensing) of phase change in-situ detection for n-octadecane with high spatial resolution
SNS	RI	The step-change of the output power ratio	<ol style="list-style-type: none"> 1. In-situ phase change detection in one measurement 2. High spatial resolution and a simple structure 3. Strong ability of anti-disturbance
Fabry-Perot	Wavelength shift	Comparison between the temperature response curve and phase change response curve of a selected dip	<ol style="list-style-type: none"> 1. Simple structure 2. Utilize cross-sensitivity to monitoring phase change 3. Not limited by the RI of the PCMs

7.2 Future work

Several research directions have been identified as possible extensions of the research presented in this thesis.

1. Detection of phase change and temperature simultaneously.

Continuous in situ monitoring of the PCM material parameters in a practical TES system is key to optimizing its energy efficiency. As was discussed previously in this thesis, temperature measurements alone cannot provide accurate information about the PCM's phase state, particularly throughout the entire PCM volume and also due to the supercooling phenomenon, which can lead to energy waste. On the other hand, binary information about the phase state of the PCM provided by the

fiber optic sensors proposed and developed in this thesis may also be insufficient to achieve optimal energy efficiency for a TES. Thus there is a need for multiparametric sensors capable of simultaneous detection of the material phase and temperature.

One possible approach to this problem is the development of hybrid fiber sensors, for example by combining the SNS fiber sensor with a long period fiber grating which is sensitive to temperature, but can be designed to be insensitive to strain and bending [106-107]. The long period fiber grating would monitor the temperature, at the same time the SNS part would monitor the phase change.

2. Detection of supercooling in PCMs

Supercooling occurs when a material remains in its liquid phase at a temperature lower than its freezing point. This phenomenon could potentially lead to losses in energy efficiency in the TES applications due to misidentification of the material's phase by the control system, thus accurate detection of the supercooling is important both in practical TES systems and as a tool for studies of phase changes in different materials such as salt hydrates and polyethylene glycol paraffin waxes.

To address this problem, another type of a hybrid fiber sensor could be developed. This could be accomplished, for example, by combining a long period fiber grating with the SNS fiber sensor or the Fabry-Perot fiber sensor. If the SNS or the Fabry-Perot sensor determines that the PCM is in its liquid state, while the long period fiber grating determines the temperature of the PCM is lower than its freezing point, the supercooled state is identified. Moreover, since the application of the Fabry-Perot fiber sensor does not rely on the RI of the PCM, the hybrid fiber sensor based

on the Fabry-Perot fiber sensor could be applied not only in organic PCMs such as n-octadecane, but also in inorganic and eutectic PCMs.

3. Detection of phase segregation (separation)

In some PCMs such as salt hydrates, repeated liquid-solid and solid-liquid phase changes could result in an incomplete dissolving of the crystalline salt which will be deposited at the bottom of the container leading to phase separation. This is likely to result in problems during the operation of TES, thus a timely detection of this phenomenon would be very useful. Since phase segregation is typically accompanied by a non-uniform distribution of the bulk RI, the SNS fiber sensor proposed here could be used for the detection of phase segregation in PCMs whose thermo-optic properties are similar to those of n-octadecane.

4. Implementation of the optical sensors in real life applications

In the industrial applications, phase change detection is the key element in many areas. One of such areas is the building energy efficiency improvement [73]. Heat and cooling demand in buildings account for a large proportion of the total energy consumption [108]. One way of reducing the energy consumption of buildings is the implementation of the solar thermal system for space heating/cooling. However, this technology requires proper monitoring and advanced control strategies to realize effective operation strategies for dynamic heat integration of the TES system. Since PCMs are always used as the key element in the TES systems, fiber sensors for phase change detection can be used in such systems. To realize that multiple Fresnel, SNS or Fabry-Perot sensors proposed here can be used in an array to monitor the energy stored rate, or the so-called state of charge, detecting the phase change at different positions within the PCM.

Another possible application of the proposed sensors is for monitoring of ice accumulation on critical aircraft surfaces. Ice accumulation on the wings of the airplane has led to major accidents in the past, thus detection of ice accumulation is mandatory [109]. Existing sensors have known issues and exploring the application of fiber optic sensors proposed in this work could be beneficial for this application. ↘

5. Multi-point detection of phase change

Due to the applications of phase change are very important in many industrial areas, the precisely monitoring of phase change is always required. For a better control of the phase change, sometimes it is necessary to know the phase state at different positions of the PCMs. Thus phase change detection of multiple points is very useful to achieve this goal. For detecting the phase change of multiple points in simultaneously, hybrid fiber sensors could be very useful. Since hybrid fiber sensors are fabricated by combining different sensors together at the different positions of the same fiber, each sensor would detect the phase change at the position where the sensor is, by monitoring the output of the hybrid fiber sensor, the phase change detection of multiple points could be realized.

References

1. BP p.l.c (2019). BP Energy Outlook 2019 edition. <https://www.bp.com/content/dam/bp/business-sites/en/global/corporate/pdfs/energy-economics/energy-outlook/bp-energy-outlook-2019.pdf>
2. de Gracia, A., & Cabeza, L. F. (2015). Phase change materials and thermal energy storage for buildings. *Energy and Buildings*, 103, 414-419.
3. Zhang, C., Chen, Y., Wu, L., & Shi, M. (2011). Thermal response of brick wall filled with phase change materials (PCM) under fluctuating outdoor temperatures. *Energy and Buildings*, 43(12), 3514-3520.
4. Lai, C. M., & Hokoi, S. (2014). Thermal performance of an aluminum honeycomb wallboard incorporating microencapsulated PCM. *Energy and Buildings*, 73, 37-47.
5. Barzin, R., Chen, J. J., Young, B. R., & Farid, M. M. (2015). Application of PCM underfloor heating in combination with PCM wallboards for space heating using price based control system. *Applied energy*, 148, 39-48.
6. Cheng, W., Xie, B., Zhang, R., Xu, Z., & Xia, Y. (2015). Effect of thermal conductivities of shape stabilized PCM on under-floor heating system. *Applied energy*, 144, 10-18.
7. Papapetrou, M., Kosmadakis, G., Cipollina, A., La Commare, U., & Micale, G. (2018). Industrial waste heat: Estimation of the technically available resource in the EU per industrial sector, temperature level and country. *Applied Thermal Engineering*, 138, 207-216.
8. Langan, M., & O'Toole, K. (2017). A new technology for cost effective low grade waste heat recovery. *Energy Procedia*, 123, 188-195.
9. Miró, L., Brückner, S., & Cabeza, L. F. (2015). Mapping and discussing Industrial Waste Heat (IWH) potentials for different countries. *Renewable and Sustainable Energy Reviews*, 51, 847-855.

10. Li, D., Wang, J., Ding, Y., Yao, H., & Huang, Y. (2019). Dynamic thermal management for industrial waste heat recovery based on phase change material thermal storage. *Applied Energy*, 236, 1168-1182.
11. Akram, N., Moazzam, M. U., Ali, H. M., Ajaz, A., Saleem, A., MOBEEN, A., & KILIC, M. (2018). Improved waste heat recovery through surface of kiln using phase change material. *Thermal Science*, 22(2).
12. Huang, Z., Luo, Z., Gao, X., Fang, X., Fang, Y., & Zhang, Z. (2017). Investigations on the thermal stability, long-term reliability of LiNO₃/KCl-expanded graphite composite as industrial waste heat storage material and its corrosion properties with metals. *Applied energy*, 188, 521-528.
13. Merlin, K., Soto, J., Delaunay, D., & Traonvouez, L. (2016). Industrial waste heat recovery using an enhanced conductivity latent heat thermal energy storage. *Applied energy*, 183, 491-503.
14. Soibam, J. (2017). *Numerical Investigation of a Phase Change Materials (PCM) heat exchanger-For small scale combustion appliances* (Master's thesis, NTNU).
15. Mohamed, S. A., Al-Sulaiman, F. A., Ibrahim, N. I., Zahir, M. H., Al-Ahmed, A., Saidur, R., ... & Sahin, A. Z. (2017). A review on current status and challenges of inorganic phase change materials for thermal energy storage systems. *Renewable and Sustainable Energy Reviews*, 70, 1072-1089.
16. Zhang, P., Xiao, X., & Ma, Z. W. (2016). A review of the composite phase change materials: Fabrication, characterization, mathematical modeling and application to performance enhancement. *Applied Energy*, 165, 472-510.
17. Sharma, S. D., Kitano, H., & Sagara, K. (2004). Phase change materials for low temperature solar thermal applications. *Res. Rep. Fac. Eng. Mie Univ*, 29(1).
18. Ip, K., & Miller, A. (2009). Thermal behaviour of an earth-sheltered autonomous building—The Brighton Earthship. *Renewable Energy*, 34(9), 2037-2043
19. Dodoo, A., Gustavsson, L., & Sathre, R. (2012). Effect of thermal mass on life cycle primary energy balances of a concrete-and a wood-frame building. *Applied Energy*, 92, 462-472.
20. Pielichowska, K., & Pielichowski, K. (2014). Phase change materials for thermal energy storage. *Progress in materials science*, 65, 67-123.

21. Kovajsa, J., Koláček, M., & Zálešák, M. (2017). Phase change material based accumulation panels in combination with renewable energy sources and thermoelectric cooling. *Energies*, 10(2), 152.
22. Muthuvelan, T., Panchabikesan, K., Munisamy, R., Nibhanupudi, K. M., & Ramalingam, V. (2018). Experimental investigation of free cooling using phase change material-filled air heat exchanger for energy efficiency in buildings. *Advances in Building Energy Research*, 12(2), 139-149.
23. Tan, P., Lindberg, P., Eichler, K., Löveryd, P., Johansson, P., & Kalagasidis, A. S. (2020). Effect of phase separation and supercooling on the storage capacity in a commercial latent heat thermal energy storage: Experimental cycling of a salt hydrate PCM. *Journal of Energy Storage*, 29, 101266.
24. Hsu, T. H., Chung, C. H., Chung, F. J., Chang, C. C., Lu, M. C., & Chueh, Y. L. (2018). Thermal hysteresis in phase-change materials: Encapsulated metal alloy core-shell microparticles. *Nano Energy*, 51, 563-570.
25. Hecht, E., & Zajac, A. (2002). *Optics*, Addison-Wesley, 3, 384-441.
26. F. Jenkins, F. A., & White, H. E. (2001). *Fundamentals of optics*. McGraw-Hill, Inc.
27. Zhou, Z. X., Tian, H., Meng, Q. X., Gong, D. W., & Li, J. (2017). *Opto-electrical functional materials and devices*. Higher Education Press.
28. Aucejo, A., Burguet, M. C., Munoz, R., & Marques, J. L. (1995). Densities, viscosities, and refractive indices of some n-alkane binary liquid systems at 298.15 K. *Journal of Chemical and Engineering Data*, 40(1), 141-147.
29. Glycerine Producers' Association. (1963). *Physical properties of glycerine and its solutions*. Glycerine Producers' Association.
30. Cui, Y., Xie, J., Liu, J., Wang, J., & Chen, S. (2017). A review on phase change material application in building. *Advances in Mechanical Engineering*, 9(6), 1687814017700828.
31. EIA, U. (2014). How much energy is consumed in the world by each sector. *US Energy Information Administration*.
32. Cabeza, L. F., Castell, A., Barreneche, C. D., De Gracia, A., & Fernández, A. I. (2011). Materials used as PCM in thermal energy storage in buildings: A review. *Renewable and Sustainable Energy Reviews*, 15(3), 1675-1695.

33. Koo, J., So, H., Hong, S. W., & Hong, H. (2011). Effects of wallboard design parameters on the thermal storage in buildings. *Energy and Buildings*, 43(8), 1947-1951
34. Meng, E., Yu, H., Liu, C., Sun, Z., & Zhou, B. (2015). Design of Phase Change Material Wall Based on the Heat Transfer Characteristics in Summer. *Procedia Engineering*, 121, 2201-2208.
35. Lin, K., Zhang, Y., Xu, X., Di, H., Yang, R., & Qin, P. (2004). Modeling and simulation of under-floor electric heating system with shape-stabilized PCM plates. *Building and Environment*, 39(12), 1427-1434.
36. Baek, S., & Kim, S. (2019). Analysis of Thermal Performance and Energy Saving Potential by PCM Radiant Floor Heating System based on Wet Construction Method and Hot Water. *Energies*, 12(5), 828.
37. Zeinelabdein, R., Omer, S., Mohamed, E., Amaireh, I., & Gan, G. (2017). Free cooling based phase change material for domestic buildings in hot arid climate.
38. Turnpenny, J. R., Etheridge, D. W., & Reay, D. A. (2001). Novel ventilation system for reducing air conditioning in buildings. Part II: testing of prototype. *Applied thermal engineering*, 21(12), 1203-1217.
39. Jaguemont, J., Omar, N., Van den Bossche, P., & Mierlo, J. (2018). Phase-change materials (PCM) for automotive applications: A review. *Applied Thermal Engineering*, 132, 308-320.
40. Pesaran, A. A., Vlahinos, A., & Burch, S. D. (1997). *Thermal performance of EV and HEV battery modules and packs*. National Renewable Energy Laboratory.
41. Lukic, S. M., Cao, J., Bansal, R. C., Rodriguez, F., & Emadi, A. (2008). Energy storage systems for automotive applications. *IEEE Transactions on industrial electronics*, 55(6), 2258-2267.
42. Sabbah, R., Kizilel, R., Selman, J. R., & Al-Hallaj, S. (2008). Active (air-cooled) vs. passive (phase change material) thermal management of high power lithium-ion packs: Limitation of temperature rise and uniformity of temperature distribution. *Journal of Power Sources*, 182(2), 630-638.
43. Yan, J., Li, K., Chen, H., Wang, Q., & Sun, J. (2016). Experimental study on the application of phase change material in the dynamic cycling of battery pack system. *Energy Conversion and Management*, 128, 12-19..

44. Babapoor, A., Azizi, M., & Karimi, G. (2015). Thermal management of a Li-ion battery using carbon fiber-PCM composites. *Applied Thermal Engineering*, 82, 281-290.
45. Kim, K. B., Choi, K. W., Kim, Y. J., Lee, K. H., & Lee, K. S. (2010). Feasibility study on a novel cooling technique using a phase change material in an automotive engine. *Energy*, 35(1), 478-484.
46. Pielichowska, K., & Pielichowski, K. (2014). Phase change materials for TES. *Progress in materials science*, 65, 67-123.
47. Andrews, D. D., Krook-Riekkola, A., Tzimas, E., Serpa, J., Carlsson, J., Pardo-Garcia, N., & Papaioannou, I. (2012). *Background report on EU-27 district heating and cooling potentials, barriers, best practice and measures of promotion*. Publications Office of the European Union.
48. Kürklü, A., Özmerzi, A., & Bilgin, S. (2002). Thermal performance of a water-phase change material solar collector. *Renewable Energy*, 26(3), 391-399.
49. Hammou, Z. A., & Lacroix, M. (2006). A new PCM storage system for managing simultaneously solar and electric energy. *Energy and Buildings*, 38(3), 258-265.
50. Kerslake, T. W. (1991). Experiments with phase change thermal energy storage canisters for Space Station Freedom. In *iece* (Vol. 1, pp. 248-261).
51. Lafdi, K., Mesalhy, O., & Elgafy, A. (2008). Graphite foams infiltrated with phase change materials as alternative materials for space and terrestrial TES applications. *Carbon*, 46(1), 159-168.
52. Cui, H., Yuan, X., & Hou, X. (2003). Thermal performance analysis for a heat receiver using multiple phase change materials. *Applied thermal engineering*, 23(18), 2353-2361.
53. Li, X., Nguyen, L. V., Becker, M., Ebendorff-Heidepriem, H., Pham, D., & Warren-Smith, S. C. (2019). Simultaneous measurement of temperature and refractive index using an exposed core microstructured optical fiber. *IEEE Journal of Selected Topics in Quantum Electronics*, 26(4), 1-7.
54. Sun, X., Du, H., Dong, X., Hu, Y., & Duan, J. A. (2019). Simultaneous Curvature and Temperature Sensing Based on a Novel Mach-Zehnder Interferometer. *Photonic Sensors*, 1-10.
55. Samarskii, A. A., Vabishchevich, P. N., Iliev, O. P., & Churbanov, A. G.

- (1993). Numerical simulation of convection/diffusion phase change problems—a review. *International journal of heat and mass transfer*, 36(17), 4095-4106.
56. Liao, Y., & Li, M. (2013). *Fiber optics*. Tsinghua University Press.
57. Zhao, C. L., Li, J., Zhang, S., Zhang, Z., & Jin, S. (2013). Simple Fresnel reflection-based optical fiber sensor for multipoint refractive index measurement using an AWG. *IEEE Photonics Technology Letters*, 25(6), 606-608.
58. Su, H., & Huang, X. G. (2007). Fresnel-reflection-based fiber sensor for on-line measurement of solute concentration in solutions. *Sensors and Actuators B: Chemical*, 126(2), 579-582.
59. Chen, L. X., Huang, X. G., Zhu, J. H., Li, G. C., & Lan, S. (2011). Fiber magnetic-field sensor based on nanoparticle magnetic fluid and Fresnel reflection. *Optics letters*, 36(15), 2761-2763.
60. Mani, P., Rallapalli, A., Machavaram, V. R., & Sivaramakrishna, A. (2016). Monitoring phase changes in supercooled aqueous solutions using an optical fiber Fresnel reflection sensor. *Optics express*, 24(5), 5395-5410.
61. Ferreira, M. S., Coelho, L., Schuster, K., Kobelke, J., Santos, J. L., & Frazão, O. (2011). Fabry–Perot cavity based on a diaphragm-free hollow-core silica tube. *Optics letters*, 36(20), 4029-4031.
62. Chen, P., Shu, X., & Cao, H. (2017). Novel compact and low-cost ultraweak Fabry–Perot interferometer as a highly sensitive refractive index sensor. *IEEE Photonics Journal*, 9(5), 1-10.
63. Quan, M., Tian, J., & Yao, Y. (2015). Ultra-high sensitivity Fabry–Perot interferometer gas refractive index fiber sensor based on photonic crystal fiber and Vernier effect. *Optics letters*, 40(21), 4891-4894
64. Ma, Z., Cheng, S., Kou, W., Chen, H., Wang, W., Zhang, X., & Guo, T. (2019). Sensitivity-Enhanced Extrinsic Fabry–Perot Interferometric Fiber-Optic Microcavity Strain Sensor. *Sensors*, 19(19), 4097.
65. Lv, Z., Wang, S., Jiang, J., Liu, K., Zhang, X., Qi, X., Liu, T. (2019) Long-sensing-length strain sensor based on optical fiber Fabry-Perot interferometer with HCF-SMF Structure. *IEEE Photonics Journal*, 11(6), 1-8.

66. Yin, B., Li, Y., Liu, Z. B., Feng, S., Bai, Y., Xu, Y., & Jian, S. (2016). Investigation on a compact in-line multimode-single-mode-multimode fiber structure. *Optics & Laser Technology*, 80, 16-21.
67. Li, C., Qiu, S. J., Chen, Y., Xu, F., & Lu, Y. Q. (2012). Ultra-sensitive refractive index sensor with slightly tapered photonic crystal fiber. *IEEE Photonics Technology Letters*, 24(19), 1771-1774.
68. Li, Z., Liao, C., Wang, Y., Dong, X., Liu, S., Yang, K., ... & Zhou, J. (2014). Ultrasensitive refractive index sensor based on a Mach-Zehnder interferometer created in twin-core fiber. *Optics letters*, 39(17), 4982-4985.
69. Dong, X., Du, H., Luo, Z., & Duan, J. A. (2018). Highly sensitive strain sensor based on a novel Mach-Zehnder interferometer with TCF-PCF structure. *Sensors*, 18(1), 278.
70. Avila-Garcia, M. S., Bianchetti, M., Le Corre, R., Guevel, A., Mata-Chavez, R. I., Sierra-Hernandez, J. M., ... & Rojas-Laguna, R. (2018). High sensitivity strain sensors based on single-mode-fiber core-offset Mach-Zehnder interferometers. *Optics and Lasers in Engineering*, 107, 202-206.
71. Tian, K., Zhang, M., Farrell, G., Wang, R., Lewis, E., & Wang, P. (2018). Highly sensitive strain sensor based on composite interference established within S-tapered multimode fiber structure. *Optics express*, 26(26), 33982-33992.
72. Andrásy, Z., & Szantho, Z. (2019). Thermal behaviour of materials in interrupted phase change. *Journal of Thermal Analysis and Calorimetry*, 138(6), 3915-3924.
73. Zsembinszki, G., Orozco, C., Gasia, J., Barz, T., Emhofer, J., & Cabeza, L. F. (2020). Evaluation of the state of charge of a solid/liquid phase change material in a thermal energy storage tank. *Energies*, 13(6), 1425.
74. Soares, N., Rosa, N., Costa, J. J., Lopes, A. G., Matias, T., Simões, P. N., & Durães, L. Validation of different numerical models with benchmark experiments for modelling microencapsulated-PCM-based applications for buildings. *International Journal of Thermal Sciences*, 159, 106565.
75. Waser, R., Ghani, F., Maranda, S., O'Donovan, T. S., Schuetz, P., Zaglio, M., & Worlitschek, J. (2018). Fast and experimentally validated model of a latent thermal energy storage device for system level simulations. *Applied Energy*, 231, 116-126.

76. Akamatsu, S., Faivre, G., & Ihle, T. (1995). Symmetry-broken double fingers and seaweed patterns in thin-film directional solidification of a nonfaceted cubic crystal. *Physical Review E*, 51(5), 4751.
77. Yin, H., & Koster, J. N. (1999). In situ observation of concentrational stratification and solid–liquid interface morphology during Ga–5% In alloy melt solidification. *Journal of crystal growth*, 205(4), 590-606.
78. Shirtcliffe, T. G. L., Huppert, H. E., & Worster, M. G. (1991). Measurement of the solid fraction in the crystallization of a binary melt. *Journal of crystal growth*, 113(3-4), 566-574.
79. Lazaro, A., Peñalosa, C., Solé, A., Diarce, G., Haussmann, T., Fois, M., & Cabeza, L. F. (2013). Intercomparative tests on phase change materials characterisation with differential scanning calorimeter. *Applied Energy*, 109, 415-420
80. Sun, Z., Yang, P., Luo, K., & Wu, J. (2021). Experimental investigation on the melting characteristics of n-octadecane with electric field inside macrocapsule. *International Journal of Heat and Mass Transfer*, 173, 121238.
81. Aubuchon, S. R., & Instruments, T. A. (2007). Interpretation of the crystallization peak of supercooled liquids using Tzero DSC. *TA344*.
82. Liu, X., Zhuang, K., Lin, S., Zhang, Z., & Li, X. (2017). Determination of supercooling degree, nucleation and growth rates, and particle size for ice slurry crystallization in vacuum. *Crystals*, 7(5), 128.
83. Kalke, H., McFarlane, V., Ghobrial, T. R., & Loewen, M. R. (2019). Field Measurements of Supercooling in the North Saskatchewan River. *20th Workshop on the Hydraulics of Ice Covered Rivers, Ottawa, Ontario, Canada, Committee on River Ice Processes and the Environment*.
84. Zhang, X., Zhou, W., & Li, H. (2019). Electromechanical impedance-based ice detection of stay cables with temperature compensation. *Structural Control and Health Monitoring*, 26(9), e2384.
85. Gao, H., & Rose, J. L. (2009). Ice detection and classification on an aircraft wing with ultrasonic shear horizontal guided waves. *IEEE transactions on ultrasonics, ferroelectrics, and frequency control*, 56(2), 334-344.
86. Lindon, J. C., Tranter, G. E., & Koppelaar, D. (2016). *Encyclopedia of spectroscopy and spectrometry*. Academic Press.

87. Millo, A., Raichlin, Y., & Katzir, A. (2005). Mid-infrared fiber-optic attenuated total reflection spectroscopy of the solid–liquid phase transition of water. *Applied spectroscopy*, 59(4), 460-466.
88. Wahl, M. S., Wilhelmsen, Ø., & Hjelme, D. R. (2020). Using fiber-optic sensors to give insight into liquid-solid phase transitions in pure fluids and mixtures. *Experimental Thermal and Fluid Science*, 119, 110198.
89. Boerkamp, M., Lamb, D. W., & Lye, P. G. (2011). Investigating surface crystal growth using an intrinsic exposed core optical fibre sensor. *Sensors and Actuators B: Chemical*, 157(2), 581-585.
90. Ikiades, A. A. (2007). Direct ice detection based on fiber optic sensor architecture. *Applied Physics Letters*, 91(10), 104104.
91. Prasad, S. B., Hegde, G., & Asokan, S. (2019, December). Fiber Bragg grating based ice detection sensor. In *2019 Workshop on Recent Advances in Photonics (WRAP)* (pp. 1-4). IEEE.
92. Wahl, M. S., Aasen, A., Hjelme, D. R., & Wilhelmsen, Ø. (2020). Ice formation and growth in supercooled water–alcohol mixtures: Theory and experiments with dual fiber sensors. *Fluid Phase Equilibria*, 522, 112741.
93. Hatta A M, Farrell G, Wang Q, Rajan G, Wang, P and Semenova, Y. (2008). Ratiometric wavelength monitor based on singlemode - multimode - singlemode fiber structure *Microw. Opt. Technol. Lett.* 50 3036-9.
94. Kim, M. S., Kim, M. K., Jo, S. E., Joo, C., & Kim, Y. J. (2016). Refraction-assisted solar thermoelectric generator based on phase-change lens. *Scientific reports*, 6(1), 1-9.
95. Jenkins, F. A., & White, H. E. (1937). *Fundamentals of optics*. Tata McGraw-Hill Education.
96. Xu, W., Shi, J., Yang, X., Xu, D., Rong, F., Zhao, J., & Yao, J. (2017). Improved numerical calculation of the single-mode-no-core-single-mode fiber structure using the fields far from cutoff approximation. *Sensors*, 17(10), 2240.
97. Han, W., Rebow, M., Liu, D., Farrell, G., Semenova, Y., & Wu, Q. (2018). Optical fiber Fresnel reflection sensor for direct detection of the solid-liquid phase change in n-octadecane. *Measurement Science and Technology*.

98. Yang, L., Xue, L., Che, D., & Qian, J. (2012). Guided-mode-leaky-mode-guided-mode fiber structure and its application to high refractive index sensing. *Optics letters*, 37(4), 587-589.
99. Wu, Q., Semenova, Y., Wang, P., & Farrell, G. (2011). High sensitivity SMS fiber structure based refractometer—analysis and experiment. *Optics Express*, 19(9), 7937-7944.
100. Wu, C., Liu, Z., Zhang, A. P., Guan, B. O., & Tam, H. Y. (2014). In-line open-cavity Fabry–Pérot interferometer formed by C-shaped fiber for temperature-insensitive refractive index sensing. *Optics express*, 22(18), 21757-21766.
101. Chen, Z., Xiong, S., Gao, S., Zhang, H., Wan, L., Huang, X. & Li, Z. (2018). High-Temperature Sensor Based on Fabry-Perot Interferometer in Microfiber Tip. *Sensors*, 18(1), 202.
102. Chen, M. Q., Zhao, Y., Xia, F., Peng, Y., & Tong, R. J. (2018). High sensitivity temperature sensor based on fiber air-microbubble Fabry-Perot interferometer with PDMS-filled hollow-core fiber. *Sensors and Actuators A: Physical*, 275, 60-66.
103. Shi, Q., Lv, F., Wang, Z., Jin, L., Hu, J. J., Liu, Z., & Dong, X. (2008). Environmentally stable Fabry–Pérot-type strain sensor based on hollow-core photonic bandgap fiber. *IEEE Photonics Technology Letters*, 20(4), 237-239.
104. Monteiro, C. S., Ferreira, M. S., Silva, S. O., Kobelke, J., Schuster, K., Bierlich, J., & Frazão, O. (2016). Fiber Fabry-Perot interferometer for curvature sensing. *Photonic Sensors*, 6(4), 339-344.
105. Mehling, H., Leys, J., Glorieux, C., & Thoen, J. (2021). Potential new reference materials for caloric measurements on PCM. *SN Applied Sciences*, 3(2), 1-22.
106. Wang, Y. P., Rao, Y. J., Ran, Z. L., Zhu, T., & Zeng, X. K. (2004). Bend-insensitive long-period fiber grating sensors. *Optics and Lasers in Engineering*, 41(1), 233-239.
107. Zhu, Y., Shum, P., Bay, H. W., Yan, M., Yu, X., Hu, J., ... & Lu, C. (2005). Strain-insensitive and high-temperature long-period gratings inscribed in photonic crystal fiber. *Optics letters*, 30(4), 367-369.
108. Kempener, R., Burch, J., Navntoft, C., Mugnier, D., Nielsen, J. E., & Weiss, W. (2015). Solar Heating and Cooling for Residential Applications. *IEA-*

ETSAP and IRENA.

109. Wiltshire, B., Mirshahidi, K., Golovin, K., & Zarifi, M. H. (2019). Robust and sensitive frost and ice detection via planar microwave resonator sensor. *Sensors and Actuators B: Chemical*, 301, 126881.